2017

Mechanical Functions of the Endothelial Glycocalyx

Matthew A. Dragovich
Lehigh University

Mechanical Functions of the Endothelial Glycocalyx

By

Matthew Dragovich

Presented to the Graduate and Research Committee

of Lehigh University

in Candidacy for the Degree of

Doctor of Philosophy

in

Mechanical Engineering

Lehigh University

May, 2017

Approved and recommended for acceptance as a dissertation in partial fulfillment of the requirements for the degree of Doctor of Philosophy.

_____

Date

_____

Dissertation Advisor, Dr. Xiaohui (Frank) Zhang

_____

Accepted Date

Committee Members:

_____

Dr. Hannah Dailey

_____

Dr. Sabrina Jedlicka

_____

Dr. Yaling Liu

Acknowledgments

I would like to first acknowledge my Ph.D. advisor, Dr. Xiaohui (Frank) Zhang. Frank was the first person who believed enough in my abilities as a scientist to allow me the privilege to work under him. I have spent the last four years of my life honoring his decision by working as hard as I could as to not let him down. Frank is an intelligent, dedicated and well rounded scientist with a deep knowledge in the subjects of biology, physics and engineering. His hard work and kindness has shaped both my professional and personal life. I am beyond proud to call him my mentor.

Furthermore, I would like to acknowledge my committee members: Dr. Hannah Dailey, Dr. Sabrina Jedlicka and Dr. Yaling Liu. I would like to show gratitude Hannah for providing her expertise in statistics. She has greatly aided me in improving a base of knowledge that I will take with me for the rest of my career. I would like to thank Sabrina for her offering expertise in cell staining techniques. This skill has aided in several publications. Lastly, I would like to show appreciation to Yaling for his assistance and commentary on my projects, particularly in the field of cell-cell adhesion mechanics.

I want to thank our collaborator at the City University of New York, Dr. Bingmei Fu and or collaborator at New York Medical College, Dr. Michael Goligorsky for assisting me with my first publication on the endothelial glycocalyx. Also, I would like to thank Dr. Renhao Li, at Emory University for helping with the glycoprotein Ib-IX complex and related mutants.

I would finally like to thank the Lehigh University department of Mechanical Engineering and Engineering Mechanics for providing me with one of the best academic

environments in the world. Also, for believing in a diverse application of mechanical engineering that allowed for the pursuit of my research goals. Furthermore, I would like to thank the University for providing me with financial support in the forms of fellowships and teaching assistantships.

Most importantly I would like to thank my family. My mother and father have provided me with the motivation to succeed in my endeavor to become a scientist. I owe them a debt of gratitude that I could never repay. Also, I would like to thank my wife. She has been by my side since I have started my education at community college. She has never stopped believing in me and I will never stop believing in her.

Table of Contents

List of tables

List of Figures

Abstract

The first part of this thesis is dedicated to how endothelial cells (ECs) produce nitric oxide (NO) due to mechanical perturbations, a process known as mechanotransduction. NO is perhaps one of the most important protective molecules in the body and is responsible for vasorelaxation, which staves off high blood pressure. Although this field has been heavily researched over the past ten years a clear picture of the underlying mechanisms that allow for this affect to take place have yet to be elucidated. Based on previous research endeavors it has been shown that the gel like carbohydrate rich layer found on the surface of ECs is a key player in NO production when ECs are exposed to shear stress due to flow. This layer is known as the endothelial surface glycocalyx (ESG). The ESG contains the long oligosaccharide chain heparan sulfate (HS), that when removed will prevent ECs producing NO under flow conditions. Also, if the protein glypican-1 that anchors HS to the EC surface is knocked out, NO will not be produced under flow conditions. Furthermore, other studies have shown that ECs will not produce NO when transient receptor potential (TRP) channels are inhibited. These channels are mechanically activated, ion soluble and known to allow Ca^{2+} to enter ECs, a molecule that allows the NO production cascade to begin. Therefore, the primary question that remained unanswered until now was how the HS-glypican-1 complex mechanically activates TRP channels to begin the NO production cascade.

The big picture problem that knowledge of this pathway may improve is treating diseases in which the ESG is disrupted. These diseases, such as diabetes and arteriosclerosis go hand in glove with reduced NO production which impairs

vasorelaxation, leading to high blood pressure. However, the problem was that, until now, there has been no way to investigate the aforementioned question experimentally. Our solution to this was to utilize an atomic force microscope (AFM) to apply force to the surface of ECs, targeting the ESG, to induce NO production.

An AFM is a highly sensitive tool that can provide minute mechanical forces to a cell via a micro cantilever. In chapter 3 we coated the AFM probe in ployLysine, an amino acid that has a strong positive charge. With this charge we were able to mechanically stimulate the surface of an EC due to the ESG's strong negative charge. When the ESG was perturbed by the AFM probe NO was produced in the EC. When HS was removed NO was no longer produced after mechanical stimulation via AFM. Moreover, when the TRP channel TRPP2 was inhibited, NO was not produced. A publication of this method can be found in the American Journal of Physiology (doi:10.1152/ajpcell.00288.2015). From this we have concluded that the ESG component HS is placing mechanical stress on TRP channels, such as TRPP2, causing them to allow Ca^{2+} into the EC thus beginning the NO production cascade.

After this time of initial discovery we focused on developing a new technique that will allow for the mechanical stimulation of HS or glypican-1 only on a fully intact ESG. Therefore, we can target the affects that HS or glypican-1 have on NO production directly, not simply infer what they do after HS is removed. This path was evaluated in chapter 4. It was the first experimental exploration to demonstrate that the affect witnessed in my first publication was not due to ESG damage after HS removal. To attain this goal we coated the AFM probes in glypican-1 antibodies to achieve specificity. The

results allow us to conclude that applying mechanical force to glypican-1 will result in rapid NO production. Moreover, this NO production can be completely inhibited by blocking TRPC channels and reduced by blocking TRPP channels. Together, our results demonstrated that the molecular mechanism of rapid NO production is a result of glypican-1creating mechanical tension in the cell membrane, activating TRPC and TRPP channels.

An additional chapter was written about the ESG's affect in inflammation. This work involved using an AFM-based single-cell adhesion assay where we directly quantified the detachment force and work perpendicular to the cell membrane of a leukocyte from a human umbilical cord vein endothelial cell (HUVEC). To perform this delicate procedure we again turned to the use of a ployLysine coated probe. This allowed us to pick up an individual K562 leukocyte with the AFM probe. After doing this the K562 was brought over a single HUVEC for adhesion testing. This was performed with an intact ESG, or with the major ESG components, HS and/or hyaluronic acid (HA) removed. For the resting HUVECs, when HS and/or HA were removed, the detachment force and work increased. For the HUVECs activated by inflammatory cytokine tumor necrosis factor alpha, we observed increases in the detachment force and work compared to the resting HUVECs. Furthermore, under inflammatory conditions, removal of HS and/or HA resulted in significant decreases in the detachment force and work. The results demonstrated that the ESG layer serves a dual function: (1) on resting endothelium, it prevents leukocyte adhesion, and (2) under inflammatory conditions, it participates in endothelial-leukocyte interactions with molecules such as selectins. A

publication on this work can be found in the BMES journal. (10.1007/s12195-016-0463-6).

Lastly we performed an analysis on the reliability of AFM nanoindentation-derived measurements of cell mechanics. AFM is an experimental technique that is often used for measuring the mechanical properties of cells and other soft materials. Despite its widespread adoption as a biophysical assay, no universal standards have been adopted for the technique. This has potentially caused the problem of irreproducible results when scientists utilize this technique. The purpose of this study was to assess the accuracy and repeatability of AFM-derived cell stiffness measurements. Therefore, we conducted a series of experiments on ASPC-1 cells (A human pancreatic cancer cell line) to compare a variety of conditions that may be leading to this inaccuracy. The conditions that observed were the following: conical vs. spherical AFM tips, nuclear vs. peripheral indentation locations, multiple piezo actuation speeds and multiple indentation forces. We then quantified apparent cell stiffness using classical contact mechanics with the Hertz model for the spherical tip and Sneddon model for the conical tip. From this we could draw several significant conclusions. The most important is that across experimental conditions, cells appeared to be stiffer when probed with conical tips compared to spherical tips. Moreover, there were no differences in apparent cell stiffness based on AFM actuation speed or indentation force. We have thus concluded that AFM remains a valuable technique for probing the mechanical properties of cells, but greater consensus can be achieved through adoption of standardized methods.

Chapter 1: Introduction

1.1 The Endothelial Surface Glycocalyx

Endothelial cells (ECs) form a single-cell layer that lines the internal surface of blood vessels throughout the entire vascular system. On their luminal surface, these cells are covered by a gel-like matrix known as the endothelial surface glycocalyx (ESG). ESG has been shown to provide a multifunctional protective coating critical for the mechanotransduction of fluid shear stress, the maintenance of the EC permeability barrier, and the control of leukocyte adhesion during inflammation. Despite these fundamental observations, the structural, functional, and mechanical properties of ESG have not been well characterized.

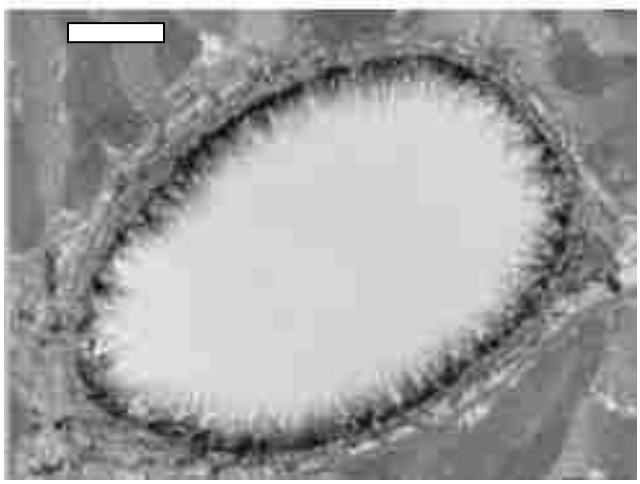

Figure 1.1: Electron microscopy image of the endothelial glycocalyx. The image depicts the ESG of a rat left ventricular myocardial capillary stained with Alcian blue 8GX. The scale bar represents 1 µm. This image was adapted from van den Berg, B. M, et al. The endothelial glycocalyx protects against myocardial edema. Circ Res. Doi:10.1161/01.Res.0000065917.53950.75. 2003 (131).

1.2 Structure of the ESG

The ESG is a negatively charged layer comprised mainly of glycosaminoglycans (GAGs), proteoglycans and glycoprotiens (39, 104). The net negative charge of the ESG is due mainly to the GAGs, Heparan sulfate (HS), hyaluronic acid (HA) and chondroitin sulfate (CS) (39). Do to this, the ESG is thought to capture circulating plasma protein such to form an organized gel-like matrix when in a water based solvent environment (97, 119, 139).

The GAGs, HS, HA and CS are linear polymers of disaccharides that have varying lengths and are modified by sulfation (104), HS comprises around 50-80% of the total GAGs (59, 103) and is typically found in a 4:1 ratio with CS (86). These GAGs form chain like structures that are held to the surface of the endothelial cells by proteoglycans and glycoprotiens. The proteoglycans consist primarily of syndecans, glypicans and glycoprotiens, such as CD44, and form the backbone of the ESG. Syndecans-1, -2, -4 contain attachment sites for HS, and syndecan-1 also harbors two more attachment sites for CS close to the cell membrane (39). The syndecans have cytoplasmic tails that are known to be associated with the cellular cytoskeleton. This interaction occurs through the molecules such as ezrin, tubulin, syntenin, syndesmos, dynamin, α-actinin (39) and perhaps F-actin (123). Syndecans can distribute force across the cell (39) as well as act as mechanical transducers of tension signals (154). Glypican-1, the only known glypican to be expressed on the surface of endothelial cells, is anchored to the cell surface through a C-terminal glycosylphosphatidylinositol (GPI) anchor (37), which restricts its location to lipid rich regions such as caveolae (39). Glypican-1 interacts

exclusively with HS (45). The transmembrane glycoprotein CD44, the only binding site for HA (45, 87), also contains binding sites for CS (45) and is also located in the lipid rich caveolae (39). Although these components are in close proximity to one another and weave in and out of the cellular surface they are not known to interact with one another (148). Therefore, HS and/or HA can be removed without affecting the rest of the ESG structure.

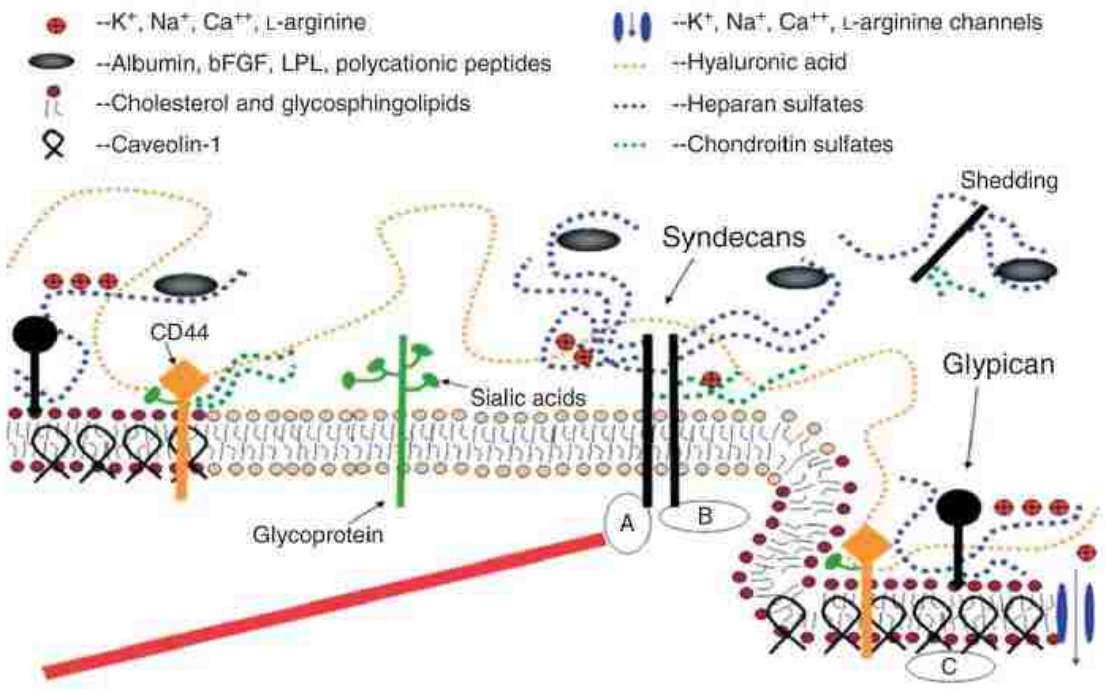

Figure 1.2: Cartoon rendition of the ESG components. Caveolin-1 associates with regions high in cholesterol and sphingolipids in the EC membrane (darker circles, left), and forms cave-like structures, caveolae (right). Glypicans, along with their HS chains (blue dotted lines) localize in these regions. Transmembrane syndecans are shown to cluster in the outer edge of caveolae. Besides HS, syndecans also contain CS, lower down the core protein (green dotted lines). A glycoprotein with its short oligosaccharide branched chains and their associated SA 'caps' are displayed in the middle part of the figure (green). HA is a very long GAG (orange dotted line), which weaves into the glycocalyx and binds with CD44. Transmembrane CD44 can have CS, HS and oligosaccharides attached to it, and localizes in caveolae. Plasma proteins (gray), along with cations and cationic amino acids (red circles) are known to associate with GAGs. (A) The cytoplasmic domains of syndecans can associate with linker molecules which connect them to cytoskeletal elements (red line). (B) Oligomerization of syndecans helps them make direct associations with intracellular signaling effectors. (C) A series of molecules involved in eNOS signaling localize in caveolae. Image adapted from Tarbell, J.M, et al. Mechanotransduction and the glycocalyx. J Intern Med. Doi:10.1111/j.1365-2796.2006.01620.x. 2006 (127).

The thickness of the ESG is still not fully understood. This particular topic suffers from a large variance in measurement values and measurement technique. The

thickness has been shown to be on the order of 20nm in frog microvessels found via electron microscopy (1, 78), which dehydrates the ESG before imaging, to 0.4µm found via atomic force microscopy (AFM) on human umbilical cord veins. However, what is known is that the ESG height, on a variety of endothelial cells, is dependent on how and where the ESG is measured. Most in vivo measurements place the height at about 0.5-0.2µm in capillaries and small veins (44, 76, 96, 135) as well as some cultured endothelial cells such as bEnd.3 cells (146), which are an immortalized cell line from rat brain endothelial cells. In bulky blood vessels, such as aortas, the ESG has been shown to be on the order of 4.3–4.5µm in the common mouse carotid artery (81). These measurements have been found by multi-photon microscopy combined with anti-body labeling.

Little is known about the ultrastructure of the ESG. However, it has been shown that the ESG does not completely cover the entire cell surface, but rather occurs in patches with quasi-periodicity between clusters where the inter-cluster spacing is about 100nm (4, 123). This shape and structure may aid in the ESGs ability to perform vital biological functions.

Over the past decade, it has become increasingly clear that the ESG functions as a mechanical sensor and transducer used to regulate NO production. Previous studies have demonstrated that removal of the two major GAG components of the ESG, HA and HS, from the EC surface reduces the cellular response to mechanical stimuli, such as shear-regulated NO production (35, 84). Moreover, particularly HS, is known to mediate binding of chemokines, cytokines, enzymes, growth factors and other bioactive

molecules (60). HS is known to bind strongly to L-selectin (64, 91) and weakly to P-selectin (64, 91, 94), tethering molecules expressed on circulating cells. These factors play a crucial role in the initial selectin dependent tethering step of leukocyte adhesion to the endothelial wall.

1.3 The ESG as a Transducer of Mechanical Signals

The ESG is known to function as a mechanical transducer. For this to happen, it is believed that the ESG must maintain flexural rigidity (5, 39, 48, 93, 135, 141), or simply the resistance offered by a structure while it is undergoing bending. When a linear elastohydrodynamic model had been applied the value of the flexural rigidity was said to be around 700 $pNnm^2$ (141). A more accurate nonlinear elastohydrodynamic model placed this value at about 490 $pNnm^2$ (48). The elasticity of the ESG has also been analyzed via AFM (8, 95, 96). When using a two-layer composite compliance model the ESG is found to be 0.3 Kpa (95), or about 0.39 KPa when using the standard contact mechanics models for single layer materials (8). However, the ESG, as wells as cells in general, are not recognized to comply with any known contact mechanics models (95, 96) causing many anomalies in the data. Therefore, reliable results for this value have not yet been elucidated.

The substantiation for the ESG as a sensor for mechanical perturbation has come from experiments performed in the late 1990 and early 2000's. The first experiments selectively removed ESG components under enzymatic digestions and then reassessed its structural integrity and organization under flow (128, 144). Later experiments had discovered that when HS or HA are degraded specifically, ECs would fail to produce

nitric oxide (NO) under flow conditions (35, 84). Further proof for the ESG as a mechano-receptor is offered by the fact that removal of HS or HA completely will almost completely inhibit flow-induced NO production but will not affect receptor-mediated NO production by bradykinin and histamine, thus suggesting that the ESG has a direct effect on the NO production mechanism (98).

NO regulates many important functions such as blood flow, leukocyte-endothelial interactions, platelet adhesion and aggregation, and vascular smooth muscle cell proliferation. NO is produced by endothelial nitric oxide synthase (eNOS) by oxidizing the substrate L-arginine to L-citrulline and NO (36). The production of NO consists of two phases (15): a rapid phase and a sustained phase. It has been shown that rapid production of NO is dependent on Ca^{2+} intake, where as sustained NO production is independent of Ca^{2+} (35).

The potential mechanism for exactly how the ESG works as a mechano-sensor for NO production is still not well understood. What is important to note is that when the ESG remains undamaged, flow of blood in the area where the ESG is located is governed by the Brinkman equation not the Navier-Stokes equation. The Brinkman includes both effects of the ESG as well as the viscosity of the fluid. The Navier-Stokes equation only governs the viscous flow in the central region of the vessel that is sufficiently far from the wall. Therefore, the force that is acting on the EC surface is not the shear force; this is basically zero at the bottom of the ESG. The EC will actually undergo a torque that originates from the flow-induced drag force that is acting on the ESG (113, 141).

The proposed mechanism for ESG to transduce mechanical signals into NO can be placed into two groups: Decentralized and centralized (24). The decentralized model is based on the idea that the proteins such as syndecans which contain attachment sites for HS and CS will distribute force throughout the EC via the physical connections that syndecans have to the cytoskeleton (129). However, this has been refuted experimentally (32). The centralized model relies on the co-localization of the protein-GAG complexes CD44-HA and glypican-1-HS along with eNOS in the lipid rich invaginations known as caveolae. Many other signal molecules are located here (127) and it is believed that local tension in this location may activate eNOS. Despite these discoveries and theories, the detailed mechanism by which ESG mediates shear-induced NO production remains uncertain.

1.4 The ESG as a Mechanical Controller of Adhesion

The ESG, in the context of a buffer, is known to prevent cell-cell adhesion between leukocytes, monocytes and other circulating blood cells to the endothelial wall (17, 45). It also has been seen to repulse red blood cells (134) as well as platelets (135); affects that are all attenuated after ESG degradation (17, 45, 134, 135). However, it is in the context of leukocyte adhesion that the ESG is the most interesting; it appears to play a dual role (104) that may be due to several factors. On one side the ESG repulses leukocytes while on the other it contains leukocyte adhesion molecules such as ICAM-1 and VCAM-1 (104). It has been seen that after removal of HS from the ESG an increase of adhesion between leukocytes to the endothelium will be seen (17, 71). Furthermore, when the inflammatory cytokine TNF-α is introduced, the same affect is prevalent (17,

52). The spatial arrangement of the ESG may be the cause of this. Since the ESG appears to be patchy (4, 123) and is much thicker, about 0.4 μm (44, 76, 96, 134), than some adhesion molecules are tall, such as P-selectin at about 38 nm (121) or αIIbβ3 at about 20 nm (145) both of which are found on platelets. Therefore, when the ESG is altered by TNF-α or digestive enzymes such as heparanase the ESG may no longer shield the adhesion molecules. There is also evidence that activation of ECs by TNF-α, is widely believed to change the properties of the ESG (109, 118) and cause it to lose its non-adhesive attributes (17, 45). Here the ESG is believed to become a ligand for selectins, thus actively participating in adhesion. At this juncture, the ESG dependent forces and the density of interacting ligands involved in this process have yet to be clarified.

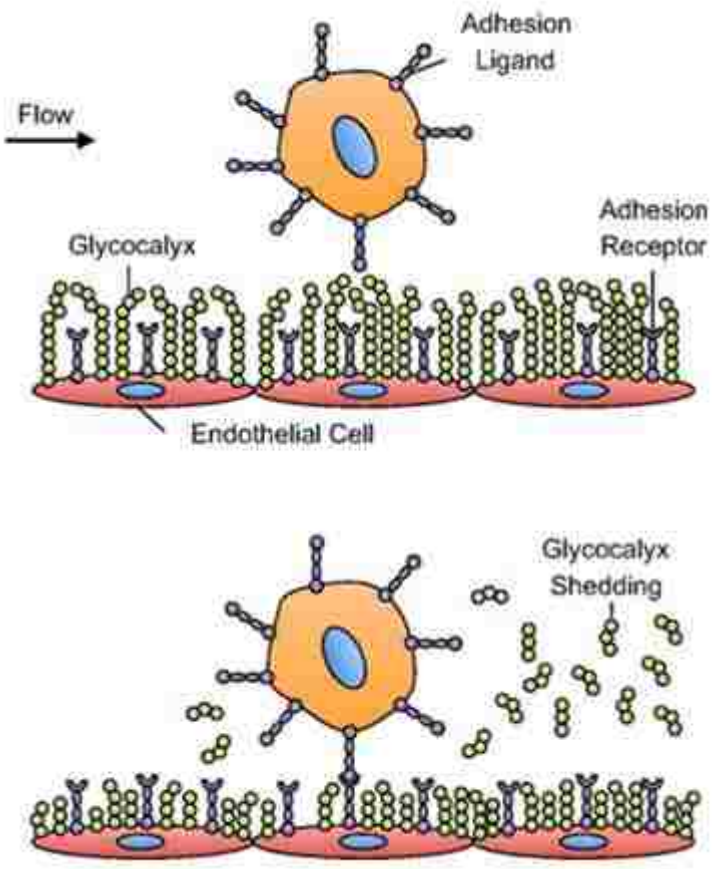

Figure 1.3: The effects of ESG shedding on cell adhesion. (A) Demonstrates interactions between a leukocyte and the endothelial wall under normal ESG conditions. (B) The ESG is being shed, exposing adhesion receptors and allowing the capture of a circulating leukocyte. This image was adapted from Mitchell, M.J, et al. Physical Biology in Cancer. The role of cell glycocalyx in vascular transport of circulating tumor cells. Am J Physiol Cell Physiol. Doi:10.1152/ajpcell.00285.2013 (83).

1.5 The ESG in Disease

The importance of ESG research comes from its role in disease. A well functioning ESG is required to provide a one of the most important multifunctional coatings in the human body. It is important for transducing fluid shear stress into vasorelaxation, maintaining of the proper permeability of the endothelial wall, and the controlling of cell-cell adhesion during inflammation. When the ESG is altered it loses these important

qualities as ESG degradation is seen to be a parallel in diabetes, arteriosclerosis and sepsis.

It is now well understood that the ESG is compromised in diseases such as diabetes (3, 88). The onset of diabetes is marked a failure of the pancreas to produce insulin which is known to cause disruptions of the ESG at the vascular wall (88). Furthermore, a lack of ESG disrupts NO production (30) which may lead to the high blood pressure seen in diabetics (12, 105). Although this pathway seems axiomatic the link between the three aforementioned aspects has not yet been established. A study analyzing blood plasma levels of hyaluronan and hyaluronidase showed that patients with diabetes exhibited increased synthesis and shedding of hyaluronan under hyperglycemic conditions and that this coincided with a reduction in the ESG (92). Given this information it is imperative to further analyze the role that ESG destruction plays in diabetes.

In such cases as arteriosclerosis the ESG is also rearranged. Atherosclerosis is a disease in which high plasma levels of LDL tend develop preferentially at sites in which turbulent flow profiles are present. When these atherogenic lipoproteins are retained, there is a local inflammatory response which will direct the development of sub-endothelial plaques (74). It has been shown that oxidized LDL can disrupt the ESG and lead to platelet adhesion (133) as well as leukocyte adhesion (17). Furthermore, a reduction in ESG height is also seen when mice are fed a high-fat high-cholesterol diet. This also coincided with a reduction of the ESG at sites with higher atherogenic risk

(133). In the future it is important to determine whether these ESG affects are the cause of or symptom of arteriosclerosis. This will inevitably lead to better treatment.

Infections and injuries found in tissue are known to illicit an inflammatory response, which is the manner in which the body regains homeostasis. This is a complex four stage process that first requires chemoattractants and cytokines such as TNF-α to be produced in the same region as inflammatory area. This leads to what is known as activation of the endothelium. However, at times this response may lead to chronic inflammation, shock, multisystem organ failure, and even death (120). Furthermore, since TNF-α is known to alter the ESG (110, 118) and cause it to become adhesive (17, 45) there exists a direct link between the above disorders and an unhealthy ESG. Patients with meningococcal meningitis, septicemia, or both that have serum TNF-α levels over 440 u/ml are likely to die of septic shock (137). Sepsis is a runaway inflammatory response do to the body's reaction to infection that causes the body to damage its own organs and can potentially be deadly (115, 137). Since sepsis coincides with an increased level of TNF-α (120, 137), which damages the ESG (110, 118) ongoing research in this area is key to patient survivability.

This collection of studies seeks to clarify the role of the ESG as a mechanical transducer and a mediator of cell-cell interactions. Both of these goals play a crucial role in the understanding the mechanisms that are highlighted diseases. Once these mechanisms are more fully understood better treatments may arise.

1.6 Transient Receptor Potential (TRP) Channels

TRP channels are members of a super family of cation soluble channels that display a large diversity is cation specificity (132). In the context of this thesis we have focused on the TRPP and TRPC family of channels.

TRP channels can be broadly divided into the two groups, simply referred to as groups 1 and 2. The reasons for dividing TRPs into groups 1 and 2 is based predominately on differences that arise do to topology and sequence. TRPC channels belong to group 1, along with TRPV, M, A and N. These channels most closely resemble the original TRP channel, Drosophila TRP (85). TRPP channels are a group 2 TRP channel. The only other known TRP channel currently placed in this group is TRPM.

Group 1 TRPs are placed in this group due to two key features. These features are as follows: All group 1 TRP channels have six transmembrane domains and the cat-ion soluble pore is located between the fifth and sixth transmembrane domains. TRPC, M and N also contain a TRP domain that is located underneath the sixth transmembrane segment. Group 2 TRPs share homology over the transmembrane section as well. For these channels there are also six transmembrane domains. However, the first and second domains are separated by a loop that is much larger than seen in group 1 TRPs (Fig 1.4).

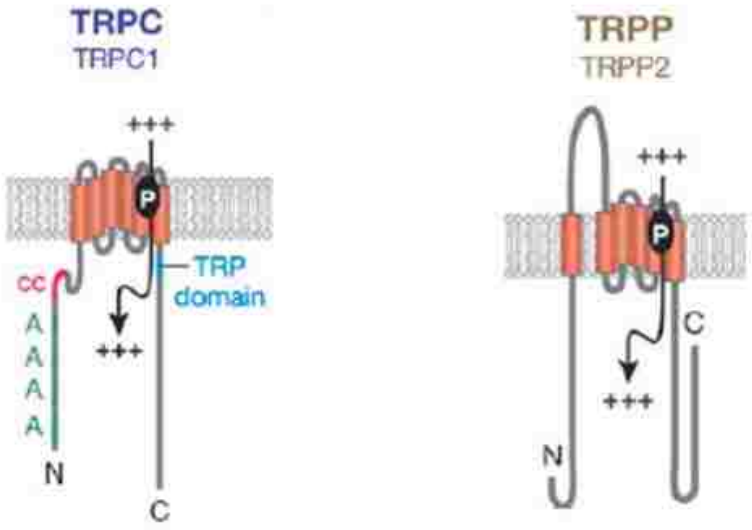

Figure 1.4: TRPC1 and TRPP2. The two members of the TRP super family that are displayed above are TRPC1, of group 1 and TRPP2 of group 2. The domains that are specified are: A, ankyrin repeats; cc, coiled-coil domain and the TRP domain. The red rectangles refer to the transmembrane domains and P refers to the pore loop which forms the channel that accepts cations (+++). The gray layer represents the lipid bi-layer this image has been adapted from Montell C, et al. Molecular characterization of the Drosophila TRP locus: a putative integral membrane protein required for photo transduction. Neuron. Doi:1313-1323. 1989 (85).

As mentioned before, the TRPP channels are designated as a group 2 subfamily within the hierarchy of TRP channels (132). We focused on observing the affects of TRPP2 (polycystin-2 or PKD2) channels, which are soluble to Ca^{2+}. Activation of TRPP2 is thought to occur via mechanical gating (132), as seen in flow experiments on cultured kidney cells (89) while other TRP channels such as TRPP3 has been reported to be a voltage-modulated, Ca^{2+}-activated nonselective cation channel (75) which is also known to be permeable to monovalent organic cations (21). Moreover, the presence of TRPP proteins on both motile and primary cilia could render them capable of sensing fluid flow as well as mechanical stretch (132). This is further elucidated by horizontal cell stretching experiments on endothelial monolayer's (11).

The TRPC channels are designated as a group 1 TRP within the hierarchy of TRP channels. For this thesis we have focused on TRPC1, an extensively expressed TRPC channel in mammalian species (153).TRPC1 can be found in the caveolae, lipid-rich invaginations in the cell surface that are formed by Cav-1, a protein that directly binds TRPC1 (101, 126). All known TRPC channels require phospholipase C (PLC) for activation. Although PLC can be activated by Ca^{2+} to cleave phospholipids the selectivity of TRPC channels to Ca^{2+} can vary (132). Despite this, it is known that TRPC1 can have Ca^{2+} solubility induced via mechanical stretch induced across the lipid bilayer (46, 80).

TRP channels typically assemble into homo- and/or hetero-multimers, particularly tetramers (149). The hetero-multimeric structures that TRP channels form is typically with channels that are similar to one another, i.e. TRPC1/TRPC5 (132). However, the forming of hetero-multimeric channels is not always restricted by channel similarity. TRPC1 and TRPP2 are known to form hetero-multimeric channels with one another (101, 149). Furthermore, the multimeric components of the channels are known to affect the functionality of the unit that they form (149). When TRPC1 and TRPP2 form a hetero-multimeric tetramer, TRPC1 seems to be the dominate channel when the tetramer is activated. Furthermore, addition of amiloride will reduce but not abolish the function of the TRPC1/TRPP2 hetero-multimeric tetramers (7, 149). The formation of hetero-multimers of TRPC1/TRPP2 may have significance in the mechano-sensation of fluid flow (130).

Chapter 2: the AFM

2.1 Introduction to AFM

The AFM is a highly sensitive mechanical device that can be utilized across a wide variety of scientific applications including imaging, force measurements and manipulation of micron sized objects (42, 56). A basic AFM consists of three main components: A cantilever (a word often interchangeable with probe), a laser and a piezo. The cantilever, typically made of silicon nitride, is moved via piezo actuation in the X, Y or Z directions. A piezo is simply a piece of ceramic or quartz that expands in a precise and controllable distance under the application of voltage. For this discussion on AFM we will restrict the direction of the cantilever to move only in the Z direction. The laser is focused on the cantilever and allowed to reflect into a quadrant photodiode. Therefore, as the cantilever deflects its motion can be monitored (Fig 2.1).

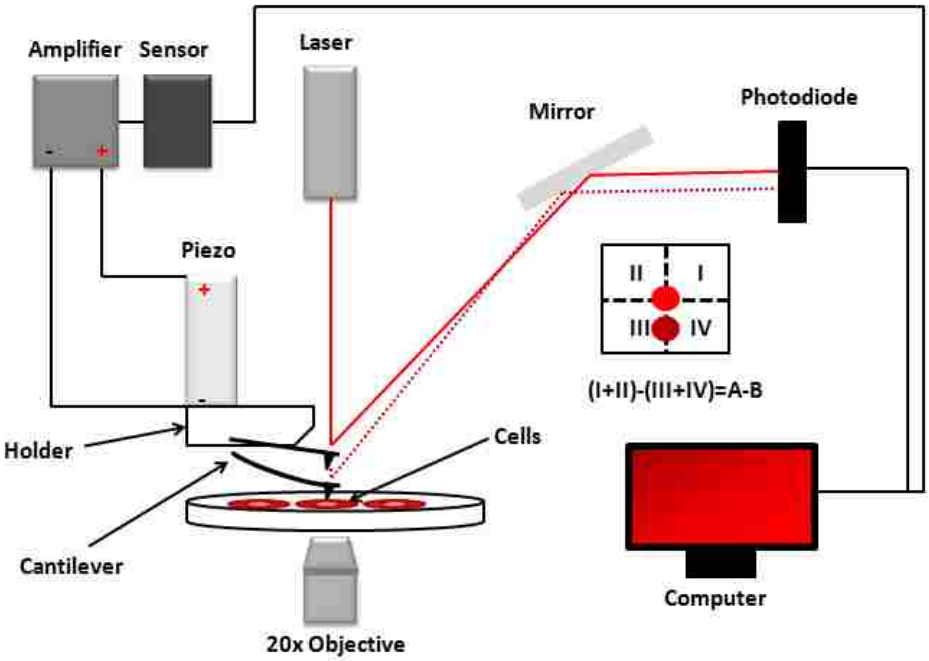

Figure 2.1: Detailed AFM schematic. Represented above is a cartoon that details the basic components of an AFM: The cantilever, the laser and the piezo as well as the additional components that are required for the instrument to function. The addtional components are the amplifier that provides the voltage that expands the piezo in the Z direction, the sensor that tracks this expansion and the mirror that allows the laser to be centered or "zeroed" in the diode. This AFM is shown with a 20x objective being used to view a sample of cells that are being manipulated by the AFM's cantilever. The solid laser trace refers to the path of the laser before the cantilever deflects and the dotted laser trace refers to the laser path after the cantilever deflects. The quadrant insert refers to the four quadrants of the quadrant photodiode. The" zero" is calculated by (I+II)-(III+IV) = A-B. This removes the tracking of any torsion motion of the cantilever, which is considered to be minimal. The value A-B is set to zero before an experiment takes place and all of the data gathered by the sensor and the diode are sent to a computer for downstream processing.

When AFM is used for imaging the cantilever is typically operated in what is known as contact mode or tapping mode. In contact mode the cantilever is simply brought into contact with a surface and raster scanned across the sample while the laser tracks the deflection of the cantilever. From this, the topography is mapped. In tapping mode the cantilever is vibrated at its fundamental frequency and is allowed to tap the

sample such to map the topography. Tapping mode has several advantages over contact mode. The most obvious is that it does not damage delicate samples. It can also achieve higher resolution. However, it has the drawback of taking a longer time to produce an image.

AFM can be used to measure atomic bonding, Van der Waals forces, and Casimir forces, dissolution forces in liquids and single molecule stretching and rupture forces (53). This is a technique known as force spectroscopy. Typically, a cantilever will be coated with a protein or other material that interacts with a protein or other material coated to a surface or expressed on cells placed under the AFM. Hundreds of interaction forces are typically observed. This data can then be used to deduce parameters such as on and off rates (k_{on} and k_{off}) as well as the energy barrier width associated with a variety of proteins via equations such as the Bell model.

The AFM that will be discussed in throughout this thesis is capable of force measurements and manipulation of micron sized objects. Although this context is broad this thesis focused on using the AFM to mechanically pull and push on cells to either monitor the downstream NO response or to observe the changes in elasticity, respectively. To pull on the cells the AFM probe can be coated in a variety of proteins that interact with the cell surface. This is similar to what is done in force spectroscopy experiments except conditions that produce only single protein interaction are not required. To push on the cells and derive the elasticity, a process known as nanoindentation, two methods could be used. The cantilevers could either be left in their stock form, where underneath the end of the cantilever there is a pyramid shaped

tip that can be pushed into the cell or have a micron sized bead attached to the end of the cantilever that will be pushed into the cell.

As mentioned before AFM probes are typically made of silicon nitride. They come in many varieties and are often chosen based on the application for which they will be used. For example, fast tapping mode scanning; cantilevers that are shorter and stiffer are often used. For force spectroscopy or nanoindentation a cantilever that is longer and softer is typically preferred (Fig. 2.2). The AFM probes that were used throughout this entire thesis were of the longer softer variety and were purchased from Bruker, model MLCT.

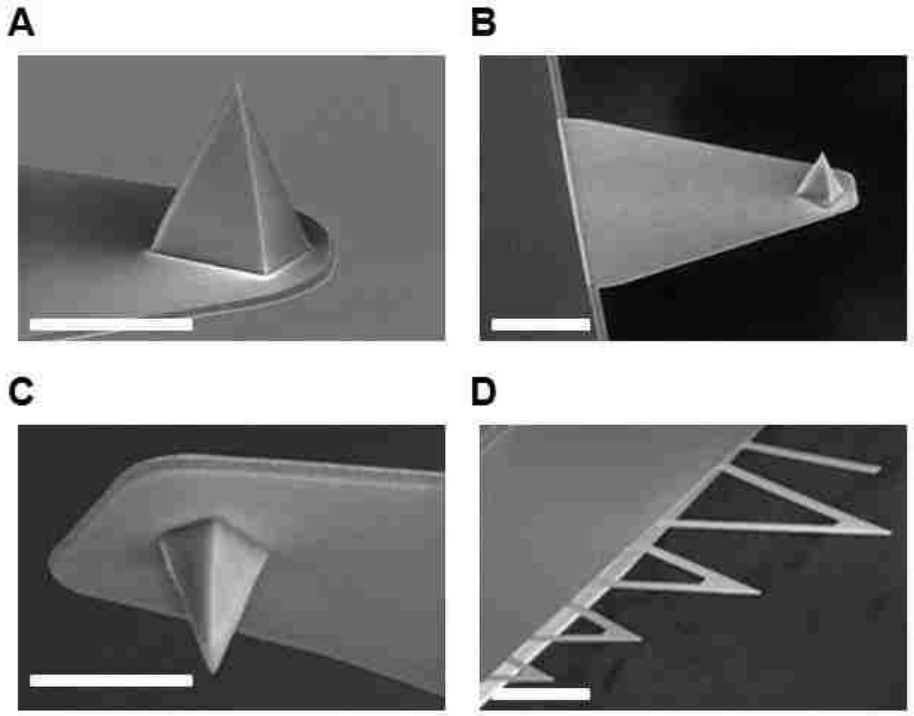

Figure 2.2: Types of AFM probes. These images are of two different AFM probes adapted from https://www.bruker.com. Panels A and B are EM images of a Bruker FASTSCAN-B. This type of probe is typically used for rapid contact mode imaging. Panels C and D are EM images of a Bruker MLCT probe. This type of probe is great for force spectroscopy or nanoindentation. The scale bars in A and C are 20 µm and the scale bars in B and D are 80 µm.

The AFM calibration can be done in a variety of manners. For the purpose of this thesis I will focus on a variation of a method known as thermal tuning (58). This process begins with pressing the cantilever against the surface of a culture dish, which was considered incompressible when compared to the cantilevers weak bending moment. This is done to determine the inverse optical lever sensitivity (InvOLS). The InvOLS was defined as a measure of the sensitivity that the photodetector had to the motion of the laser as it reflected off of the deflecting cantilever. This value was determined by the slope of the contact portion of the trace produced by the AFM as the probe touched the surface of the dish (Fig 2.3).

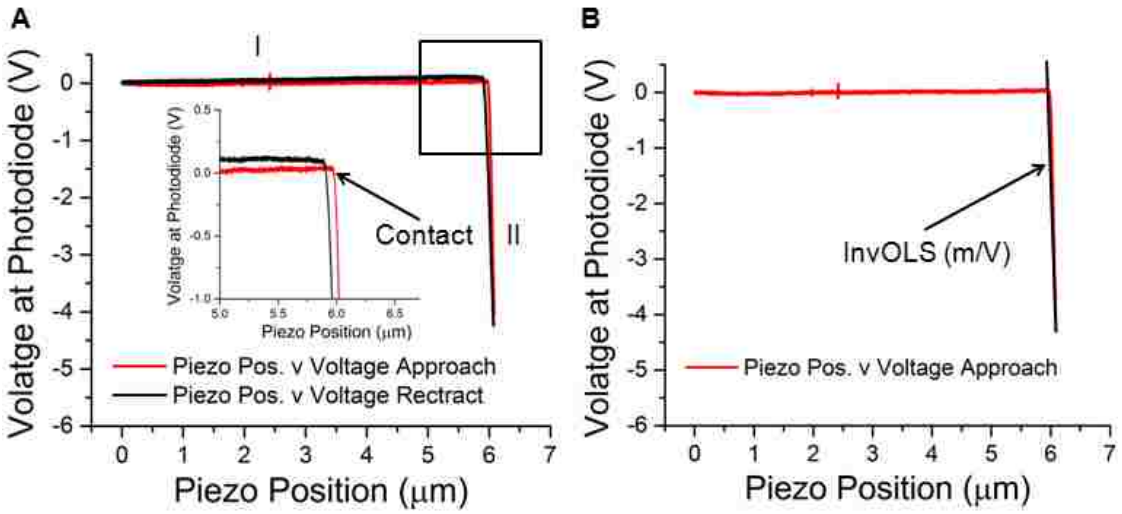

Figure 2.3: InvOLS. Panel A shows what the AFM scans look like during the calibration. The first part of the curve (I) is flat and the second part (II) curves sharply downward. Part (II) is the region in which the cantilever is in contact with the surface. Panel B graphically demonstrates the manner in which the InvOLS is found. It is important to note that the X direction of this plot refers to the Z direction that the piezo has moved.

Next, the random thermal fluctuations of the AFM probe were recorded as a function of time. The amplitude axis of the thermal fluctuations was then transformed into the position of the probe by multiplying the amplitude by the InvOLS, as the

amplitude of the thermal fluctuations is in V and the InvOLS is in m/V. This information was then transformed into the frequency domain by the methods of Fourier and yielded the resonance frequency peak of the probe. Using only the position points associated with resonance peak, a histogram could then be made of the probes position over time. The center of the bins from the histogram can then be averaged by taking the mean squared displacement (MSD). In equation 2.2 $\mathbf{x}_i(t) - \mathbf{x}_i(0)$ is a vector describing the distance that the cantilever traveled over a given time. Therefore, the MSD is simply the average of the magnitude of these vectors. Setting the equal partition therorem for a one dimensional oscillator equal to the energy for a one dimensional spring the spring constant k can finally be derived (Eq 2.5).

$$\frac{1}{2}kx^2 = \frac{1}{2}k_bT \qquad \textbf{Eq. 2.1}$$

$$MSD \equiv \langle x^2 \rangle \equiv \sum_i \langle \left(\boldsymbol{x}_i(t) - \boldsymbol{x}_i(0) \right)^2 \rangle \qquad \textbf{Eq. 2.2}$$

$$\frac{1}{2}k\langle x^2 \rangle = \frac{1}{2}k_bT \qquad \textbf{Eq. 2.3}$$

$$k\langle x^2 \rangle = k_bT \qquad \textbf{Eq. 2.4}$$

$$k = \frac{k_bT}{\langle x^2 \rangle} \qquad \textbf{Eq 2.5}$$

One more important aspect to note is that the distance the cantilever tip moves must be calculated. This is because the raw AFM data provides only the position of the piezo. The tip position can be easily found by performing the following calculation: Piezo Position-InvOLS*voltage at the diode, where InvOLS*voltage at the diode is normally

referred to as ΔZ. With the InvOLS in m/V and the spring constant in N/m, a change in voltage at the photodetector could now be converted into a force at the probe (Fig 2.4). PBS was utilized as the fluid in which the calibration took place.

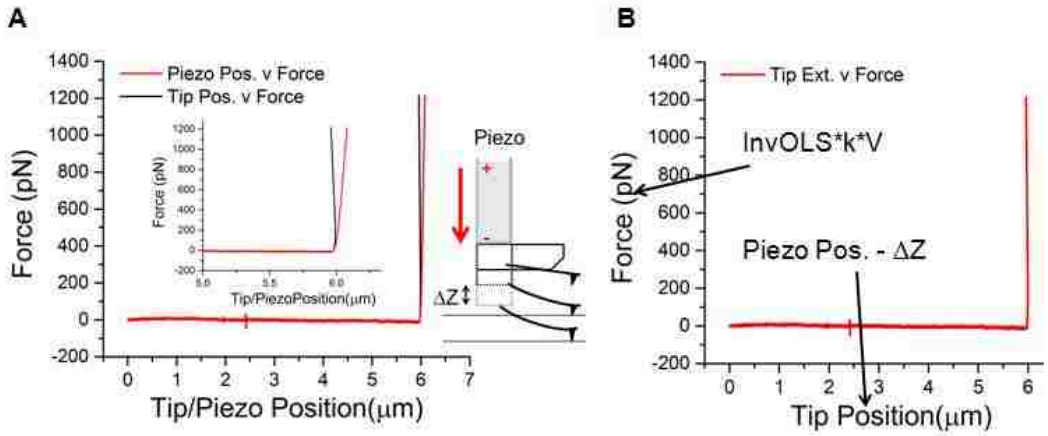

Figure 2.4: Conversion to force. Panel A shows how the AFM scan appears before and after the piezo position is converted into tip position for a single calibration scan. The insert shows the nature of the parameter ΔZ. From here it can be seen that this term can be described as the distance that the piezo travels after the tip has stopped traveling and the cantilever begins deflecting. Panel B shows an AFM scan that has under gone full corrections both for tip position and force.

*All of the following plots of AFM scans throughout this thesis will refer to the tip position (X direction shown on the plots above) simply as extension.

2.2 The Custom Built AFM

Much of this thesis was performed with an AFM that was constructed by Steven Wei (received PhD in biological engineering, 2014) and myself. This AFM was used for chapters 3 and 4, such to determine the mechanical pathway that governs the production of NO in endothelial cells. The AFM was entirely programmed in LabView and designed to be mounted atop a florescence microscope. This was done to have the

unique ability to take fluorescence images of cells while simultaneously delivering mechanical perturbations via AFM.

The AFM was built using a piezo from Physik Instrumente. The piezo was capable of a 0-60 µm range, however the AFM was restricted to move only 0-15 µm. This was to reduce the amount of change produced in the optical path between the cantilever and the photodiode, which can cause changes in the shape of the AFM scans. The A-B signal was calculated via an analogue position sensing amplifier produced by On Track Photonics. The main body of the AFM was built to spec in the Lehigh University machine shop and the laser was purchased as a custom built product from China. The A to D converted used was an NI USB-6210 data acquisition card from National instruments. Data could be read from this card a speed of 2 KHz. The AFM could achieve a resolution in the Y direction of about 20 pN and a resolution in the X direction of about 2 nm.

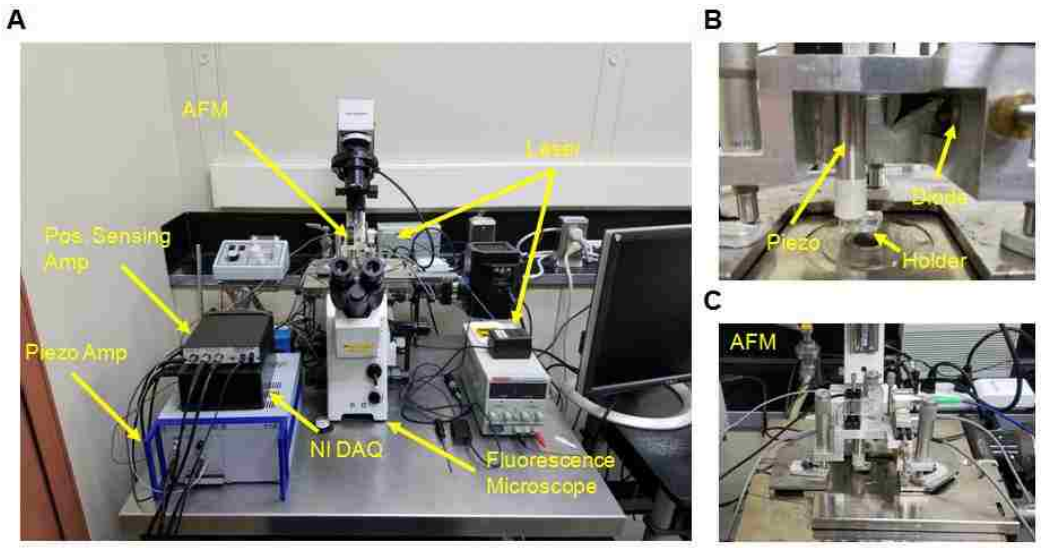

Figure 2.5: The custom built AFM. The AFM and all of its components were set up on air table (A). In panels B and C the holder, piezo and diode can be seen.

Chapter 3: Mechanotransduction of the endothelial glycocalyx mediates nitric oxide production through activation of TRP channels

3.1 Abstract

The carbohydrate-rich ESG found on the vascular endothelium, services critical functions in the mechanotransduction of blood shear stress. One of the most important protective functions of the ESG is to mediate the production of NO in response to blood shear. However, the detailed mechanism underlying ESG's mechanotransduction of the production of NO has not been completely identified. Herein, we used a combined atomic force and fluorescence microscopy approach to show that the ESG senses and transduces vertical mechanical stretch to produce NO. This rapid NO production is dependent on the presence of both HS and HA on ESG, as the removal of HS and/or HA leads to a significant decrease in NO production. Moreover, the production of NO is dependent on the intake of Ca^{2+} via endothelial Transient Receptor Potential (TRP) channels. Together, this study's results demonstrate the molecular mechanism of rapid production of NO in response to vertical mechanical stretch.

3.2 Introduction

Previous studies have demonstrated that the two major ESG components HA and HS cause a reduction in cellular response to mechanical stimulus (35, 84). Still, no clear mechanism has emerged. This project aims to characterize the mechanical sensing and transducer abilities of the ESG by means of AFM. Our AFM techniques have demonstrated that mechanical stimulation of HA and HS will result in increased NO

production. Moreover, that there is a synergistic relation between the HA and HS as simultaneous stretching of the two components will induce greater NO production stimulating than HA and HS alone. As a result, the study focused on two aims. The first aim demonstrated the vertical stretching force implemented on cell surface will induce NO production in a significant fashion in endothelial cells if and only if both HA and HS are present. The second aim of this study illustrated that HA and HS mechanically prime TRPP channels to intake Ca^{2+} and in turn cause an up-regulation of NO production when HA and HS are present on the cell surface that is being mechanically stretched.

3.3 Additional Background

NO, one of the most important protective molecules in the vasculature is produced by eNOS. A well-functioning eNOS oxidizes the substrate L-arginine to L-citrulline and NO. This normal function of eNOS requires dimerization of the enzyme, the presence of the substrate L-arginine and the cofactor 6R- 5,6,7,8-tetrahydro-L-biopterin (BH4), a powerful, naturally occurring reducing agent (36). NO produced by eNOS regulates vascular tone, blood flow, leukocyte-endothelial interactions, platelet adhesion and aggregation, and vascular smooth muscle cell proliferation (16, 96). The eNOS shares a binding site with caveolin-1 (Cav-1) (34) where the Cav-1 acts as a negative regulator of eNOS function (27). Upon stimulus dependent activation of ECs, Cav-1 negative regulation of eNOS is overpowered by Ca^{2+}-calmodulin (CaM) and the eNOS activity is up-regulated (82). These Ca^{2+} channels are located in the caveolae which are cellular invaginations enhanced by cholesterol and sphingolipids and are present in multiple cell types (39). A number of other ion channels and transporters have been localized to

caveolae including Na^+ channels, pacemaker channels (HCN_4) in the heart and the Na^+/Ca^{2+} exchanger (NCX1) (9, 39). Also, inside the caveolae are the proteoglycans transmembrane CD44 and glypican-1 which bind to the GAGs, HA and HS respectively (39). HA and HS are well defined to be mechanical sensors and transducers (35, 84) and are likely pulling on the CD44 glypican-1 by nature of their connection.

3.4 Materials and Methods

Cell culture: Immortalized rat brain endothelial cells bEnd.3 purchased from American Type Culture Collection (ATCC) 10801 University Boulevard Manassas, VA 20110 USA were cultured in DMEM medium (ATCC) supplemented with 4 mM L-glutamine, 4500 mg/L glucose, 1 mM sodium pyruvate, 1500 mg/L sodium bicarbonate, 1% penicillin streptomycin and 10% fetal bovine serum. The cells were grown in Corning t-25 flasks at 37 °C in a 5% CO_2 atmosphere and plated for experiments in 35 mm Cyto-One culture dishes (US Scientific). The experimental buffer used was a HEPES buffer containing 135 mM NaCl, 5 mM KCl, 1.5 mM $CaCl_2$, 1 mM $MgCl_2$, 100 mM glucose, 10 mM HEPES and 1% FBS, pH 7.3.

Enzymes: To remove ESG, bEnd.3 cells were treated with heparinase I & III (blend from *Flavobacterium heparinum*, Sigma-Aldrich) at a final concentration of 25 mU/ml and/or hyaluronidase (from bovine testes, Type I-S, Sigma-Aldrich) at a final concentration of 20 µg/ml for 90 minutes prior to experiments.

TRP Blocker*:* Amiloride hydrochloride was obtained from Sigma-Aldrich and applied to the cells at a final concentration of 100 µM.

Amino Acids: Poly-L-lysine (PLL) was obtained from Sigma-Aldrich.

Cell Stains: The NO fluorescent indicator DAF-FM diacetate was obtained from Life Technologies and applied to the cells at a final concentration of 5 μM for 90 minutes prior to experiments at 37 ^{o}C.

Atomic force microscopy (AFM) instrumentation: For this study, we used a custom-built AFM with fluorescence imaging capabilities to vertically stretch the glycocalyx. This AFM was mounted on an Olympus IX71 inverted fluorescence microscope, as shown in Fig. 2.1A. The tip/cantilever was mounted on a stacked piezo translator, which generated vertical movements of up to 15μm. Custom LabView software was used to control the movement of the piezo translator and timing of the measurements. The detection limit of this AFM was in the range of 10pN. To maintain the samples at 37 °C, a custom temperature control device capable of stably controlling the temperature at 37 °C within 0.1 °C was used for the duration of the experiment.

AFM pulling assay: The AFM probes used in this work were Bruker MLCT-O10 tipless nitride levers. To use these probes on the negatively charged ESG, the probes were coated overnight with poly-L-lysine at a concentration of 50 μg/ml in 0.2 M solution of $NaHCO_3$ (pH 9.0) at 4 °C. On the day of the experiment, the bEnd.3 cells were loaded with DAF-FM at a concentration of 5 μM. This was accomplished by first washing the cells with the experimental buffer 3x to remove the culture medium and adding 2ml of the experimental buffer in the culture dish. The cells were then loaded with DAF-FM, wrapped in tin foil and incubated for 90 min. After removal from the incubator, the cells were washed 3x with the experimental buffer and allowed to sit at room temperature for 15 min before the experiment began. This procedure was performed in low light

conditions to mitigate the effects of photo bleaching. In some experimental groups, the treatment with heparinase I & III and hyaluronidase treatment took place concurrently with DAF-FM loading.

To conduct the experiment the cells were first placed under the AFM for 15 minutes to insure that both the cells the AFM cantilever are equilibrated in the experimental buffer. During the experiment the AFM probe was aligned over a single bEnd.3 cell and depressed into the cell. During contact the probe had electrostatic interactions with the glycocalyx. As the probe was retracted it was held at a constant force for an average of 80 seconds. This allowed for mechanotransduction to take place, leading to NO production. Fluorescent images were taken before and after the vertical mechanical stimulation of the single bEnd.3 cell. The data was analyzed in Image-J by taking into account the area of the cell the background of the image and the integral density of the cell. The formula used is: (Integral density of Cell)-(Background)*(Area of Cell). A paired T-test was performed on the normalized florescence intensity of the cells before and after mechanical stimulation. Typically, more than 15 cantilever-cell pairs were recorded for each experimental condition.

Parallel plate flow chamber assay: The assay was conducted using a parallel plate flow chamber obtained from GlycoTech (Rockville, Maryland) connected to an Infusion Withdrawal Syringe Pump (Harvard Apparatus, Holliston, MA). Confluent bEnd.3 cells cultured on 35 mm culture dishes were first loaded with DAF-FM and subjected to shear stress at 20, 25 and 35 dynes/cm^2. NO production was monitored using the IX71 fluorescence microscope.

2.5 Results

As shown in Fig. 2.1, the AFM pulling assay was conducted using a custom-built AFM mounted on an inverted fluorescence microscope. For the single-cell pulling assay (Fig. 1A), a tip-less micro-cantilever probe coated with poly-L-lysine, a cationic polypeptide that binds to the glycocalyx, is controlled to move in the vertical direction using a piezoelectric translator. The laser light is aligned over the probe and reflected into the quadrant photodiode to track the movement and force of the cantilever. The AFM detection system used a 1040-nm infrared laser, which does not interfere with simultaneous fluorescence imaging with the fluorescent dyes DAF-FM used in this study. The bEnd.3 cells were cultured on a tissue culture dish and labeled with DAF-FM, an NO-specific fluorescence dye, prior to the experiments. Fig. 2.1B shows a typical force application profile. First, the cantilever was positioned above the center of an endothelial cell. Expansion of the piezoelectric translator lowered the probe onto the cell surface. Following probe–cell contact, further expansion of the translator pressed the probe against the cell. The compression force on the cell was determined from the upward deflection of the cantilever and was set at 280 pN for two seconds. Once this force value was reached, the expansion of the translator ceased. The probe was subsequently retracted from the cell. Probe-cell interaction due to the adhesion to the glycocalyx led to the stretching force applied onto the cell. After this presetting, a 50 pN stretching force is reached; the probe ceased to retract and stayed in the same position to allow continuous stretching to take place. After stretching for 80 seconds, the probe was retracted again to stop the probe-cell interaction. Simultaneous fluorescence

images were recorded by a CCD camera to monitor the change in the NO level inside the cell.

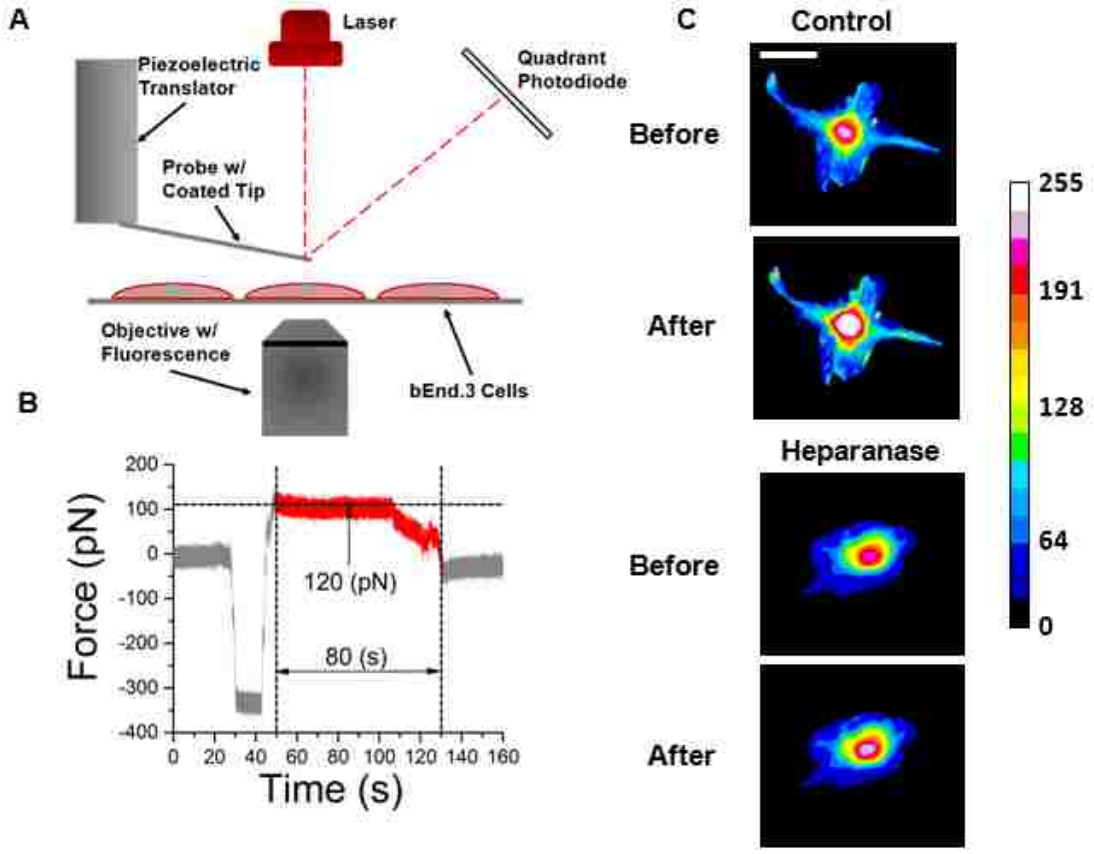

Figure 3.1: The AFM pulling assay. (A) A schematic diagram of the assay set-up. (B) Typical plot of force vs. time following normal stretching of the ESG using a poly-L-lysine coated cantilever. (C) Images of a single bEnd.3 cell stained with DAF-FM diacetate, before (Top) and after (Bottom) the ESG stretch, and without (upper) or with pretreatment of heparinases. Scale bars are 20 µm.

Fig. 3.1C shows that after stretching, the DAF-FM fluorescent intensity was typically much higher than that of the same cell prior to application of the force. Because the DAF dye intensity reflects the cumulative production of NO, the enhancement of NO production after stretching was quantified by subtraction of the

average fluorescence intensity of approximately 10 adjacent cells that were not under any mechanical perturbation.

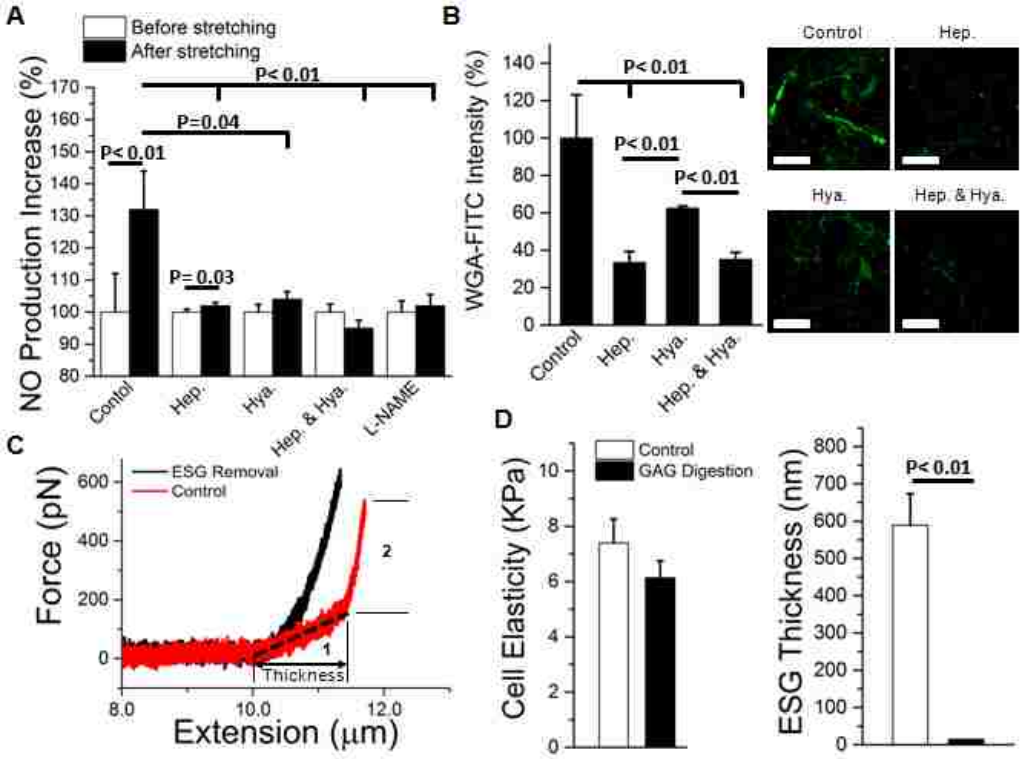

Figure 3.2: NO production is reduced after the removal of the ESG. (A) Percentage of increase in NO production after 80 seconds of stretching. The cells were either untreated (control) or treated with the indicated reagents prior to stretching. The error bar is standard error with N > 10 in each case. (B) GAG removal decreased the WGA-FITC fluorescence. The error bar is standard error with N > 10 in each case. Right inserts: representative fluorescent images of bEnd.3 cells stained with WGA-FITC, without (Control) or with pretreatment of heparinases (Hep.) and/or hyaluronidase (Hya.). Scale bar is 20 μm. (C) Quantification of thickness and stiffness of ESG by AFM nanoindentation. Regions 1 and 2 are indentation of ESG and plasma membrane, respectively. (D) The effect of GAG removal on ESG thickness and cell elasticity. The error bar is standard error with N > 10 in each case. P values are located in the plots.

Fig. 3.2A shows the averaged normalized intensity of NO fluorescence after stretching, which increased by approximately 40% relative to controls. bEnd.3 cells were subjected to an average force of 182 pN +/- 35 pN in the vertical direction using an AFM

probe coated with PLL, which has a net positive charge. It is assumed that the positive charge interacts with the net negative charge of the ESG, allowing electrostatic interaction between the two ions and the pulling force to occur. To confirm whether the DAF fluorescence is specific to NO production, the bEnd.3 cells were treated with L-NAME, a known eNOS inhibitor. Repeating the pulling after L-NAME treatment led to no increase in NO fluorescence intensity, indicating that NO was indeed produced by eNOS. To test whether this NO production is due to the stretching of ESG, the bEnd.3 cells were treated with heparinases and/or hyaluronidase to remove the HS and HA, two major components of ESG, respectively. Following heparinase and hyaluronidase treatment, the NO production decreased to 12.5% and 6.25%, respectively, compared to that of the control group. When both enzymes were used, the enhancement of NO production was completely abolished.

To confirm that the GAGs were in fact removed by the enzymatic digestions with heparinase I & III and hyaluronidase, the cells were stained using wheat germ agglutinin (WGA) before and after removal of the GAGs. After treatment of the cells with a concentration of 25 mU/ml heparinase I & III and 20 μg/ml hyaluronidase, they were washed 3x in the experimental buffer and stained with WGA at a concentration of 5 μg/ml in the experimental buffer for 45 min. The results showed a significant decrease in the fluorescence intensity (Fig. 3.2B). Additionally, an AFM indentation assay was conducted to determine the thickness and stiffness of the ESG (Fig. 3.2C). During the indentation scan, the AFM tip travels vertically towards the surface of a bEnd.3 cell. Upon indentation of the ESG, the AFM cantilever, serving as a soft spring, is deflected

(Fig. 3.2C). The deflection of the cantilever is measured and plotted as a function of the sample position along the z axis. The resulting curve is transformed into a force-versus-indentation curve using the cantilever's spring constant and the light lever sensitivity. The slope of the force indentation curve directly reflects the stiffness (expressed in pN/nm), which is necessary to indent the ESG for a certain distance. The first slope indicates the stiffness (in this tracing, 0.30 pN/nm) of the very first layer, which is the ESG. The second nonlinear region indicates the stiffness of the cortical membrane. Practically, the slope of the force indentation curve is deduced from a manually plotted regression line (similar to the line in the tracing) using MatLab. We found that ESG behaves as a linear spring, resulting in a single fixed stiffness value. The distance between the starting point of the ESG indentation and the starting point of the second slope (projected on the x-axis) corresponds to the thickness of the ESG. On average, the ESG thickness was found to be 0.589 +/- 0.08 μm before removal by heparinase I & III and hyaluronidase (68). After removal, the AFM was unable to detect the presence of the ESG (Fig. 3.2D). The second nonlinear region of the force-indentation curve was fitted to the Hertz model to obtain the cellular elasticity. The change in elasticity of the bEnd.3 cells before and after ESG removal was not statistically significant (Fig. 3.2D). Therefore, Fig. 3.2 demonstrates that the increased level of NO is produced specifically by eNOS and that an intact glycocalyx layer is required.

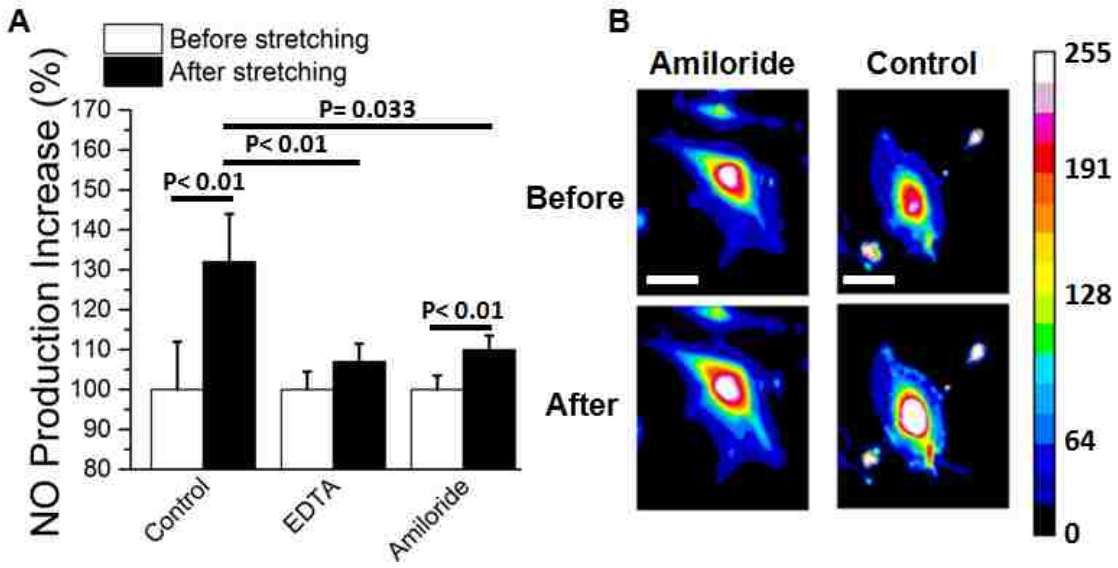

Figure 3.3: NO production is reduced after inhibiting TRPP channels. (A) The effect of 10 mM EDTA and 10 µM amiloride on rapid NO production. The error bar is standard error with N > 10 in each case. P values are located in the plot. (B) Images of a bEnd.3 cell stained with DAF-FM diacetate, before (top) and after (bottom) the ESG stretching, and without (right) or with treatment of 10 µM amiloride. Scale bars are 20 µm.

It has been reported that the rapid NO production in response to shear requires Ca^{2+} intake. To test whether Ca^{2+} is required for NO production, we loaded the bEnd.3 cells with DAF-FM as wells as an addition of 10mM EDTA, a calcium chelator. The Lack of NO production do to EDTA indicated that Ca^{2+} intake is indeed essential for the NO production. Moreover, ion TRP channels have been shown to be required in the rapid NO production during EC stretching (22, 106).Those studies, however, did not determine whether and how ESG may be involved in the NO production. To test this involvement, we added 10µM/ml of amiloride a blocker of the calcium permeable, TRPP family channels TRPP2 and TRPP3 (7, 11, 22, 151), before the AFM pulling assay. Similarly to EDTA, the addition of amiloride significantly decreased both Ca^{2+} intake and NO

production, suggesting that the Ca^{2+} intake is mediated by the activated TRP family channels.

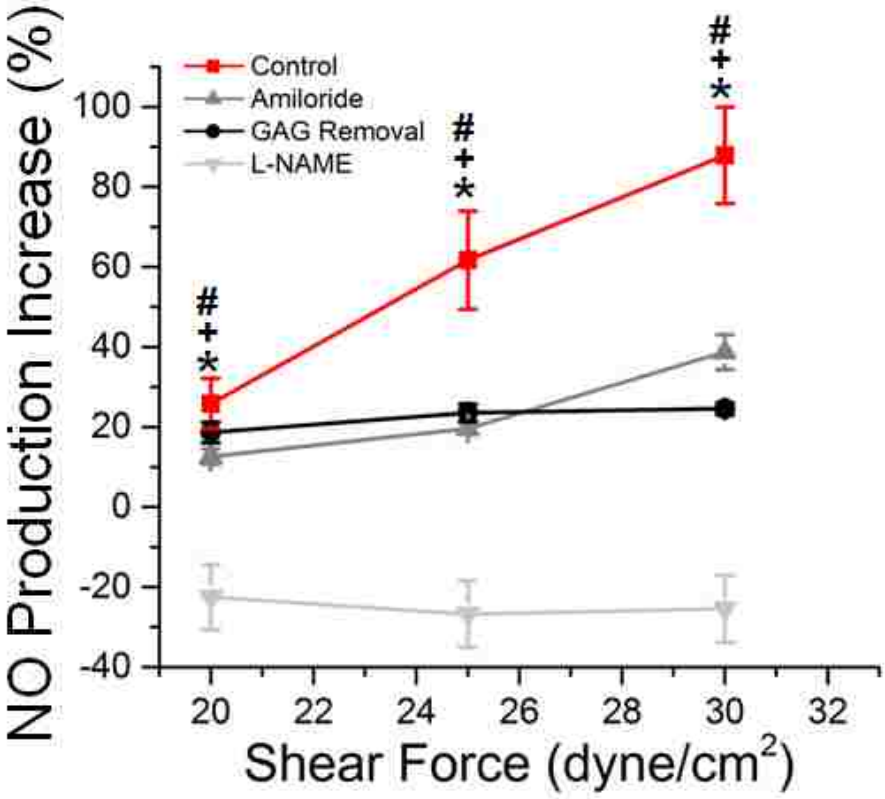

Figure 3.4: Flow-induced NO production observed in a parallel plate flow chamber. bEnd.3 cells were either untreated (control) or treated by the indicated reagents prior to the assay. The error bar is standard error with N > 10 in each case. *P<0.05 between L-NAME and Control, +P<0.05 between GAG removal and Control, #P<0.05 between Amiloride and Control.

Lastly, we sought to compare the NO production detected in our AFM assay and the commonly used parallel plate flow chamber assay (Fig. 3.4). Shear stress of 20, 25 and 35 dynes/cm^2 was applied to a confluent layer of bEnd.3 cells that was loaded with DAF-FM. The NO production was monitored simultaneously. The flow chamber assay clearly demonstrated that shear stress resulted in a significant increase in NO production and that the production was inhibited by GAG digestion, amiloride, and L-

NAME. Therefore, the NO production in response to vertical stretching appears to be controlled by the same mechanism as that of the shear stress stimulation.

3.6 Verification of GAG Removal

To verify the removal of the GAG HS from the surface of the bEnd.3s a wheat germ agglutinin (WGA) staining assay was performed. WGA, which in this case is an FITC conjugate, has the ability to recognize and bind to N-acetylglucosamine (70), a common (6, 106, 110, 114). It was stored as 1mg/ml aliquots at -20 ^{o}C. To obtain the data HS was first removed from the cell surface by heparinase I &III treatment at a concentration of 25mUN/mL for 1 hr 30 min at 37 ^{o}C in the culture medium. The cells were then washed with PBS 2x and treated with 5µg/mL of WGA for 10 min at 37 ^{o}C in PBS supplemented with 5% BSA. The cells were then washed again 2x in PBS and imaged on a Nikon C2si confocal microscope in PBS with 5% BSA. The images clearly showed a reduction in FITC fluorescence in the HUVECs treated with heparanase I&III. The same procedure was performed for the cells after 20µg/mL hyaluronidase treatment.

3.7 Discussion

In this work, we show that the ESG senses and transduces vertical mechanical stimulation in a fashion similar to shear forces. NO is produced rapidly and is dependent on the capacity of ECs to uptake Ca^{2+} via the TRP channels.

Many experiments performed on BAECs, HUVECs and bEnd.3 cells have demonstrated that ECs respond to shear flow and lateral stretch by producing NO (11, 35, 65-67). Under shear flow, the ECs respond in a biphasic manner, whereby the first phase is dependent on Ca^{2+} intake and the rate of change in the shear stress on the cell

while the second phase is Ca^{2+} independent and shear stress dependent (66, 67). However, this effect has not been shown to occur in Ca^{2+}-mediated NO production following stretch. Furthermore, in rat carotid artery endothelial cells, the TRPV channels activated Ca^{2+} intake and are directly related to NO production under shear flow conditions (65). In this experiment, vasodilatation was greatly reduced using 1 μmol/L RuR, the TRPV channel blocker. Moreover, TRPP2 has been implicated in both stretch-induced NO production by Ca^{2+} intake in bEnd.3 cells, simulating brain injury (11) and shear flow-mediated Ca^{2+} intake in renal epithelial cells (89). In the current study, we seek to ascertain a relationship between TRPP2 and the capacity of ESGs to initiate rapid NO production in bEnd.3 cells that is Ca^{2+} dependent and induced by vertical stretching on the ESG.

A recent molecular dynamics simulation study demonstrated that, under shear flow conditions, HS chains pull on syndecan-4, shifting their cytoplasmic domains from a vertical orientation to approximately 70° to 60° away from the horizontal (20). Additionally, there is a significant motion of these domains through the lipid bi-layer in the vertical direction. Furthermore, in endothelial cells, syndecan-4 cytoplasmic domains are believed to interact with transduction complexes as well as actin filaments. Therefore, it can be hypothesized that this cytoplasmic angling and vertical shifting will move the anchoring points of HS chains in the cytoskeleton, activating the biochemical machinery inside the cell (10, 20). We therefore believe that this machinery can be activated by vertical stretching, whereby HS chains pull on proteins such as syndecan-4, glypican-1 and others. This concept may also help explain why horizontal stretching of

bEnd.3 cells can trigger Ca^{2+} dependent NO production. However, this type of experiment differs from the current experiment in that the cytoskeleton tension is produced by pulling of the entire cell, whereas we place tension on the cytoskeleton by pulling on the ESG.

When compared to shear flow experiments, the seemingly low Ca^{2+} intake and NO production measured in the current experiment may raise a question. In the first five minutes of pulsatile shear flow at 10 +/- 15 dynes/cm^2, NO production increased to approximately 200% of basal levels and in steady shear flow at 20 dynes/cm^2, NO production increased to approximately 150% of basal levels (35). This observation may reflect the fact that the lever contacts roughly 1800 μm^2 of surface area and pulls to average forces on the order of 100 s of pN. This stimulus will result in a highly localized region of stimulation, activating a smaller area of the ESG. Furthermore, this finding lends a potential explanation for the resultant large decrease in NO production after removal of HS and HA; the less these key ESG components are stimulated, the less NO production there will be. Moreover, the demonstration that rapid NO production is induced by the rate of change in the shear stress (66, 67) may further explain why AFM has the ability to induce rapid NO production as well as explain why pulsatile shear flow can cause a greater increase in rapid NO production, as observed in some flow experiments (35).

A potential unifying theory that could explain our findings in the context of previous studies could be as follows. The reorganization of GAGs, proteoglycans and glycoproteins during horizontal or vertical stimulation of the ESG cause tension in the

lipid bi-layer, which is propagated throughout the EC due to the connections that some of the proteoglycans and glycoproteins have to the cytoskeleton. This in turn will cause a variety of mechanically sensitive ion channels, such as TRP channels, to accept Ca^{2+} ions. This is a plausible explanation based on the following argument. The GAG HS, as it attaches to its respective proteoglycan syndecan-4, can cause the reorganization of syndecan-4 through the lipid bi-layer and the cytoskeleton under shear flow conditions (20). This effect may also be observed in transmembrane glycoproteins such as CD44, which interact with the cytoskeleton (43) and harbor an attachment site for HA (39, 87). This tension in the lipid bi-layer, the cytoskeleton as well as the proteoglycans and glycoproteins may activate ion soluble TRP channels. The intake of these ions by TRPV4, TRPC1 and TRPP2 channels is known to coincide with vasorelaxation and stretch-induced NO production (11, 65). Additionally, it is known that the activation of eNOS, which produces most of the vasorelaxing NO, requires Ca^{2+} to upregulate its activity (25, 82). Ca^{2+} will then activate eNOS, and NO will be produced.

NO production depends on multiple factors, such as NOS expression, activity and substrate concentration. In addition, the half-life of NO depends on reactive oxygen species (ROS) (55). To verify if these other factors affect NO production or detection, we repeated the HS/HA removal study. Instead of using pulling force, the ECs were stimulated by calcium ionophore A23187, a potent eNOS agonist that bypasses the mechanotransduction step. As shown in figure 5, after treatment with A23187, the control, HS-, HA-, as well as HS-/HA- removal groups, resulted in similar level of enhanced NO production, which was inhibited by L-NAME. This experiment indicates

that HS and/or HA removal does not alter the NO production machinery, including substrate availability, G-protein activities (41), and eNOS expression in ECs, nor do the HS and/or HA removal alter the bioavailability due to potential change of ROS levels.

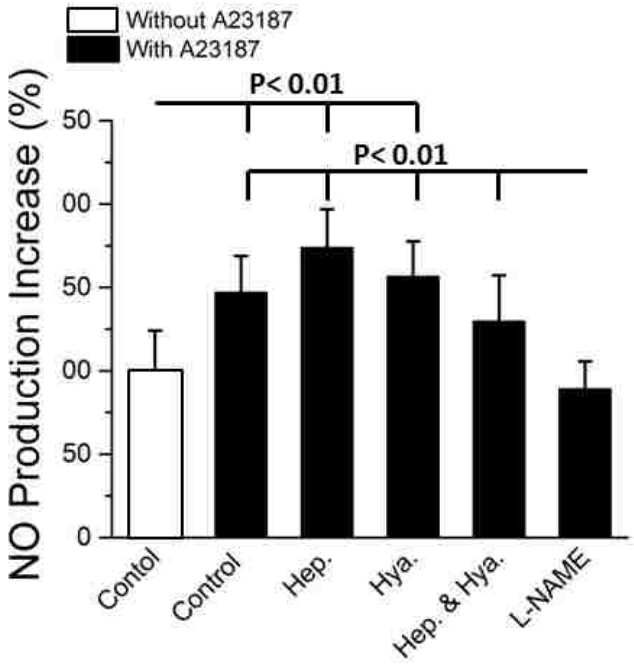

Figure 3.5: NO production induced by 1 μM of calcium ionophore (A23187). The error bar is standard deviation with N > 30 in each case. P values are located in the plot.

Further work needed to validate this hypothesis would entail demonstrating whether NO production, TRP channel activation and Ca^{2+} intake are predominately due to the reorganization of the transmembrane proteoglycans and glycoproteins in the lipid bi-layer. Furthermore, whether these transmembrane proteoglycans and glycoproteins cause this type of NO production by means of connections to the cytoskeleton will need to be verified. These studies will help demonstrate experimentally that the GAGs attached to transmembrane proteoglycans and glycoproteins such as CD44 and syndecan-4 are the first line for sensing in this transduction pathway. A better

understanding of this mechanism of vasorelaxation could potentially have broad-reaching applications with regard to therapy for renal dysfunction (136), diabetes (92), high sodium-based hypertension (68, 96) and pulmonary function (143).

Chapter 4: The ESG Core Protein Glypican-1 Activates TRPC1 and TRPP2 Channels to begin the NO Production Cascade

4.1 Abstract

The endothelial surface glycocalyx is a carbohydrate rich layer that is comprised of long oligosaccharide chains that are held to the cell surface via core proteins. These oligosaccharide chains and core proteins, namely HS and glypican-1 are known to be required for a well functioning ESG to produce NO under mechanical perturbations by produced flow. Despite these observations a clear picture of how these constituents are utilized by cells to transduce mechanical force into NO production has yet to be elucidated. This assay utilized cultured bEnd.3 cells (from rat brain endothelium) as a model system to show that the ESG core protein glypican-1 senses and transduces mechanical stretch to produce NO by activating TRPC and TRPP channels. To achieve this we have utilized a combined atomic force and fluorescence microscopy approach. In this system an antibody that recognized glypican-1 could be coated to probes used by the AFM, thus allowing the application of force to be applied to the protein directly. NO production could then be monitored by fluorescence before and after the application of force by the AFM. The results demonstrate that applying mechanical force to glypican-1 will result in rapid NO production. Furthermore, that this NO production can be completely inhibited by blocking TRPC channels and reduced by blocking TRPP channels. Together, our results demonstrate that the molecular mechanism of rapid production of NO is a result of glypican-1creating mechanical tension in the cell membrane, activating TRPC and TRPP channels.

4.2 Introduction

This assay investigated the role of the ESG in NO production by isolating the key components of the proposed mechanism outlined in chapter 1. It has been shown that ECs with RNA-silenced glypican-1 will have inhibited NO production under physiological flow conditions (31). Therefore, it was our goal to uncover the underlying mechanism that this observation is dependent on. Due to the fact that Glypican-1 is physically attached to HS, a known mechano-sensor required for NO signaling (35), the HS-glypican-1 complex will likely cause tension in the caveolae under mechanical perturbations. This tension will activate nearby TRP channels located within the caveolae via attachment to CAV-1. These channels are likely TRPC1 (2) or TRPP2, which form hetero-multimeric channels with TRPC channels (2, 26). TRP channels are known to allow Ca^{2+} into the cell and cause vasorelaxation in ECs (11, 38). We accomplished two specific aims to achieve this goal. The first aim was to mechanically stimulate glypican-1 independent of HS via AFM and monitor the NO production before and after mechanical perturbation. This directly demonstrated that glypican-1 is a mechanical sensor that leads to NO production. The second aim was to block TRPPC1 or TRPP2 and again use AFM to mechanically stimulate glypican-1 independent of HS. This exhibited the manner in which TRP channels are mechanically activated by glypican-1. Both of these aims were carried out by utilizing the same type of AFM assay used in chapter 2. However, anti-glypican was coated on the probe instead of PLL such to achieve the specificity and the probe was no held at a specific force clamp during retraction. This is because the antibodies could not be held for much longer than a few seconds. Knowledge of this

mechanism will at last provide a comprehensive bio-mechanical model for how ECs respond to blood flow with NO production.

4.3 Materials and Methods

Cell culture: Immortalized rat brain endothelial cells bEnd.3 purchased from American Type Culture Collection (ATCC) 10801 University Boulevard Manassas, VA 20110 USA were cultured in DMEM medium (ATCC) supplemented with 4 mM L-glutamine, 4500 mg/L glucose, 1 mM sodium pyruvate, 1500 mg/L sodium bicarbonate, 1% penicillin streptomycin and 10% fetal bovine serum. The cells were grown in Corning t-25 flasks at 37 °C in a 5% CO_2 atmosphere and plated for experiments in 35 mm Cyto-One culture dishes (US Scientific). The experimental buffer used was a HEPES buffer containing 135 mM NaCl, 5 mM KCl, 1.5 mM $CaCl_2$, 1 mM $MgCl_2$, 100 mM glucose, 10 mM HEPES and 1% FBS, pH 7.3.

TRP Blockers: Amiloride hydrochloride and SKF96365 were obtained from Sigma-Aldrich and added to the cells at a final concentration of 100 µM.

Cell Stains: The NO fluorescent indicator DAF-FM diacetate was obtained from Life Technologies and applied to the cells at a final concentration of 5 µM for 90 minutes prior to experiments at 37 ^{o}C.

Primary Antibodies: Anti-glypican-1, TRPC1 and TRPP2 primary antibodies were obtained from Santa Cruz Biotechnology and were diluted 1:100 in PBS for all experimental procedures.

Secondary Antibodies: To visualize the glypican-1, Alexa Fluor 546 anti-rabbit was purchased from Thermo Fisher Scientific Inc. To visualize the TRPC1 or TRPP2 Alexa Fluor 488 anti-mouse was also obtained from Thermo Fisher Scientific Inc.

Atomic force microscopy (AFM) instrumentation: For this study, we used a custom-built AFM with fluorescence imaging capabilities to vertically stretch the glycocalyx. This AFM was mounted on an Olympus IX71 inverted fluorescence microscope. The tip/cantilever was mounted on a stacked piezo translator, which generated vertical movements of up to 15µm. Custom LabView software was used to control the movement of the piezo translator and timing of the measurements. The detection limit of this AFM was in the range of 10pN. To maintain the samples at 37 °C, a custom temperature control device capable of stably controlling the temperature at 37 °C within 0.1 °C was used for the duration of the experiment.

AFM pulling assay: The AFM probes used in this work were Bruker MLCT-BIO-DC nitride levers. Anti-glypican-1 or Anti-HS was immobilized onto the AFM cantilever using a heterobifunctional polyethylene glycol (PEG) crosslinker, Acetal-PEG-NHS (Institute of Biophysics, Johannes Kepler University) according to a modified protocol developed by Dr. Hermann J. Gruber, Johannes Kepler University (http://www.jku.at/biophysics/content). Functionalized cantilevers were used for the AFM experiment within 8 hours.

On the day of the experiment, the bEnd.3 cells were loaded with DAF-FM at a concentration of 5µM. This was accomplished by first washing the cells with the experimental buffer 3x to remove the culture medium and adding 2ml of the experimental buffer in the culture dish. The cells were then loaded with DAF-FM,

wrapped in tin foil and incubated for 90 min. After removal from the incubator, the cells were washed 3x with the experimental buffer and allowed to sit at room temperature for 15 min before the experiment began. This procedure was performed in low light conditions to mitigate the effects of photo bleaching.

To conduct the experiment the cells were first placed under the AFM for 15 minutes to insure that both the cells the AFM cantilever are equilibrated in the experimental buffer. During the experiment the AFM probe was aligned over a single bEnd.3 cell and depressed into the cell. As the probe was retracted it created a rupture force between the antibodies and the glypican-1 on the surface of the cell. Fluorescent images were taken before and after the vertical mechanical stimulation of the single bEnd.3 cell. As before, the data was analyzed in Image-J by taking into account the area of the cell, the background of the image, and the integral density of the cell. The formula used is: (Integral density of Cell)-(Background)*(Area of Cell). A paired T-test was performed on the normalized florescence intensity of the cells before and after mechanical stimulation. Typically, 10 cantilever-cell pairs were recorded for each experimental condition.

Parallel plate flow chamber assay: The assay was conducted using a parallel plate flow chamber obtained from GlycoTech (Rockville, Maryland) connected to an Infusion Withdrawal Syringe Pump (Harvard Apparatus, Holliston, MA). Confluent bEnd.3 cells cultured on 35 mm culture dishes were first loaded with DAF-FM and subjected to shear stress at 5 dynes/cm^2. NO production was monitored over time using the IX71 fluorescence microscope.

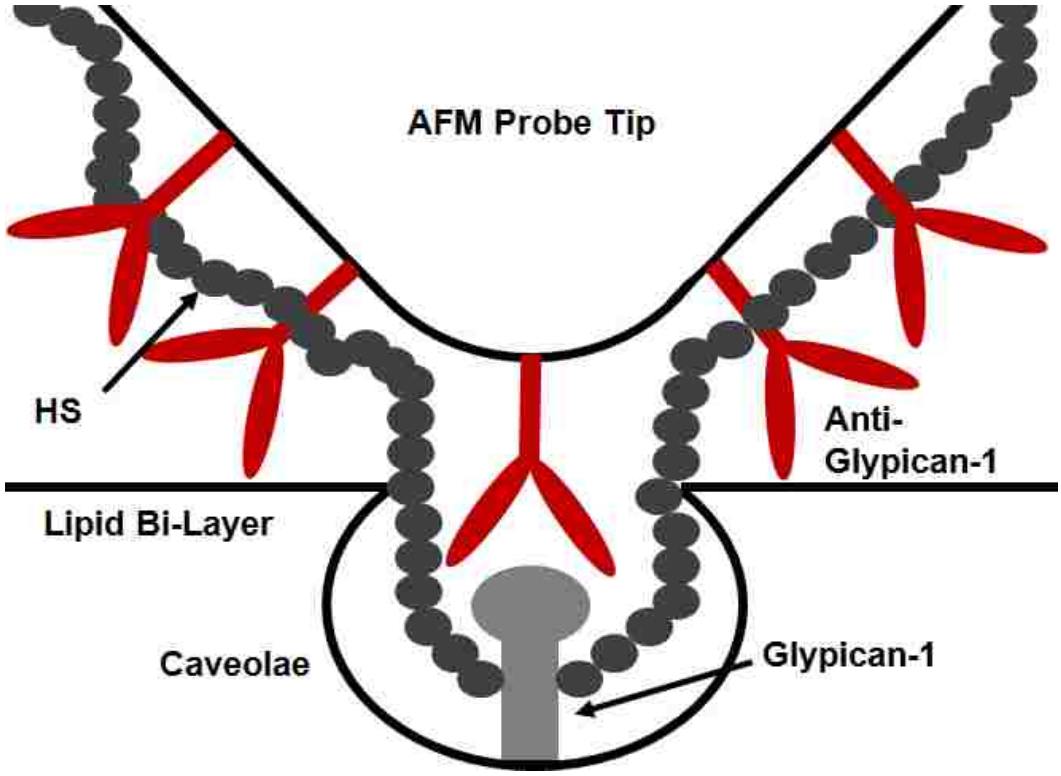

Figure 4.1: Scale rendition of the coated AFM probe approaching glypican-1. The figure demonstrates the relative sizes of the glypican-1 IgG antibodies, ~40 nm (108); the rounding of AFM probe tip, ~20 nm; and the caveolae, ~70 nm in diameter (124).

4.4 Results

When the AFM probe coated with anti-glypican-1 was depressed into the cell and retracted such to produce a force on the glypican-1, an increase of about 35% in DAF-intensity could be seen. An increase of about 11% in DAF-intensity could be observed when the probe was coated with anti-HS (Fig. 4.1C). This seems to suggest that glypican-1 alone is a powerful mechanotransducer as seen in flow experiments (32). Also, it shows that HS alone can induce NO production albeit in a lesser fashion. This may be due to the fact that HS also attaches to syndecans. Therefore, when alone HS is pulled it

may not be in the same region as glypican-1, thus producing a force on the cell but not on glypican-1 resulting in lower NO production.

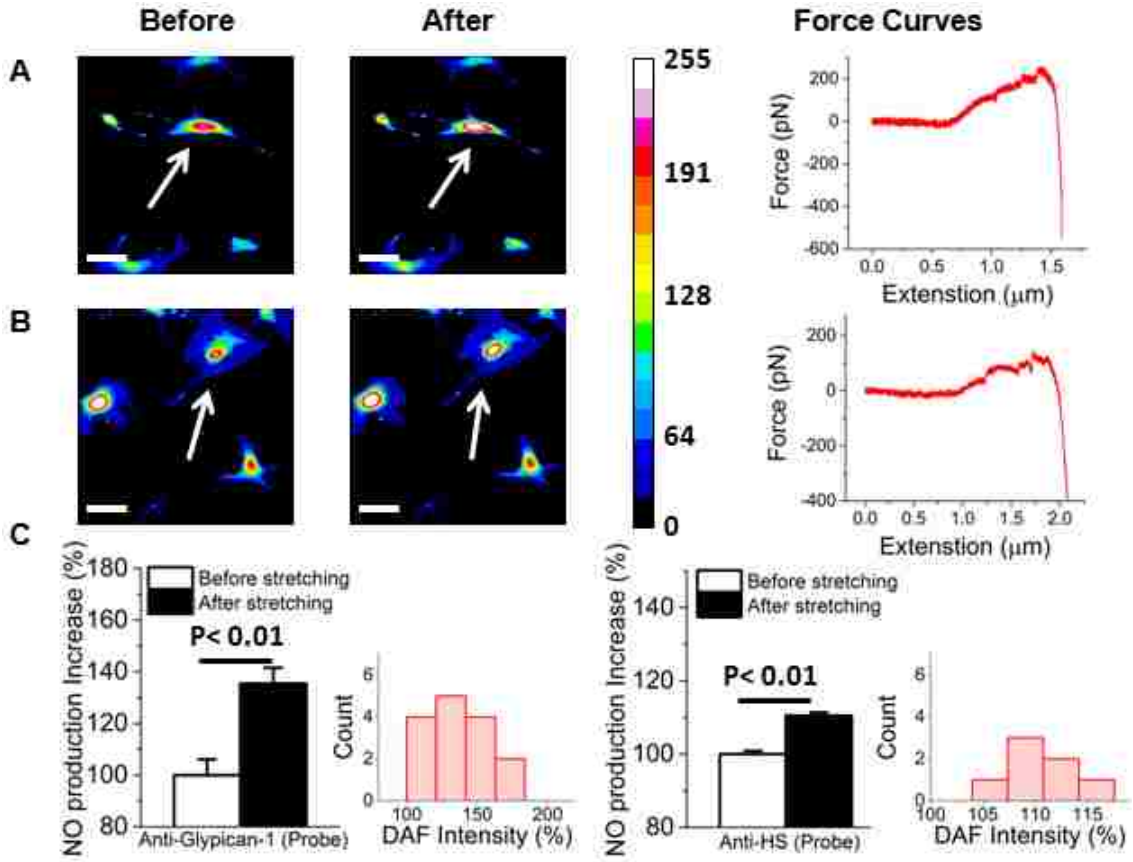

Figure 4.2: Experimental results for probes coated in anti-glypican and anti-HS. (A) Demonstrates the before and after images taken of a single bEnd.3 cell that has undergone mechanical stretching from an AFM probe coated in anti-glypican along with the corresponding force curve that produces this affect. It is clear the neighboring cells do not change. When the AFM probe is coated in anti-HS is can be seen that there is less NO production (B). The data was quantified for a sample of 15 cells stimulated by an anti-glypican coated AFM probe and 10 cells for and anti-HS coated AFM tip (C). The basal level of NO was considered to be 100%. In the bar graphs "Before" is before mechanical stimulation and "After" is after mechanical stimulation. The data was determined as normally distributed with a Shapiro -Wilk of 0.063 and 0.733 for the anti-glypican coated AFM probe and the ant-HS coated probe respectively. Therefore a t-test was performed. The results are placed above the bars in the plot. Scale bar is 20 μm.

Furthermore, to insure that the DAF-intensity was specific to NO, the bEnd.3 cells were exposed to 100µM/L of L-NAME (Sigma-Aldrich, St. Louis, MO), a known inhibitor of eNOS. After the cells were treated with L-NAME the production of NO was greatly reduced, indicating that the observed increase in DAF intensity was specific to NO. We then analyzed the dependency of the NO production on the intake of Ca^{2+}. After the bEnd.3 cells were exposed to 5mM of EDTA (Sigma-Aldrich, St. Louis, MO) the NO production was greatly reduced from non-chelation conditions. Both of these experiments were performed with an AFM probe coated in anti-glypican (Fig. 4.2).

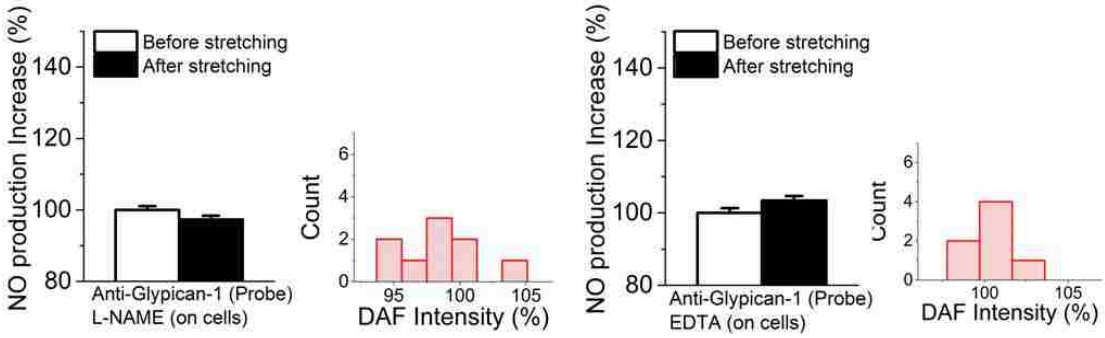

Figure 4.3: eNOS inhibited and Ca^{2+} chelation conditions. Anti-glypican coated AFM probes were used to simulate 10 cells treated with L-NAME and 10 cells treated with EDTA. The basal level of NO was considered to be 100%. In the bar graphs "Before" is before mechanical stimulation and "After" is after mechanical stimulation. The data for the L-NAME conditions was determined as normally distributed with a Shapiro -Wilk of 0.675 where the data for the cells treated with EDTA was not, having a Shapiro –Wilk of 0.007. Therefore a t-test was performed for the L-NAME treated cells and a K–S test for the EDTA treated cells. No significance was found for either experiment.

After the dependence of NO production on Ca^{2+} was confirmed we sought to analyze the affects that TRP channels may have on the production NO. The probes were first coated in glypican-1 and the experiment was repeated after the cells were exposed to 100 µM of Amiloride or SKF96365, blockers of TRPP2 and TRPC1 channels

respectively. When the bEnd.3 cells were treated with Amiloride a reduction in NO production could be observed after mechanical stimulation by the AFM. However, the amount of production post mechanical stimulation was still statistically significant over the basal levels observed in cells. When bEnd.3 cells were exposed to SK96365 NO production was completely inhibited (Fig. 4.3C). This data implies that TRPC1 channels play the dominant role in allowing Ca^{2+} into the cell to begin the NO production cascade. Since glypican-1 was the protein that was being pulled the TRPC 1channels and to some extent TRPP2 channels seem to be gated by mechanical perturbations on this protein.

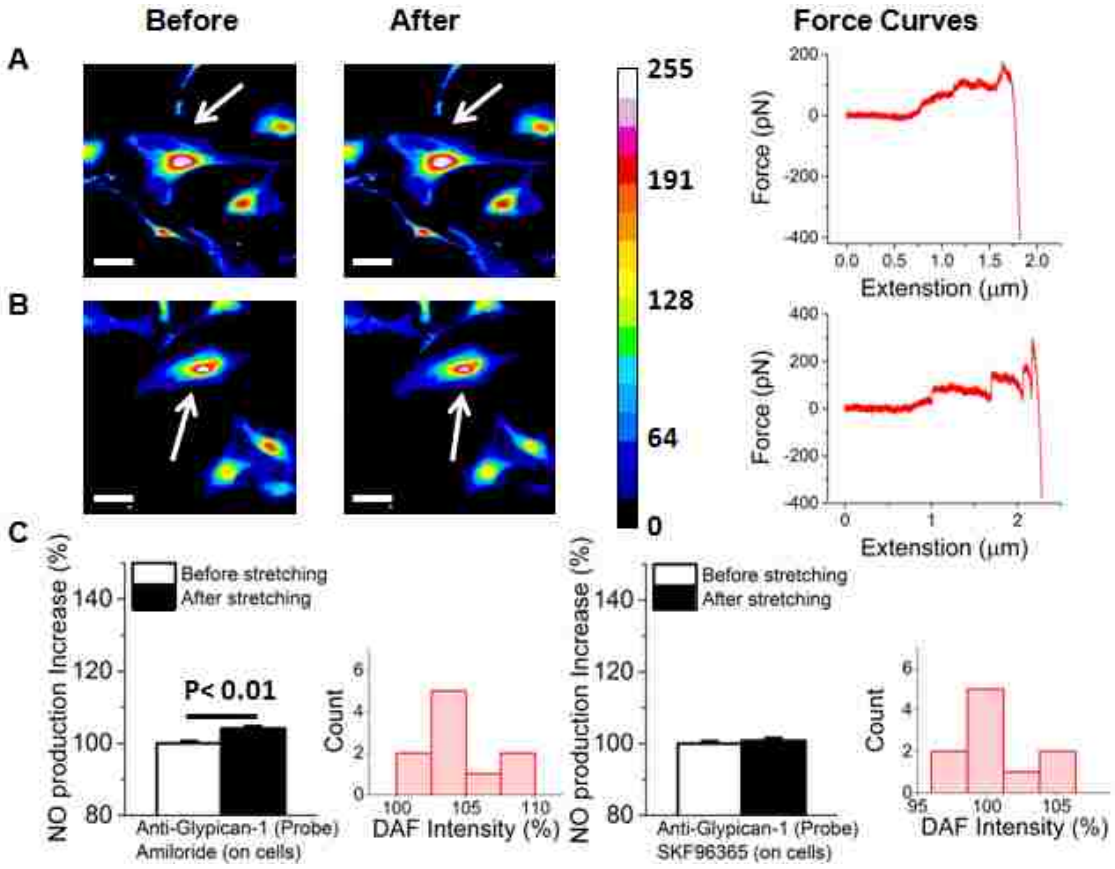

Figure 4.4: TRPP2 and TRPC1 inhibited conditions. It can be clearly observed that when cells are exposed to amiloride or SKF96365 that there is little to no increase in NO production. The data was quantified for a sample of 10 cells stimulated by an anti-glypican coated AFM probe under amiloride treated conditions and 10 cells stimulated by an anti-glypican coated AFM tip probe under SKF96365 treated conditions. Again the corresponding forces curves are provided (A and B). The basal level of NO was considered to be 100%. In the bar graphs "Before" is before mechanical stimulation and "After" is after mechanical stimulation (C). The data for the amiloride conditions was determined as normally distributed with a Shapiro -Wilk of 0.240 where the data for the cells treated with SKF96365 was not, having a Shapiro –Wilk of 0.031. Therefore a t-test was performed for the amiloride treated cells and a K–S test for the SKF96365 treated cells. Significance was found for the amiloride treated cells with the P value provided in the plot. No significance was found for the SKF96365 treated cells. Scale bar is 20 μm.

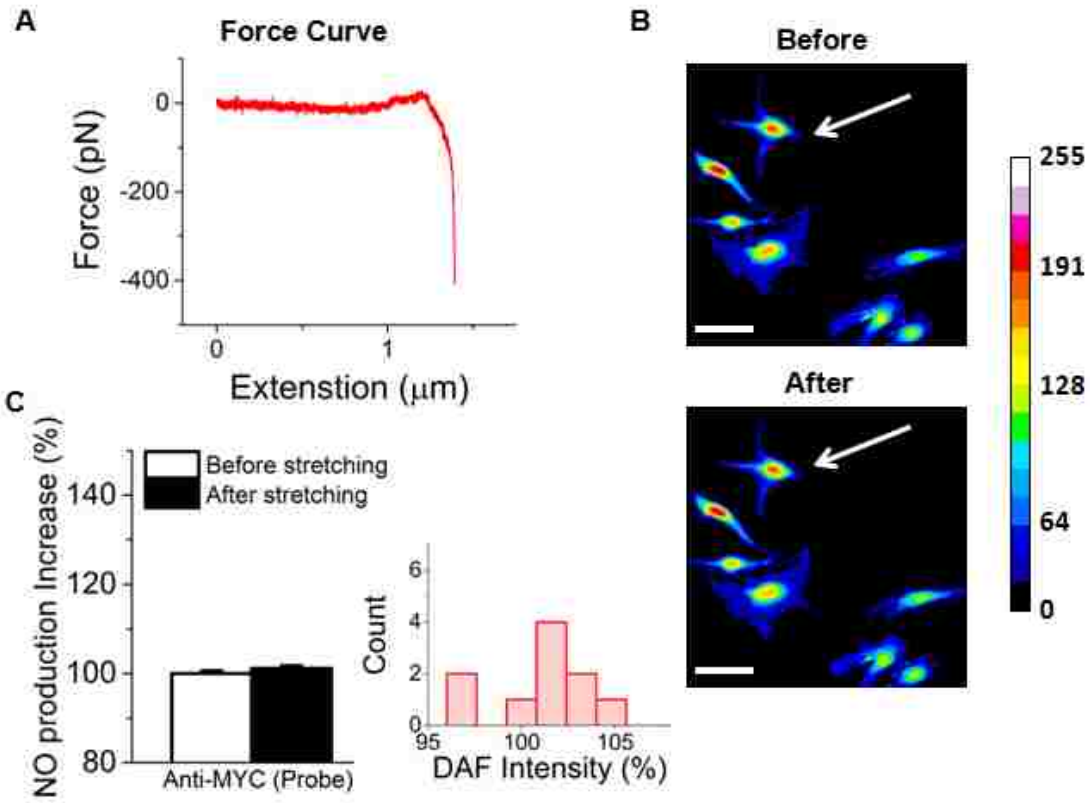

Figure 4.5: MYC Tag coated probe results. When the AFM probe was coated in anti-MYC it was unable to produce a force on the cell. Therefore no production of NO could be seen (A and B). The basal level of NO was considered to be 100%. In the bar graphs "Before" is before mechanical stimulation and "After" is after mechanical stimulation (C). The data for these conditions was determined as normally distributed with a Shapiro -Wilk of 0.160. Therefore, a t-test was performed. No significance was found. Scale bar is 20 μm.

The amount of force and work placed on each cell was quantified by analyzing the curve produced by the AFM. There was no significance between the average amount of force or work applied to the cells across all experiments, with the exception of the experiment utilizing the anti-MYC coated probes (Fig. 4.5). The statistics were analyzed a Kruskal-Wallis H test done in IBM SPSS (SPSS, Inc., Chicago, IL). This was repeated to determine the significance of the NO production between groups.

Furthermore, there was little correlation between force and work and the amount of NO produced at these scales (Fig. 4.6).

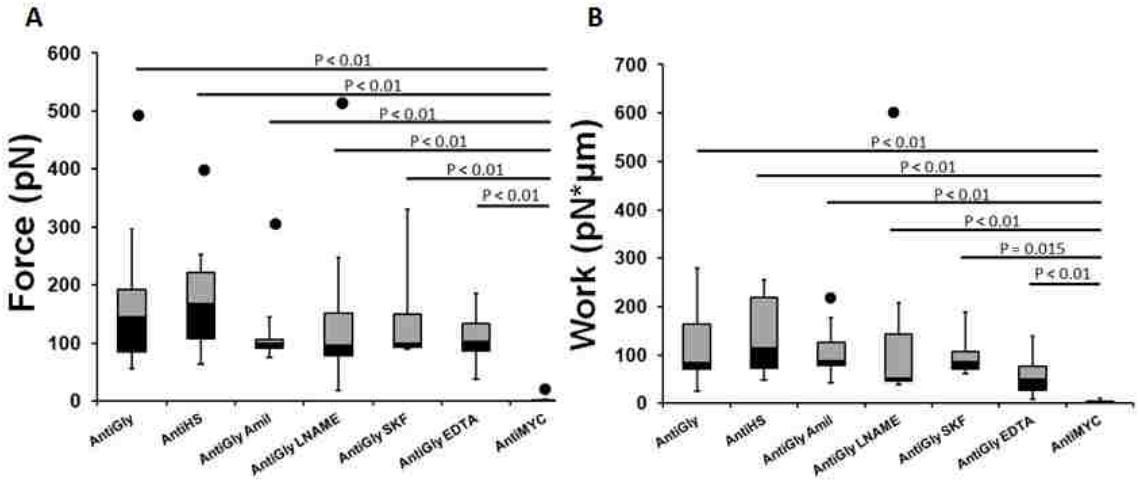

Figure 4.6: Force and Work placed on the cells. To insure that the NO production we were observing was due to the stimulation of glypican-1 and not the amount of force or energy imparted on the cells all of the scans were quantified for peak force (A) and work (B). A Kruskal-Wallis H test was performed to determine if there were significant differences between the groups as not all of the data was normally distributed. Median forces were statistically different for force, $H(6) = 28.86$ with a $p < 0.001$ and work, $H(6) = 31.37$ with a $p < 0.001$. All of the significant P values are included in the plot. Clearly the force and work applied to the cell were the same across all conditions with the exception of the anti MYC coated only AFM probe, as expected.

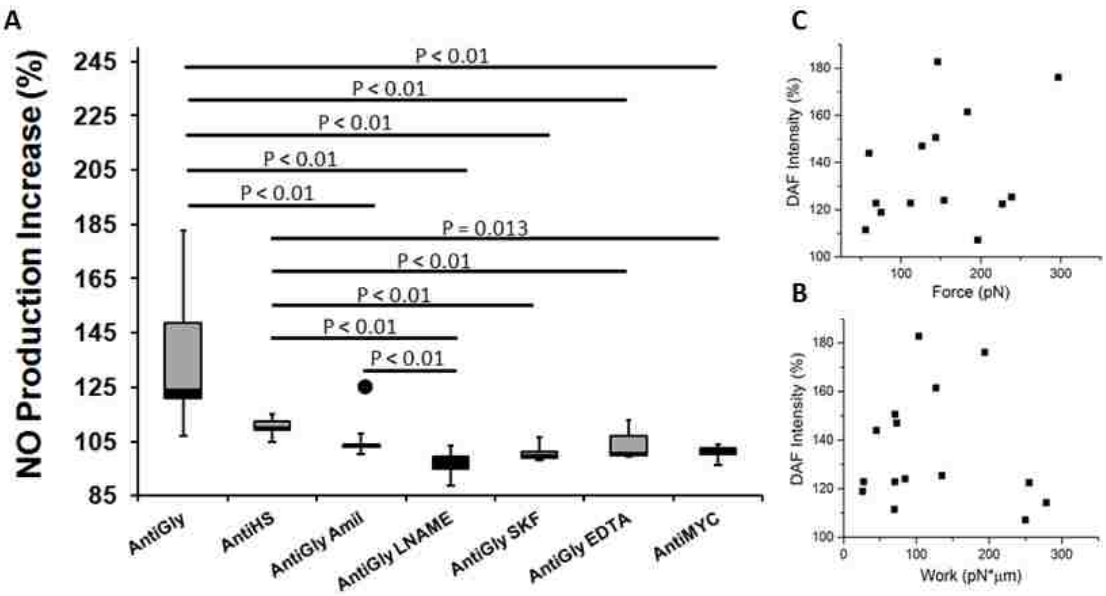

Figure 4.7: NO production comparison. Kruskal-Wallis H test was performed to determine if there were significant differences in force between the groups. Median forces were statistically different. $H(7) = 84.27$ with a $p < 0.001$. (A). All of the significant P values are included in the plot. From this data it can be shown that AFM probes coated with anti-glypican and anti-HS (with no other treatment given to the cells) cause the cells to produce more NO than any other conditions tested. Also, there seems to be only a weak correlation between force, work and NO produced by the cells at these scales of force and work (B and C).

Further care was taken to insure that AFM probes did indeed express the antibodies that were coated on them. To achieve this we followed the above protocol developed by Dr. Hermann J. Gruber, Johannes Kepler University (http://www.jku.at/biophysics/content), with our own modification. Since our anti-glypican contained 0.1% gelatin we applied protein A (Thermo Fisher Scientific Inc) to the probe after the PEG was applied. This allowed us to bypass the non-specific binding that the gelatin has to PEG, thus permitting us to bind more antibody to the probe. To verify the validity of this we incubated the AFM probe in Alexa Fluor 546 anti-rabbit

(Thermo Fisher Scientific Inc., Waltham, MA, USA) for 1 hr. at room temperature after the final step where the glypican antibodies are adhered to the AFM probe. A control was performed using the MYC tag in the place of the anti-glypican, which should not attach to the secondary antibodies. This insured that we were seeing fluorescence that is specific to the desired antibody (Fig. 4.7A and B). We also performed this same task for the anti-HS probe. We followed the normal un-modified protocol developed by Dr. Hermann J. Gruber, Johannes Kepler University (http://www.jku.at/biophysics/content), adding Alexa Fluor 546 anti mouse (Thermo Fisher Scientific Inc., Waltham, MA) for 1 hr. at room temperature after the final step where the HS antibodies were attached to the probe. A control was done by simply adding the secondary antibody to the probe with no anti-HS (Fig. 4.7C and D).

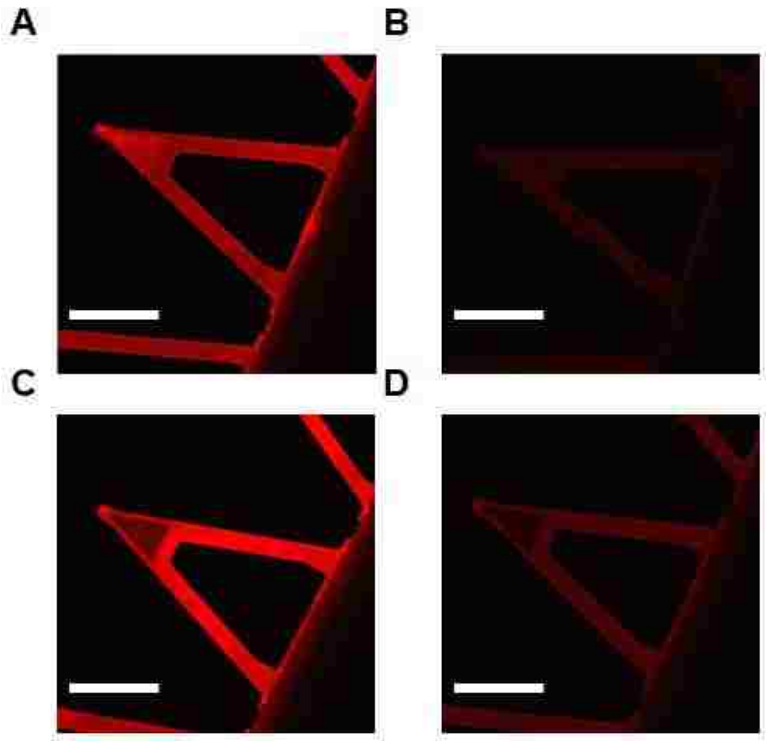

Figure 4.8: Cantilever staining verification of protein coating. To prove the validity of our modified protein coupling method (originally developed by Dr. Hermann J. Gruber, Johannes Kepler University) we incubated the anti-glypican AFM probe (A) in Alexa Fluor 546 anti-rabbit secondary antibody. The control (B) was coated using the MYC before introduction of the secondary. We also validated the presence of the anti-HS on the AFM probe by incubating it in Alexa Fluor 546 anti-mouse secondary antibody (C). The control was done by simply incubating an AFM probe in the secondary with no anti-HS (D). Scale bar is 40 µm.

4.5 Discussion

Endothelial cells are continuously exposed to shear stresses due to blood flow within the human body. This stress will be imparted on the ESG and is assumed to begin the mechanotransduction process that leads to NO production in endothelial cells. Furthermore, there is a significant vertical lifting of the ESG core proteins though the lipid bilayer when the shear stress is applied (20). As this affect is what may allow the

AFM to beginning the NO signaling cascade similar to what has been seen in flow experiments (35, 84), we performed a flow assay to verify if treatment of the bEnd.3 cells with SKF96365 or Amiloride would inhibit NO production. The assay was conducted using a parallel plate flow chamber obtained from GlycoTech (Rockville, Maryland) connected to an Infusion Withdrawal Syringe Pump (Harvard Apparatus, Holliston, MA). Confluent bEnd.3 cells cultured on 35 mm culture dishes were first loaded with DAF-FM and subjected to shear stress at 5 dynes/cm^2. NO production was monitored using the IX71 fluorescence microscope. Images were taken in 5 min intervals for a total of 30 min. These results clearly demonstrate that SKF96365 inhibition of TRPC1 or Amiloride inhibition of TRPP2 will cause a marked reduction in NO production when bEnd.3 cells are exposed to physiological shear stresses due to fluid flow.

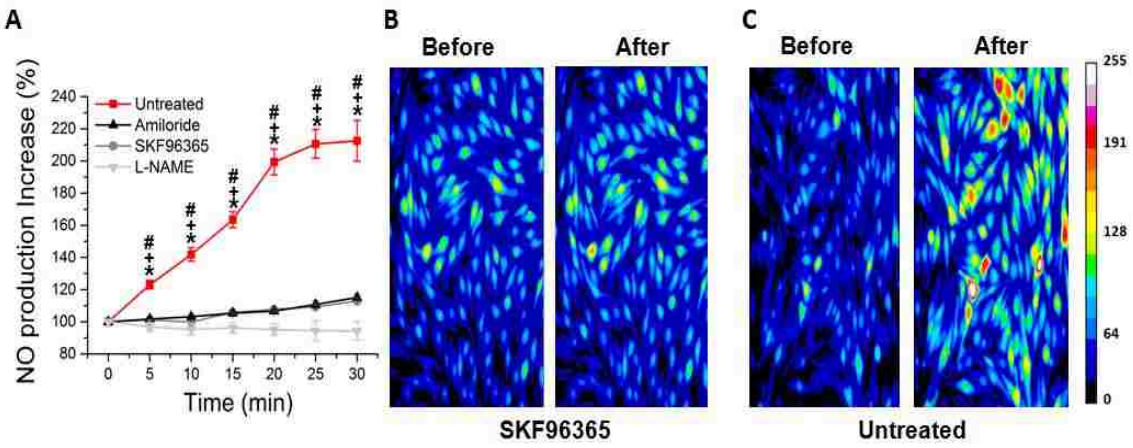

Figure 4.9: BEnd.3 cells exposed to shear flow. In order to compare the results of the AFM study to a more physiological scenario the bEnd.3 cells were exposed to a shear stress of 5 dynes/cm^2. Images were taken every 5 min for a total of 30 min and the DAF fluorescence of each image was quantified in imageJ (A). The DAF fluorescence at the start, i.e. the first image was considered to be 100%. It can clearly be seen that after even 30 min of applying shear stress to the cells that were exposed to SKF96365 very little NO production can be seen when compared to the untreated cells (B and C). A similar affect can be seen vi amiloride exposure. L-NAME was utilized as a control to demonstrate NO specificity. To test for significant differences in the data sets, first a Shapiro-Wilk test was utilized to determine normality. The normality criterion was met for all groups. Therefore, a Tukey test was performed on the data via an ANOVA to determine the p values. *P<0.05 between Amiloride and Untreated, +P<0.05 between SKF96365 and Untreated, #P<0.05 between L-NAME and Untreated.

Another important fact about our data is that the cells tend to produce the majority of the NO in the center of the cell both when stimulated by AFM or by flow. This was expected by AFM, as this is the region of the cell that was being mechanically pulled due to the fact that the anti-glypican achieves interaction with the cell in this region. However, the flow data seems to mirror this affect. Therefore a staining study was done such to image the region in which the proposed mechano-sensing glypican-1 is located as well as its proximity to TRPC1 and TRPP2 channels to glypican-1.

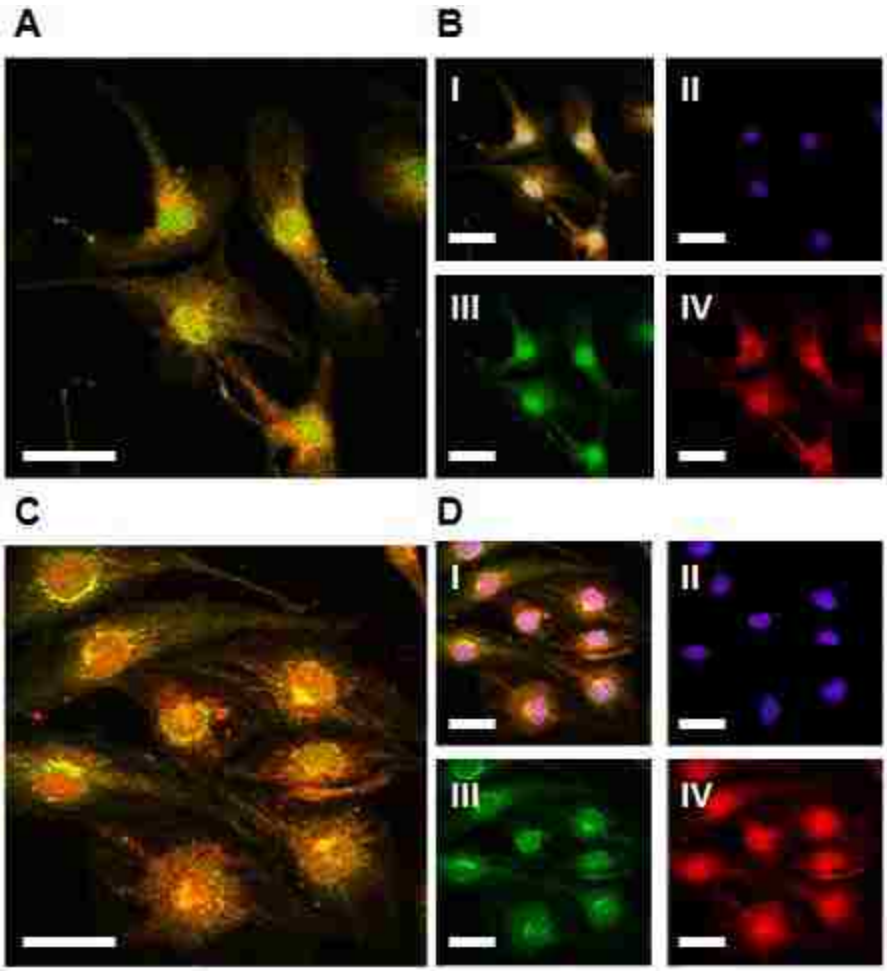

Figure 4.10: BEnd.3 cell fixed and stained for Glypican-1, TRPC and TRPP. To analyze the regions in which the glypican-1 and TRPC1 and TRPP2 are located multi colored co-localization staining was performed. When glypican-1 and TRPP2 were stained for it can be seen that there is substantial overlap particularly in the nuclear region of the cell (A). The nucleus location is shown relative to the glypican-1 and TRPP2 as well as individually (B-I and II). Further images of the glypican-1 only (B-III) and TRPP2 only (B-IV) are shown as well. When glypican-1 and TRPC1 were stained the overlap occurs mainly in patches that are adjacent to the nucleus (C). Again, the nucleus location is shown relative to the glypican-1 and TRPC1 as well as individually (D-I and II). Note that in the images of the glypican-1 only (D-III) and TRPC1 only (D-IV) indicate that the patches seem to be of the TRPC1 clustering independent of glypican-1. Scale bars are 20 µm.

To achieve the cell images the bEnd.3 cells were first fixed in 4% w/v Para-formaldehyde (Sigma-Aldrich, St. Louis, MO) dissolved in PBS for 10 min. They were then washed 3x for five minutes in PBS. Following this the cells were perforated using 0.5%

Triton X-100 (Sigma-Aldrich, St. Louis, MO) diluted in PBS for 10 min. Again the cells were washed 3x for five minutes in PBS following this step. The glypican-1, TRPC1 and TRPP2 primary antibodies were diluted 1:100 in PBS from the stock concentration and added the cells for 24 hr. at 4 ^{o}C. The primary antibodies were then removed and the cells were washed 3x in PBS. To visualize the glypican-1, Alexa Fluor 546 anti-rabbit was added to the cells for 1 hr. at room temperature. To visualize the TRPC1 or TRPP2 Alexa Fluor 488 anti-mouse was added to the cells for 1 hr. at room temperature after the Alexa Fluor 546 anti-rabbit was removed. Images were taken the same day as the treatment with the secondary antibodies.

This assay investigated the role of the ESG in NO production by isolating the key components of the ESG that are thought to be involved in NO production. It has been shown that ECs with RNA-silenced glypican-1 will have inhibited NO production under physiological flow conditions (31). Furthermore, it has been shown that TRPC1 and/or TRPP2 are needed to produce NO under mechanical stress (11) and that TRP channels are known to allow Ca^{2+} into the cell and cause vasorelaxation in ECs (11, 38). Moreover, TRPC1, TRPP2 and glypican-1 are all located within the caveolae (2, 26, 39). This is also the location of eNOS (34), which produces NO after Ca^{2+} intake (16, 96) . Therefore, it would follow that the mechanical activating mechanisms would share a common location. We focused on uncovering the underlying mechanism that these observations are dependent on. It appears that glypican-1 causes the production of NO as follows: Glypican-1 is physically attached to HS, a known mechano-sensor required for NO signaling (35). Therefore, under mechanical perturbations, the HS-glypican-1

complex will cause tension in the caveolae. This tension will activate nearby TRP channels located within the caveolae via attachment to CAV-1. These channels are likely TRPC1 (2) or TRPP2, which form hetero-multimeric channels with TRPC channels (2, 26). Furthermore, from the images co-localization of glypican-1 and TRPC1 and TRPP2 can clearly be seen, particularly in the nuclear region of the cells. Referring to Fig. 4.1A and B as well as Fig. 4.8C it is clear that most of the NO is produced in this region.

The power of bio-mechanical engineering research comes from the ability to witness events such as NO production in live cells as they happen. This experiment embodies this idea; not only can we witness live NO production, but we can witness the how live NO productions is affected by individual constituents of the ESG. We believe that we can at last provide a comprehensive bio-mechanical model for how ECs respond to blood flow with NO production by utilizing this powerful technique. This information can have potentially therapeutic applications (68, 92, 96, 136, 143).

Chapter 5: Dual Regulation of L-Selectin Mediated Leukocyte Adhesion by Endothelial Surface Glycocalyx

5.1 Abstract

This study analyzed the endothelial surface glycocalyx (ESG)-dependent adhesion between leukocytes (K562s) and human umbilical cord vein endothelial cells (HUVECs). We directly quantified the detachment force and work perpendicular to the cell membrane. The study aimed to clarify the role of the ESG in the adhesion between leukocytes and resting HUVECs as well as HUVECs under inflammatory conditions. An AFM-based single-cell adhesion assay was conducted. Detachment force and work were measured for every cell-cell separation event. The experiment was performed under removal of the ESG's major GAG components HS and HA. The HUVECs, were activated by inflammatory cytokine tumor necrosis factor alpha (TNF-α). For the resting HUVECs, when HS and/or HA were removed, the detachment force and work in the normal direction were increased dramatically. For the HUVECs activated with TNF-α, we observed an increase in detachment force and work compared to the resting HUVECs and removal of HS and/or HA resulted in a significant decrease of detachment force and work. The results demonstrate that the ESG layer serves a dual function: (1) on resting endothelium, it prevents leukocyte adhesion, and (2) under inflammatory conditions, it participates in endothelial-leukocyte interactions with molecules such as selectins

5.2 Introduction

This study analyzed, via AFM, the separation forces that exist in cell-cell interactions between leukocytes and the endothelial wall on a short time scale of 0.5 seconds such to imitate the first tethering and rolling stage of leukocyte adhesion. The forces that this study showed are in the vertical direction, thus giving insight into the normal forces involved in leukocyte rolling; the force component that holds the leukocytes to the endothelium under flow conditions. The first aim of this study demonstrated an increase of adhesive force due to the removal of HS and HA by heparinase I&III and hyaluronidase respectively. This was done to demonstrate the affects that the thickness and density of the gel-like ESG structure had on leukocyte-endothelial adhesion forces. The second aim of this study exhibited the manner in which endothelium stimulation by the inflammatory factor TNF-α increased leukocyte-endothelial adhesion forces through heparin mediated ligands. This revealed that leukocyte adhesion to the endothelial wall, under inflammatory conditions, is both large and heavily reduced under heparinase I&III treatment.

5.3 Additional Background

TNF-α is an inflammatory cytokine produced by macrophages and monocytes during acute inflammation and is responsible for a varying range of signaling events within cells, leading to necrosis or apoptosis (60). Also, the expression of L-, P-selectin molecules is up-regulated via TNF-α (106) and TNF-α has been shown to up-regulate monocyte and leukocyte attachment through L-selectin binding (45, 147). However,

there is evidence that suggests TNF-α stimulated endothelial cells do not express more L-selectin ligands than endothelial cells that are not stimulated by TNF-α (45, 139).

K562s are a leukocyte cell line that can impulsively develop characteristics that are analogues to erythrocytes, granulocytes and monocytes (77). Moreover, K562s are not known to express, among other adhesion molecules, endogenous L-selectin (14). L-selectin, belongs to a group of lectins known as selectins that arbitrate the initial adhesion of leukocytes to the luminal surface of the endothelium in a Ca^{2+} dependent fashion during inflammation (116, 122). L-selectin is typically expressed on leukocytes and interacts with constitutively expressed ligands and inducible ligands on the endothelium (72, 116).

5.4 Materials and Methods

Cell Culture: Human umbilical vein endothelial cells (HUVECs), purchased from ATCC were cultured in Lonza EBM-2 medium from an EGM-2 BulletKit containing 0.5mL hEGF, 0.2mL Hydrocortisone, 0.5mL GA-1000 (Gentamicin, Amphotericin-B), 10mL FBS (Fetal Bovine Serum), 0.5mL VEGF, 2mL hFGF-B, 0.5mL R3-IGF-1, 0.5mL Ascorbic Acid, and 0.5mL Heparin. K562 leukocytes, purchased from Sigma-Aldrich, were cultured in RMPI-1640 medium also from Sigma-Aldrich containing 10% FBS from ATCC, 2% L-glutamine from Gibco by Life Technologies, 1% sodium bicarbonate from Sigma-Aldrich, 1% from sodium pyruvate from Sigma-Aldrich and 1% penicillin-streptomycin from Sigma-Aldrich. All cells were cultured in Corning t-25 flasks and plated in experiments in 35 mm Cyto-One treated culture dishes for AFM experiments or World Precision Instruments 35mm

FluoroDish glass bottom culture dishes for cell staining. The culture was maintained at 37 ^{o}C and 5% CO_2 in a water jacked incubator.

Enzymes: Heparinase I&III blend from flavobacterium heparinum from Sigma-Aldrich was made into aliquots in PBS at 50UN/mL and stored at -80 ^{o}C.

Hyaluronidase from bovine testes, Type I-S, lyophilized powder, 400-1000 units/mg, from Sigma-Aldrich, was stored at -20 ^{o}C and prepared fresh in PBS with .01% BSA at 2000U/mL before every experiment.

Cytokines: TNF-α, from R&D systems, was prepared at a concentration of 100 µg/mL in PBS with 0.1% BSA and stored in a single 100µL aliquot at -20 ^{o}C.

Anti-Bodies: DREG.200, from ATCC, purified from hybridoma, was purchased at a concentration of 200 µg/mL in PBS and stored in aliquots of 100µL at 4 ^{o}C. Anti-MYC, from invitrogen, was purchased at a concentration of 1.5 mg/mL in a single 50 µL aliquot at that was stored at 4 ^{o}C. Alexa Fluor 546 goat anti-mouse secondary anti-body, from ThermoFisher, was purchased at a concentration of 2 mg/mL in a single 500 µL aliquot that was stored at 4 ^{o}C and was a TRITC conjugate.

Amino Acids: Poly-L-lysine, from Sigma-Aldrich, was prepared at a concentration of 50 µg/mL in 0.2 M $NaHCO_3$ and stored in aliquots of 1mL at -20 ^{o}C.

Collagen: Collagen type I solution from rat tail, from Sigma-Aldrich, was purchased at a concentration of 4 mg/mL and stored in a single bottle at 4 ^{o}C.

Cell Dyes: Wheat germ agglutinin (WGA) as lyophilized ≥ 55% (GE) powder, from Sigma-Aldrich, was prepared at a concentration of 1 mg/mL in PBS and stored in 20 µL aliquots at -20 ^{o}C and was an FITC conjugate. Hoechst 33258 pentahydrate (bis-benzimide), from

ThermoFisher, was purchased as a powder and stored in 200 µL aliquots at a concentration of 10mg/mL at 4 ^{o}C.

AFM Probes: The AFM probes used in this experiment were Bruker model MLCT-O10 tipless nitride levers and were coated in poly-L-lysine.

Atomic force microscopy (AFM) instrumentation: An AFM, in this experimental context, was used to first pick up the K562 cell and then press the cell against the HUVEC. The AFM used in all experiments was a custom built machine that was programmed using IGOR. The AFM was attached to a CCD camera with 20x objective capabilities, suspended from the ceiling via elastic cables and housed in a noise damping container. The spatial resolution of the AFM in the x-direction is approximately 1 nm and spatial resolution in the y-direction is approximately 15-20 pN.

Cell adhesion assay: To begin the experiment the AFM probes were first coated in PLL. This was done via a high pH buffer technique. First, the AFM probes were placed in acetone for 10 min, and then they were sterilized in a UV ozone chamber for 20 min. After removal from the chamber they were placed into a 0.2 M solution of $NaHCO_3$ in DI water (pH 9.0) containing a 50 µg/mL concentration of PLL. The probes were left to incubate in this solution over night at 4 ^{o}C.

The HUVECs and the K562s were split 3 days a week at ratios of 1:5 and 1:10 respectively. The HUVECs were seeded to the culture dishes coated with collagen 24 hrs before the experiment began at 15% confluence. This was done to insure that single HUVECs would be present and to ensure that the K562s that were being picked up by the AFM were not in contact with any HUVECs prior to the experiment. The collagen

was coated on the surface of the culture dishes by dropping 100 µL of .2 mg/mL collagen, diluted from the stock solution in sterile water, onto the center of the culture dish. The collagen was spread out on the dish by placing a 22x22-1 glass cover slip on top of the drop located in the culture dish.

The AFM calibration, performed the following morning, was done first by pressing the probe against the surface of a Cyto-One culture dish to determine the inverse optical lever sensitivity (InvOLS). The InvOLS was defined as a measure of the sensitivity that the photodetector had to the motion of the laser as it reflected off of the deflecting probe. This value was determined by the slope of the contact portion of the trace produced by the AFM as the probe touched the surface of the dish. Next, the random thermal fluctuations of the AFM probe were recorded as a function of time. This information was then transformed into the frequency domain by the methods of Fourier and yielded the resonance frequency peak of the probe. K_bT divided by the square of the area under this peak was established as the spring constant. With the InvOLS in m/V and the spring constant in N/m, a change in voltage at the photodetector could now be converted into a force at the probe. The PLL coating caused some adhesion between the probe and the surface of the dish however; there was no deviation from expected InvOLS and spring constant values. PBS was utilized as the fluid in which the calibration took place.

For HUVEC activation experiments the HUVECs were stimulated with TNF-α for 10 hrs at 37 ^{o}C at a concentration of 100 ng/mL. If the cells were stimulated with TNF-α, the procedure was done prior to heparinase I&III treatment and/or hyaluronidase

treatment. There was no washing procedure done in between treatments. The heparinase I&III treatment and/or hyaluronidase treatment were performed immediately before the experiment and were done at concentrations of 25 mUN/mL and 20 μg/mL respectively.

First, the cells were treated with the proper concentrations of heparinase I&III and/or hyaluronidase and placed in the incubator for 1 hr. After removal from the incubator, the cells were washed 3x with the culture medium, to remove any remaining enzymes, cytokine and cleaved ESG constituents. Directly after this step the K562 cells were added to the same dish as the HUVECs. The K562 cells were spun down and re-suspended in EBM-2, and then added to the HUVECS by means of a pipette. The K562s were not activated by TNF-α as this mat cause L-selecting shedding (61). The samples were then allowed to sit at room temperature for 15 min, under the AFM, before the experiment began such that that the AFM probe would reach thermo-equilibrium with its surrounding fluid and also so that the leukocytes would have time to settle on the bottom of the dish.

To perform the experiment, a live K562 cell was first attached to the end of the AFM probe by lowering the probe down and touching it to the cell which sat un-adhered to the surface of the culture dish. Since the K562 cells possess a net negative charge and the cantilever a net positive charge, due to the PLL, the cells were easily picked up from the bottom of the dish; the force used to capture the leukocyte was 1 nN with 5 s of dwell time. Immediately after capture, the adhered K562 cell was brought over top of a HUVEC, away from the nucleus, and the force scanning began.

The two cells were touched together with a force of about 300 pN with a dwell time of 0.5 seconds resulting in a contact area of about 17.35 μm^2 that was calculated from a standard contact mechanics model for elastic spheres (152). For these equations: a is the contact area radius which was calculated to be 2.35 μm (Eq. 5.1), R is the radius of the K562 taken to be 10μm (57), P is the load of 300pN, E is Young's modulus which was experimentally determined to be 129 Pa, the means of which are included in the appendix, and v is Poisson's ratio taken to be 0.5.

$$a = \left[\frac{3(1-\upsilon^2)RP}{4E}\right]^{1/3} \quad \textbf{Eq. 5.1}$$

Total vertical displacement was determined to be 1μm (Eq. 5.2). The HUVEC stiffness was not found experimentally but is known to be on the order of 10 KPa (69).

$$\delta = 2\left\{\frac{P}{Ka} - \frac{P}{\pi E}\left[\frac{1-\upsilon^2}{\sqrt{a^2+4R^2}} - \frac{2(1+\upsilon)R^2}{(a^2+4R^2)^{3/2}}\right]\right\}, K = \frac{4}{3}\left(\frac{E}{1-\nu^2}\right) \quad \textbf{Eq. 5.2}$$

In all experiments the AFM recorded the force of indentation, the interaction between the two cells and the extension of the probe tip for 30 force scans per cell-cell pair. All of the data was analyzed for peak force and work (Fig. 5.1). Unique cell-cell pairs were

chosen every time i.e. a new HUVEC and a new K562 were selected every time.

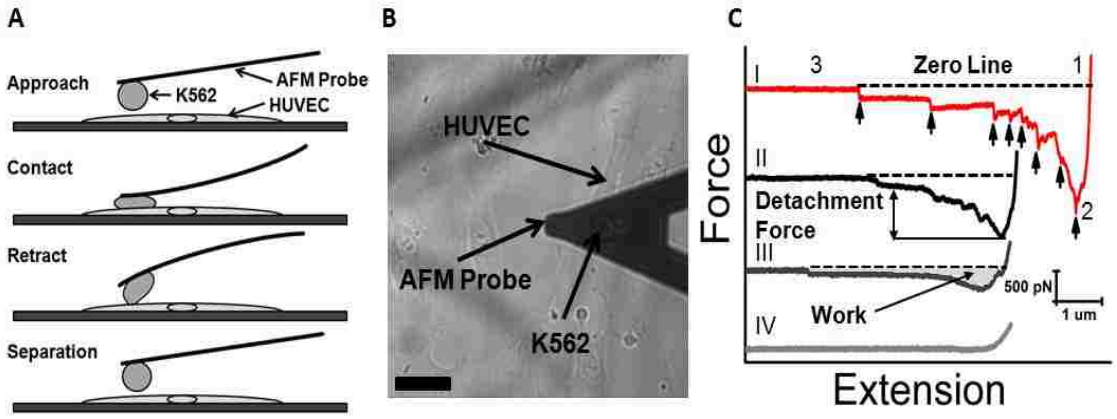

Figure 5.1: Single-cell force spectroscopy of leukocyte-endothelial interaction. (A) A schematic of the experimental procedure. (B) Image of a single leukocyte adhered to the AFM probe over a single HUVEC (scale barf is 20 µm). (C) Typical force spectrum traces for K562 cells bound to HUVES under different conditions. Strong adhesion occurred between K562s and HUVECS treated with TNF-α (I). Adhesion between K562 cells bound to HUVECS after TNF-α by was markedly reduced by hyaluronidase treatment (II). This was again seen under Heparanase I&III treatment (III). The untreated is denoted by the IV trace. Measurements were acquired with a compression force of 300pN, 0.5 s contact, and a cantilever retraction speed of 3 µm/s. Shaded area in the red trace is the "work of deadhesion." Arrows in the black trace point to rupture events; breakage of adhesive bond(s). Dashed lines indicate zero forces.

5.5 Results

The experimental data from the first aim of this study showed an increase of force and work when the HUVECs were exposed to heparinase I &III treatment and/or hyaluronidase treatment over the untreated data, which had no exposure to heparinase I &III or hyaluronidase, (Fig. 5.2). This alludes to the idea that removal of ESG constituents from endothelial cells may expose ligands which interact with the incoming leukocyte. Furthermore, because HS makes up some 50-80% of the total GAGs on the

surface of endothelial cells (59, 103), this affect may be dependent on the amount ESG present, not the type of GAG removed (Fig. 4.2).

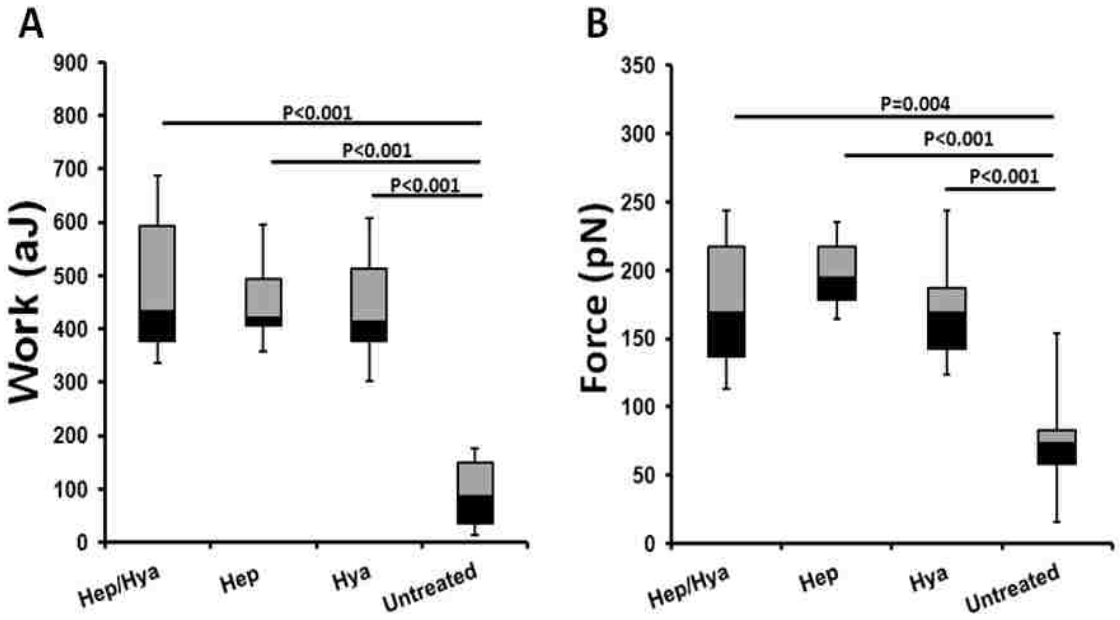

Figure 5.2: ESG mediated adhesion. (A) Work of deadhesion involved in rupturing all bonds between the K562 and the HUVEC. (B) Peak force required to separate the bound K562 from the HUVEC. When the HUVECS were exposed to the heparanase I & II and/or hyaluronidase the work of deadhesion and peak force required for separating the cells increased in a significant fashion. The above p values indicated for (A) and (B) are from comparing the untreated (no treatment on HUVECs) to all three test conditions. N=10 cell-cell pairs for all experiments.

The experimental data from the second aim of this study demonstrated that upon TNF-α stimulation the endothelial-leukocyte interaction was greatly increased over the both the untreated and TNF-α only data, where the TNF-α only data has had no exposure to heparinase I &III or hyaluronidase, but did have exposure to TNF-α. Furthermore, this increase of interaction was almost entirely dependent upon the presence of heparin groups during TNF-α stimulation (Fig. 5.3). Curiously, the same affect, albeit less dramatically, was seen under hyaluronidase treatment of the

endothelial cells. This lends evidence to the idea that HA serves as a powerful ligand for leukocyte-endothelial interactions in the initial stages of cell rolling.

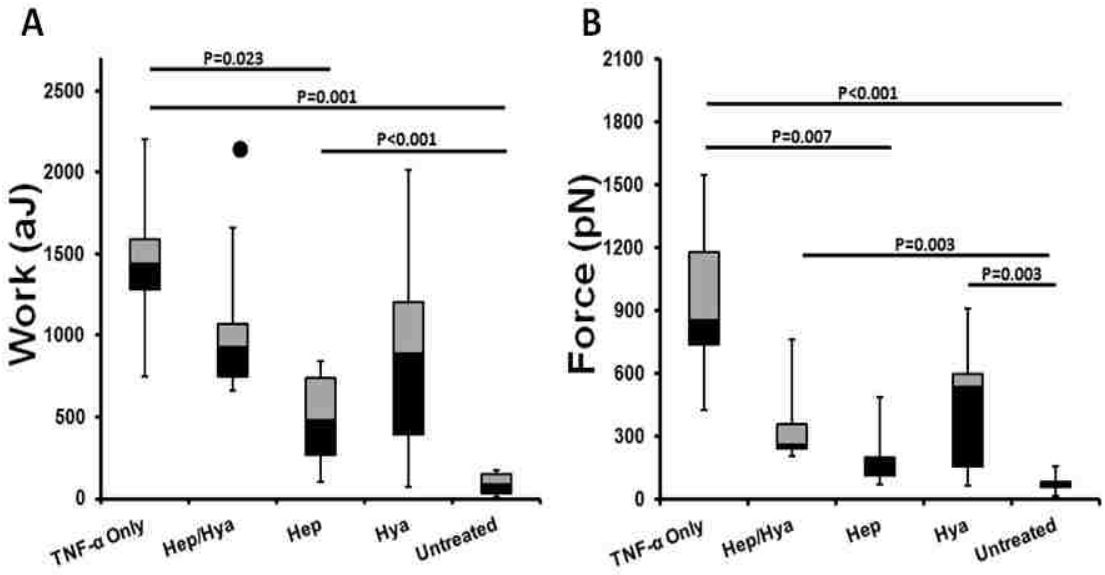

Figure 5.3: ESG mediated TNF-α induced adhesion. (A) Work of deadhesion involved in rupturing all bonds between the K562 and the HUVEC. (B) Peak force required to separate the bound K562 from the HUVEC. Strong adhesion occurred between K562s and HUVECs treated with TNF-α. Adhesion between K562s bound to HUVECs after TNF-α by was distinctly decreased by hyaluronidase treatment. This was again seen more dramatically under heparanase I&III treatment. The untreated has no treatment (HUVECs). The above p values denoted for (A) and (B) are from comparing the TNF-α only to all three test conditions and the untreated, as well as the untreated to all three test conditions. N=10 cell-cell pairs, for all experiments except the Heparanase, Hyaluronidase and Hep/Hya conditions where N=13 cell-cell pairs. Outliers are designated by ●.

5.6 Verification of GAG Removal

To verify the removal of the GAGs from the surface of a WGA staining assay was performed (Fig. 5.4). WGA, which in this case is an FITC conjugate, has the ability to recognize and bind to N-acetylglucosamine (70), a common disaccharide unit within HS and HA (6, 106, 110, 114). To obtain the data HS was first removed from the cell surface by heparinase I &III treatment at a concentration of 25 mUN/mL for 1 hr 30 min at 37 ^{o}C

in the culture medium. The cells were then washed with PBS 2x and treated with 5 μg/mL of WGA for 10 min at 37 ^{o}C in PBS supplemented with 5% BSA. The cells were then washed again 2x in PBS and imaged on a Nikon C2si confocal microscope in PBS with 5% BSA. The images clearly showed a reduction in FITC fluorescence in the HUVECs treated with heparanase I&III. The same procedure was performed for the cells after 20 μg/mL hyaluronidase treatment. Interestingly, only a very small difference in fluorescent intensity could be detected, as shown in Figure 2. This may be due to the fact that HA makes up a much smaller portion of the total GAGs than HS. Since WGA is specific only to N-acetylglucosamine, a disaccharide unit that HS and HA have in common, it is reasonable to believe that the background on the cell surface was too high to detect a significant difference in fluorescence if HA alone is removed.

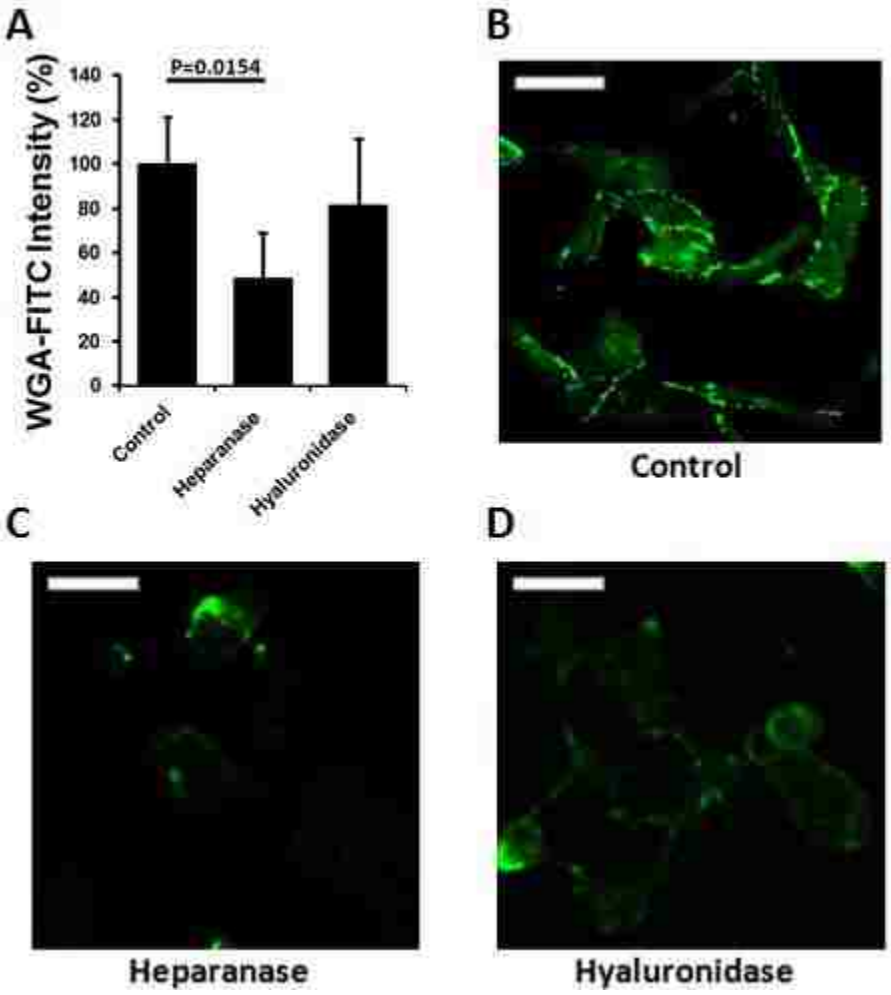

Figure 5.4: Fluorescence images of GAG removal. (A) Plot of the WGA FITC fluorescence post GAG removal. The images show a reduction in FITC fluorescence when compared to the controls (B) in the HUVECs treated with heparanase I&III (C) or hyaluronidase (D). However, only the cells treated with heparanase I&III showed a significant difference in FITC fluorescence as determined by a student's T-tests. The p value is noted in the plot. Scale bar is 20 µm.

5.7 Discussion

The ESG is a negatively charged (39, 104, 148) gel like structure (97, 119, 140) that is predominately made up of HS (59, 103) and can be around 0.5 µm in height (96, 131, 135). Therefore, in the first aim of our study, when the ESG was exposed to 25 mUN/mL of heparinase I&III the thickness, density and charge may have been reduced. This could

allow for rolling molecules that localize on the microvilli of leukocytes (125) to more easily reach through the remaining ESG and bind to other sites on the HUVEC surface. For leukocytes in particular, L-and P- selectin are preferentially expressed on these locations (33, 86, 125). Therefore, if microvilli are able to infiltrate the reduced ESG layer they may bind to leukocyte activators such as leukotriene B4 or platelet-activating factor that are expressed on the luminal surface of endothelial cells (17). This postulation may be further supported by the data gathered from the HUVECs treated with 20 μg/mL of hyaluronidase. This experiment demonstrated a lesser increase in the force required to disassociate the K562 from the HUVEC. This is significant because hyaluronic acid makes up much less of the total GAGs present on the surface of the endothelial cell (39, 104, 106).

The processes of leukocyte adhesion is a complex fourfold progression. The first step involves a tethering due to L-, P- and E-selectins which cause an initial deceleration under flow conditions (17, 45, 106). This affect is believed to permit easier access to cytokines such as TNF-α (106) which trigger firm adhesion via ICAM-1 and VCAM-1 (13, 19, 99, 106, 150). When the HUVECs were stimulated with 100 ng/mL TNF-α for 10 hrs a significant increase in vertical direction disassociation force was seen. Upon treatment with 2 5mUN/mL of heparinase I&III, the force was greatly reduced to similar force levels seen in non TNF-α stimulated cells that had been treated with 25 mUN/mL of heparinase I&III. This indicates that HS and HS proteoglycans may be the dominant ligands for adhesion molecules that provide the vertical force component under TNF-α

stimulated conditions. Furthermore, TNF-α may be an important complex that modifies HS and HA proteoglycans to become powerful ligands.

It is known that L-selectin binding to aortic endothelium can be strongly inhibited heparinase I, II or III (inhibited by 50%), as well as trypsin (inhibited by 90%), which is known to remove all of the cell surface constituents. This indicates that L-selectin binds to HS chains that are attached to HS proteoglycans (45) as well as other sites that are modulated by the contents of the cell surface. Therefore, an additional experiment was conducted to outline a potential mechanism for the generation of TNF-α mediated leukocyte adhesion (Fig. 5.5). L-selectin tethering activity was blocked utilizing the mouse derived IgG1 antibody DREG.200, which is known to block the functional groups of L-selectin (63, 79, 131, 138). The results demonstrate a remarkable decrease in force and work after the leukocytes were exposed to DREG.200 for 15 min following 10 hr of TNF-α stimulation of the HUVECs. A control was conducted with the non L-selectin blocking mouse IgG antibody anti-MYC after 10 hrs of TNF-α stimulation of the HUVECs. The results showed little difference in binding affinity to the TNF-α stimulated TNF-α only. The DREG.200 and anti-MYC treatment took place concurrently with the addition of the K562 cells to the HUVEC dish. The DREG.200 and anti-MYC were combined with the EBM-2 medium at a concentration of 10 μg/mL.

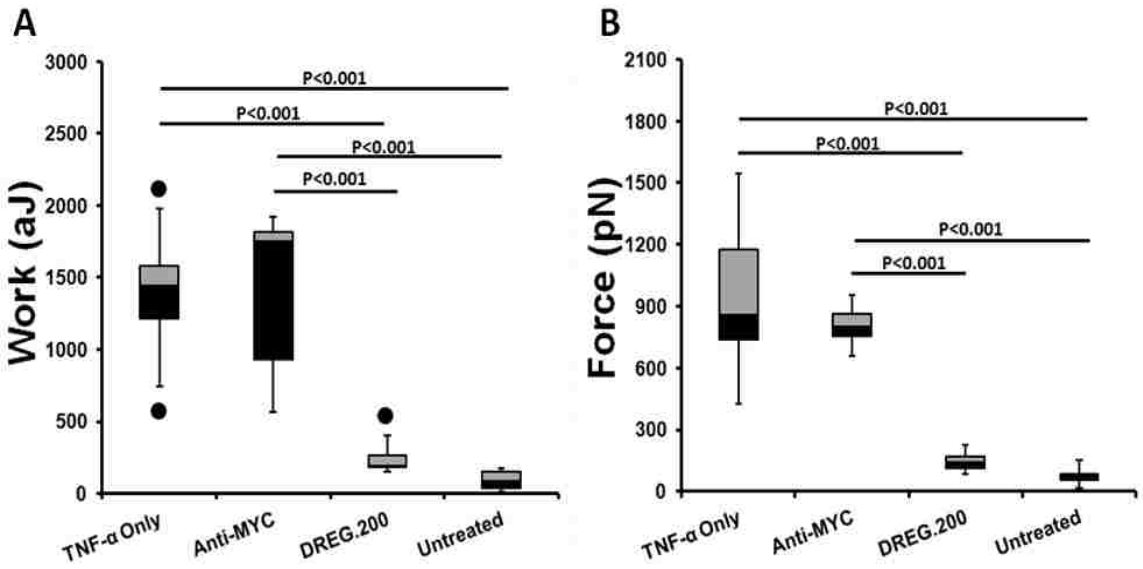

Figure 5.5: L-selectin mediated TNF-α induced adhesion. (A) Work of deadhesion involved in rupturing all bonds between the K562 and the HUVEC. (B) Peak force required to separate the bound K562 from the HUVEC. Strong adhesion occurred between K562s and HUVECs treated with TNF-α. Adhesion between K562s bound to HUVECs after TNF-α exposure was reduced by treatment of the K562s with DREG.200, but not with Anti-MYC. The untreated has no treatment (HUVECs and K562s). The above p values denoted for (A) and (B) are from comparing the + control to both test conditions and the – control. Also, Anti-MYC conditions exhibited significance to the DREG.200 conditions and the –control. N=10 cell-cell pairs for all experiments. Outliers are designated by ●.

The Presence of L-selectin was quantified via antibody staining. To begin a Precision Instruments 35mm FluoroDish glass bottom culture dish was coated with PLL. This was done by diluting the PLL in a 0.2 M solution of $NaHCO_3$ in DI water (pH 9.0) containing a 200 µg/mL concentration of PLL. The dishes were left to incubate in this solution over night at 4 ^{o}C. They were then washed with PBS 3x and the cells were added to the dishes in their culture medium. After 1 hr the culture medium was removed and the cells, now immobilized on the bottom of the dish were fixed with 4% W/V paraformaldehyde for 10 min. They were then washed 2x for 10 min in PBS. Next, DREG.200 was added to the PBS at a concentration of 10 µg/mL and the cells were

allowed to sit overnight at 4 ^{o}C. After this, the cells were treated with the secondary antibody Alexa Fluor 546 goat anti-mouse at a concentration of 10 µg/mL for one hour and the nucleus stain Hoechst 33258 pentahydrate at a concentration of 20 µg/mL for 5min. Finally, the cells were washed 2x in PBS and imaged on a Nikon C2si confocal microscope in PBS. Controls were performed with both 10 µg/mL of Anti-MYC and no primary antibody. The results showed a clear expression of L-selectin on the surface of the K562s used in this experiment which demonstrates that K562 do at the very least express L-selectin functional groups. This is contrary to what is typically known about L-selectin expression on the surface of K562s and may be due to the tendency of these cells to spontaneously change their characteristics to that of erythrocytes, granulocytes and monocytes (77) (Fig 5.6).

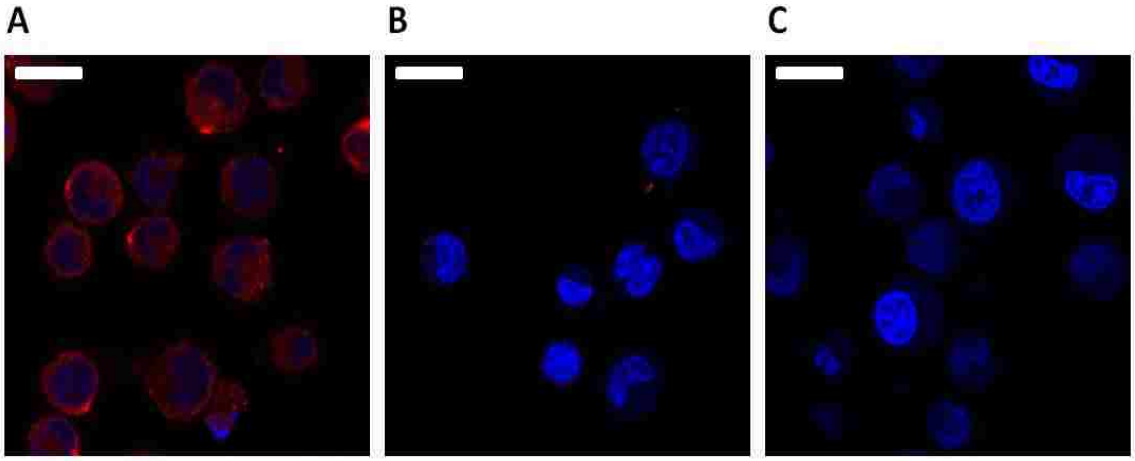

Figure 5.6: DREG.200 interaction staining. Images of the K562s stained for DREG.200. (A) Illustrates the K562s where DREG.200 was applied to the cells 24 hrs before secondary antibody staining with Alexa Fluor 546 goat anti-mouse. It can be seen in the image that there is a high presence of L-selectin shown in red when compared to (B), where the K562s were treated with Anti-MYC 24 hrs before secondary antibody staining. (C) Shows K562s that did not have DREG.200 applied before secondary antibody staining. In all images the nucleus was stained for with Hoechst 33258, shown in blue.

These results illustrate the powerful manner in which L-selectin acts to tether the leukocytes to the surface of the endothelial wall in the vertical direction. Another interesting idea that this data seemed to elucidate was that the work dropped off significantly when the leukocytes were exposed to 10 μg/mL DREG.200. This is perhaps because the cells no longer experienced long tether formations to L-selectin. As this treatment almost completely inhibited K562 binding to HUVECs, it lends support to the idea that L-selectin has a strong binding to HS and HS proteoglycans after exposure to TNF-α. Both of the TNF-α mediated assays findings support previous experimental results from rolling assays (17, 45).

A calcium chelation experiment was also performed on resting HUVECs as well as HUVECs stimulated with TNF-α. The reaction molecule Ca^{2+} was removed from the culture medium via 10 mM EDTA, which is known to remove free Ca^{2+}. The EDTA was added directly to the dish 10 min before the experiment began. Removing Ca^{2+} from the medium caused a reduction in unbinding force and work for both the resting and TNF-α stimulated HUVECs (Fig. 5.7). This information demonstrates two possibilities: one that L-selectin is dependent on Ca^{2+} and therefore L-selectin binding is inhibited, or two,

other long chain molecules such as Lewisx are also in part responsible for the interaction

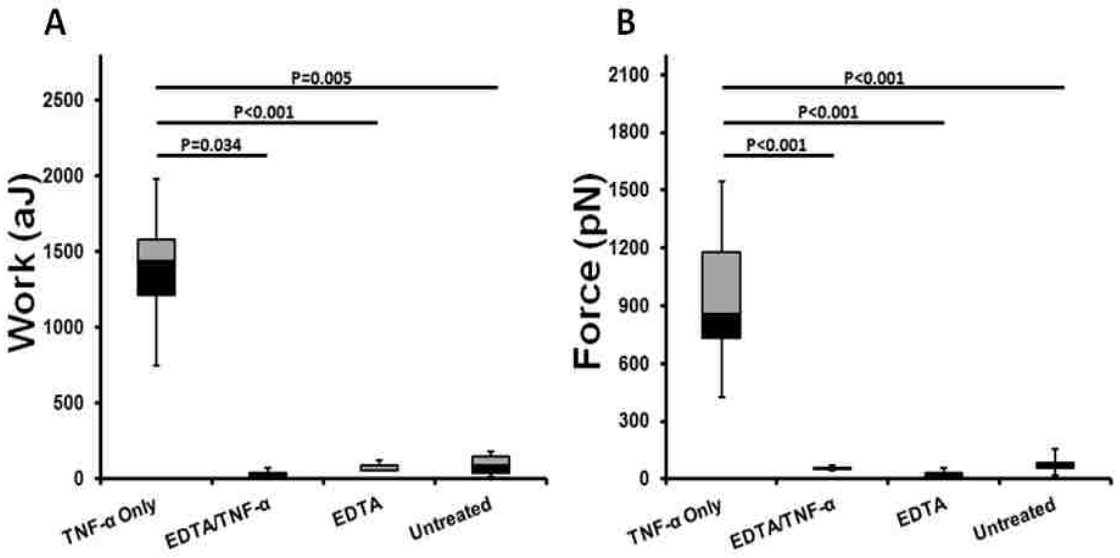

Figure 5.7: EDTA mediated TNF-α induced adhesion. (A) Work of deadhesion involved in rupturing all bonds between the K562 and the HUVEC. (B) Peak force required to separate the bound K562 from the HUVEC. Strong adhesion occurred between K562s and HUVECs treated with TNF-α (+ control). Adhesion between K562s bound to HUVECs after TNF-α by was reduced by the addition of EDTA. This was also seen when EDTA was added to the experiment on resting HUVECs. The – control has no treatment (HUVECs and K562s). The above p values denoted for (A) and (B) are from comparing the + control to both test conditions and the – control. N=10 cell-cell pairs for all experiments.

An additional fascinating result from this assay was the reduction of adhesive force between cells when they are treated with 20μg/mL hyaluronidase. This result has not been seen in L-selectin dependent cell rolling experiments when the cells were treated with 200mU/mL hyaluronidase (45). It may be explained by the proteoglycan CD44, which is expressed on HUVECS (18, 28, 40), serving as a ligand receptor for L-, P- and E- selectins. It has been shown that standard CD44 does bind to L-, P- and E-selectins at a low affinity during micro sphere rolling assays (49). Therefore, this study may illuminate the idea that there is a significant vertical component to this mechanism,

making the HA-CD44 complex a much more important binding mechanism than originally thought. Thus, the rolling cells may also be prevented from moving back into the blood stream by the HA-CD44 complex. Furthermore, CD44 is essential for HA degradation by hyaluronidase and is perhaps disrupted from L-, P- and E- selectin binding due to hyaluronidase exposure (50) which will reducing the number of available ligands able to bind these selectins expressed on the K562 cells and HUVECs.

The number of ligand ruptures per force scan was quantified for all experiments (Tables 5.1 and 2). Also, the number of ligand ruptures between the K562 and the HUVEC per μm^2 were quantified as the as a function of GAGs present on the cell surface (Fig. 5.8). The amount of GAGs removed was quantified from the WGA FITC fluorescence (Fig. 5.4). The figure shows a clear decrease in ligand ruptures for the TNF-α stimulated HUVECs as they are treated with hyaluronidase and/or heparanase I&III. Furthermore, this plot exhibits that for resting HUVECs there are more bonds that are formed after hyaluronidase and/or heparanase I&III treatment when compared to TNF-α stimulated HUVECs under the same digestive conditions. However, this does not correlate to a higher peak rupture force or dissociation work when compared to the TNF-α stimulated cells, particularly the ones exposed to hyaluronidase. Therefore, TNF-α is likely modifying the ligands.

	TNF-α (+Control)	TNF-α Hyaluronidase	TNF-α Heparanases	TNF-α Hep/Hya
Average Ruptures/Scan	9.45	6.91	4.23	4.23
Error (+/-)	0.276	0.569	0.817	0.722
Average Ruptures/μm^2	0.544	0.398	0.244	2.44
	TNF-α (Anti-MYC on K562)	TNF-α (DREG.200 on K562)	TNF-α EDTA	
Average Ruptures/Scan	9.57	< 2	< 2	
Error (+/-)	0.457	N/A	N/A	
Average Ruptures/μm^2	0.551	< 0.05	< 0.05	

Table 5.1: Ligand ruptures per scan for HUVECs stimulated with TNF-α.

	No Treatment (-Control)	Hyaluronidase	Heparanases
Average Ruptures/Scan	< 2	4.77	5.88
Error (+/-)	N/A	0.437	0.247
Average Ruptures/µm²	< 0.05	0.275	0.339
	Hep/Hya	EDTA	
Average Ruptures/Scan	5.29	< 2	
Error (+/-)	0.304	N/A	
Average Ruptures/µm²	0.31	< 0.05	

Table5.2: Ligand ruptures per scan for resting HUVECs.

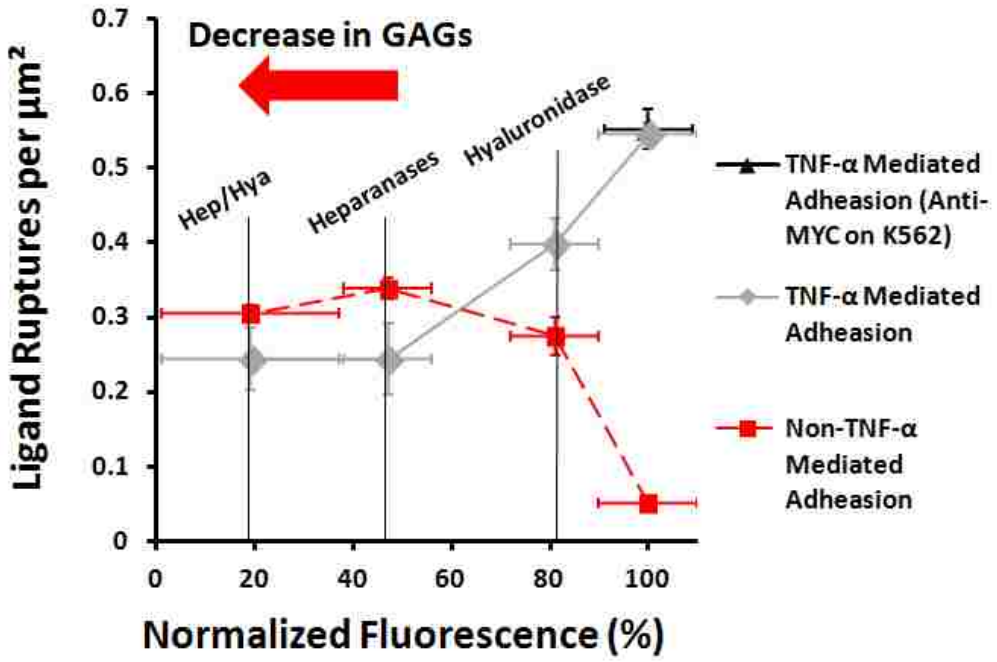

Figure 5.8: Ligand ruptures between the K562 and HUVEC. The ligand ruptures per µm2 quantified as a function of GAGs present on the cell surface as determined by the WGA FITC fluorescence. The –Control, TNF-α (DREG.200 on K562), EDTA, TNF-α EDTA, were excluded from this plot as there was < 0.05 per µm2 ruptures on average for these conditions. The vertical lines represent the types of enzymatic digestions.

The data gathered from this study demonstrated the normal forces involved in the initial steps of leukocyte adhesion to the endothelial wall. The experiments were preformed under cytokine induced inflammatory response conditions and/or exposure to ESG digesting enzymes such as heparinase I&III and/or hyaluronidase. We have

determined that the ESG layer serves two main functions: First, on resting endothelium, it prevents leukocyte adhesion, perhaps due to the electrostatic repulsion that the negatively charged GAGs have on the negatively charged leukocytes. Second, under inflammatory conditions, the ESG aggressively partakes in endothelial-leukocyte interactions, possibly by interactions between chemical moieties on GAG and leukocyte adhesion molecules such as selectins. These findings are among the first to investigate the forces involved in ESG dependent leukocyte adhesion over short contact times by the means of AFM. This assay lends support to previous leukocyte and monocyte rolling experiments and further expands the discussion to HA and CD44 being important cell rolling ligands. Knowledge of these forces will lead to a better understanding of pathological ESG shedding conditions as wells as inflammatory responses in the human body.

5.8.1 Appendix A: Statistics

To test for significant differences in the data sets, first a Shapiro-Wilk test was utilized to determine normality. If the normality criterion was met, a least significant difference (LSD) test was performed on the data via an ANOVA to determine the p values. If the normality criterion was not met, a Kruskal-Wallis H test was carried out; pairwise comparisons were performed with a Bonferroni correction to determine the adjusted p values. All p values are presented in the figures.

Work with no TNF-α (Figure 3A): An LSD test was performed. No significance was found between any of the treatment groups.

Force with no TNF-α (Figure 3B): Distributions of force were similar for all groups as assessed by visual inspection of a box and whiskers plot. Kruskal-Wallis H test was performed to determine if there were significant differences in force between the groups. Median forces were statistically different. $H(3) = 25.358$ with a $p < 0.001$. No significance was found between any of the treatment groups.

Work with TNF-α (Figure 4A): An LSD test was performed. No significance was found between any of the treatment groups.

Force with TNF-α (Figure 4B): Distributions of force were not similar for all groups as assessed by visual inspection of a box and whiskers plot. Kruskal-Wallis H test was performed to determine if there were significant differences in force between the groups. Median forces were statistically different. $H(4) = 35.432$ with a $p < 0.001$. No significance was found between any of the treatment groups.

Work with DREG.200 (Figure 5A): An LSD test was performed. Significance was found between two of the treatment groups: Anti-MYC and DREG.200.

Force with DREG.200 (Figure 5B): An LSD test was performed. Significance was found between two of the treatment groups: Anti-MYC and DREG.200.

Work with EDTA (Figure 6A): Distributions of force were not similar for all groups as assessed by visual inspection of a box and whiskers plot. Kruskal-Wallis H test was performed to determine if there were significant differences in force between the groups. Median forces were statistically different. $H(4) = 40.007$ with a $p < 0.001$. No significance was found between any of the treatment groups.

Force with EDTA (Figure 6B): Distributions of force were not similar for all groups as assessed by visual inspection of a box and whiskers plot. Kruskal-Wallis H test was performed to determine if there were significant differences in force between the groups. Median forces were statistically different. $H(4) = 26.523$ with a $p < 0.001$. No significance was found between any of the treatment groups.

5.8.2 Appendix B: Elasticity of K562s

To determine the elasticity of the K562s, first 22x22-1 glass sides were coated with poly-L-lysine. First, the slides were placed in acetone for 10 min, and then sterilized in a UV ozone chamber for 20 min. After removal from the chamber they were placed into a 0.2 M solution of $NaHCO_3$ in DI water (pH 9.0) containing a 200 µg/mL concentration of PLL. The slides were left to incubate in this solution over night at 4 ^{o}C. The slides were then washed with PBS 3x and placed into a 35 mm Cyto-One culture dish filled with 3 mL of the K562 culture medium. The K562s were then added and allowed to settle to the bottom where they were immobilized by the PLL.

After the dish was placed under the AFM, the cantilever was brought over top of the K562 and the scanning began. The probe contacting the K562 mimicked the cell being compressed between two flat plates. Force and depth were recorded for 20 cells with 20 scans performed on each cell. This information was passed to MatLab, where a numerical root finding method was utilized to solve equations 1 and 2 for Young's modulus (E) and contact radius (a). R is the radius of the K562 taken to be 10µm and ν is Poisson's ratio taken to be 0.5. For each scan the force (P) and compression distance (δ) where known. From this method E was determined to be 129±18 Pa and a was found to

be 2.54±0.8 µm, also the average force of indentation was 294±11 pN. This method was considered to be an analogue to the adhesion experiment because the 2 magnitudes of difference in cellular elasticity between the HUVECs and the K562s. Therefore, the HUVEC will be as incompressible as the glass when compared to the K562 and thus a good approximation of the K562 cell stiffness in the context of this experiment. Furthermore, the force of indentation was set to 300 pN and remained there reliably as it did in the above experiments. Profiles of the elasticity and contact radius are shown in histograms (Fig. 5.9).

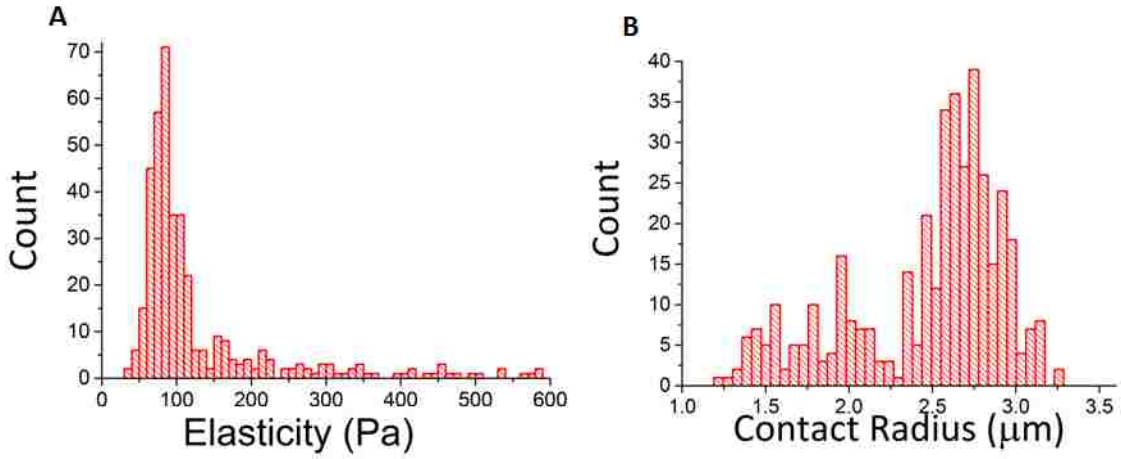

Figure 5.9: Elasticity and contact radius profiles of K562s. (A) Histogram distribution of Young's modulus fit to a with a median of 129±18Pa. (B) Histogram distribution of contact radius with a mean of 2.54±0.8µm. Both of these values were determined by solving equations 1 and 2 numerically for each scan, from which force (P) and compression distance (δ) where known.

Chapter 6: Investigation of the Reliability of AFM Nanoindentation-Derived Measurements of Cell Mechanics

6.1 Abstract

AFM, as an experimental technique, is often utilized for measuring the mechanical properties of cells and other soft materials. Despite its widespread adoption as a biophysical assay, no universal standards have been adopted for the technique and different research groups use varying methods and report cell elastic stiffness values that are at times divergent or contradictory. The purpose of this study was to study the accuracy and repeatability of AFM-derived cell stiffness measurements using comprehensive set experiments with a single cell type. AFM nano-indentation was performed on ASPC-1 (human pancreatic adenocarcinoma) cells to compare the following experimental conditions: conical vs. spherical AFM tips, nuclear vs. peripheral indentation locations, four actuation speeds (0.94, 1.88, 3.76, and 7.52 μm/s), and three indentation forces (100, 300, and 1000 pN). Each experimental condition was repeated with 40 cells. Apparent cell stiffness was calculated using classical contact mechanics with the Hertz model for the spherical tip and Sneddon model for the cone. Cell stiffness was log-transformed to achieve normality and between-groups comparisons were made using analysis of variance (ANOVA). Across all experimental conditions, cells appeared to be stiffer when probed with conical tips compared to spherical tips (all $P < 0.05$). There were no statistically significant differences in apparent cell stiffness based on AFM actuation speed or indentation force (all $P > 0.05$).

6.2 Introduction

AFM, beginning in the 1980s, has been utilized as a tool to investigate the properties of biological samples, such as cells and other micro-environments (29, 51). Since then the elastic properties of a variety of cell types have been studied with this technique. Cells such as HUVECs have had their elasticity estimated as a function of time during the early stage of cell culture (111, 112) with reported the elastic modulus being around 3.0–6.7 kPa (62, 111, 112). The Young's modulus of other cell types has also been studied. They include chondrocytes (0.6 kPa) (47), 3T3 fibroblasts (3–12 kPa) (107) and human chondrosarcoma cell (2 kPa) (23). This is of course just to name a few of the many cell types that have had their elasticy analyzed via AFM. At this point in time it is very important to bring attention to the following issue; clearly there is an enormous variation in reported values of cell elasticity, even for the same cell type. An eaxpmle being the above mentioned 3T3 fibroblasts. This problem has been attempted to be solved under several assumptions. One of the most prominent the assumptions is that cells should not be assumed to be linearly elastic as the aforementioned studies suppose. Thus, many other models ranging from composite material models (95, 117) to account for the ESG thickness and elasticity, to models that account for visco-elasticity (90) have been tried. However, these attempts fall short. They are still not reliable and can be very complicated to carry out, requiring very expensive equitment and expertise that is hard to come by. To further complicate the issue there is no standard procedure to carry out these experiments beyond the just the modeling of elasticity. Since cells are known to vary in elasticity as their time in culture continues (111, 112) and cells are

known to vary in elasticity if they are cultured on different substrates (73) agreement must reached on protocol. If this cannot be rectified the conflict in reporting is likley to continue. Therefore, the specific aims of this study were to investigate the role of indentation location, contact speed of the probe with the cell, the shape of the indentor, and the peak force used for the indentation (Fig. 6.1). This was done due to the fact that these were the most often varied parameters found in the literature as determined via an data minning study. Our results suggest that variations in tip shape and indentation force are likely to be causing the majority of the variations of cell elasticity calculations seen in the literature.

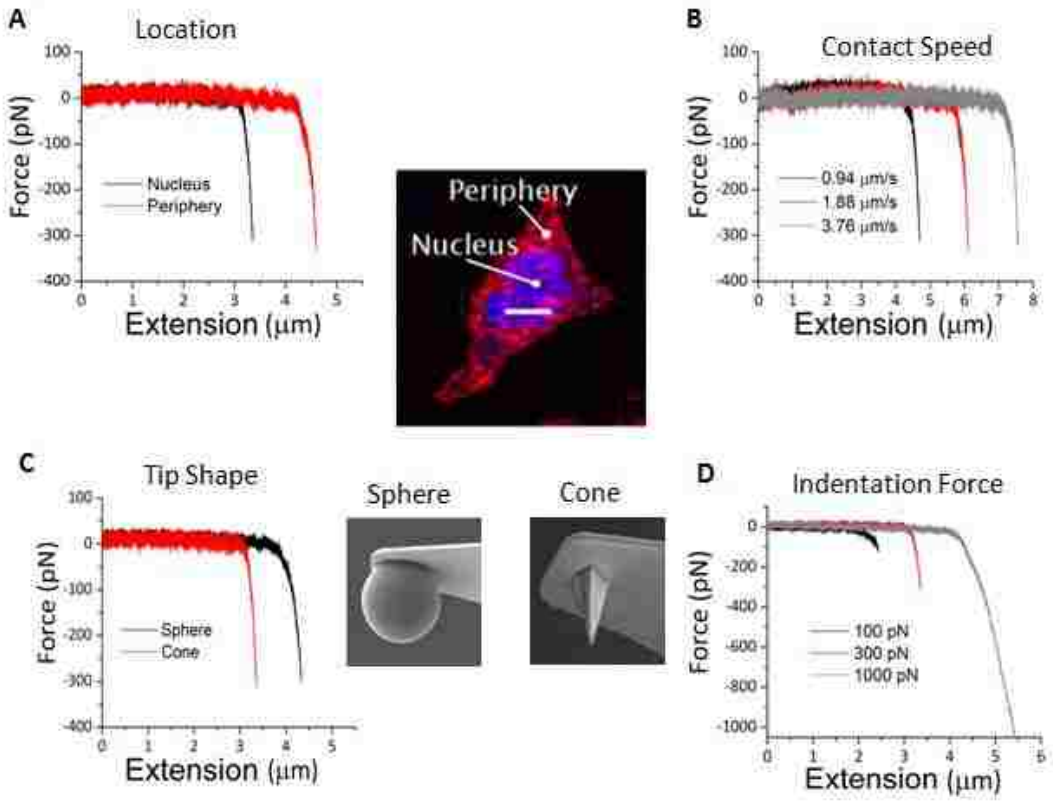

Figure 6.1: The experimental conditions. (A-D) Examples of AFM scans under the variations of the experimental conditions. (A) location was varied between the center of the cell and (nucleus) and the edge of the cell (periphery). (B) The speed of piezo actuation was varied using 0.94 µm/s, 1.88 µm/s, 3.76 µm/s. (C) Two tip shapes were used, spherical on conical. (D) Indentation force was varied using 100pN, 300pN and 1000pN. The above insert is an ASPC-1 cell stained with rhodamine phalloidin for F-actin and Hoechst 33258 for the nucleic acid (scale bar is 40 µm). The below insert s are EM images of AFM probe tips: Sphere (left) and cone (right).

6.3 Additional Background

There is no consesues on cellular elasticty results dervied from AFM and cells have yet to be conclusively shown to not be linearly elastic. Therefore, this assay sought to verify the assumptions of linear elasticty such to validate the tipical models used to determine cellular elasticty, namley the Sneddon and Hertz models. These models have several assumptions: The material is a semi-infinite half space, indentation deformations are

small, the surfaces in contact are ideally smooth (no fiction), and the material is homogenous and isotropic. Of couse cells violate the assumption of a semi-infinite half space and the is homogenous and isotropic assumption. However, it remains to be seen just how much of an affect these viloations have on the elasticity results. The equations are as follows:

$$F(d) = \frac{2E}{(1-\upsilon^2)} \frac{d^2}{\tan\theta} \qquad \textbf{Eq. 6.1}$$

$$F(d) = \frac{4}{3} \frac{E}{(1-\upsilon^2)} \sqrt{R} d^{3/2} \qquad \textbf{Eq. 6.2}$$

The first equation (Eq. 6.1) is known as the Sneddon model while the latter (Eq. 6.2) is the Hertz model. In both models E is Young's modulus, v is Poisson's ratio (0.5 for cells) and d is indentation depth. The Sneddon model is used to represent a conical indenter being pushed in to an elastic surface while the Hertz model used to represent a spherical indenter being pushed in to an elastic surface. In the Sneddon model, θ is the half angle of the opening of the cone. In the Hertz model R is the radius of the sphere.

6.4 Materials and Methods

Cell Culture: ASPC-1 (human pancreatic adenocarcinoma) from Sigma Aldrich were cells were passaged and incubated with Dulbecco's Modified Eagle's Medium (DMEM) containing 10% FBS from ATCC, 2% L-glutamine from Gibco by Life Technologies and 1% penicillin-streptomycin from Sigma-Aldrich. All cells were cultured in Corning t-25 flasks

and plated in experiments in 35 mm Cyto-One treated culture dishes 24 hrs prior to experiments or World Precision Instruments 35 mm FluoroDish glass bottom culture dishes for cell staining and imaging. The culture was maintained at 37 ^{o}C and 5% CO_2 in a water jacked incubator.

AFM Probes: The AFM probes used in this experiment were Bruker mode MLCT BIO--DC non-conductive silicon nitride (beta tested) and Bruker model MLCT-O10 tipless nitride levers modified by Novascan to have a 5 µm diameter bead made of borosilicate glass.

Cell Dyes: Hoechst 33258 pentahydrate (bis-benzimide), from ThermoFisher, was purchased as a powder and stored in 200 µL aliquots at a concentration of 10mg/mL at 4 ^{o}C. Rhodamine Phalloidin, from Life Technologies, was purchased as a powder and stored in a single aliquot of 1.5 mL at a concentration of 200 U/mL at 4 ^{o}C.

Atomic force microscopy (AFM) instrumentation: An AFM, in this experimental context, was used to first pick up the K562 cell and then press the cell against the HUVEC. The AFM used in all experiments was a custom built machine that was programmed using IGOR. The AFM was attached to a CCD camera with 20x objective capabilities, suspended from the ceiling via elastic cables and housed in a noise damping container. The spatial resolution of the AFM in the x-direction is approximately 1 nm and spatial resolution in the y-direction is approximately 15-20 pN.

Indentation Assay: A series of experiments were then conducted to compare the following conditions: conical vs. spherical AFM tips, nuclear vs. peripheral indentation locations, four actuation speeds (0.94, 1.88, 3.76, and 7.52 µm/s), and three indentation forces (100, 300, and 1000 pN). Each experimental condition was repeated with 40 cells.

Apparent cell stiffness was calculated using classical contact mechanics with the Hertz model for the spherical tip and Sneddon model for the cone. This was derived by fitting the AFM data for force v. tip position from the defined point of indentation to the highest indented force. Since all of the parameters from Eq. 6.1 and Eq. 6.2 are known except E (Young's modulus) could be determined by the fitting. Cell stiffness was log-transformed to achieve normality and between-groups comparisons were made using analysis of variance (ANOVA).

Cell Imaging Assay: Para-formaldehyde was prepared at 4 % W/V in PBS combined at 60 ^{o}C and then cooled to room temperature. Medium from cell culture dish was removed and 1mL of the para-formaldehyde solution was added to cells for 10 min. The para-formaldehyde solution was the removed from cells and the cells were washed 2x with 1mL PBS. Next a 0.5% Triton 100X solution in PBS was prepared. The PBS was removed from the cells and the Triton solution was added for 10min. The Triton solution was then removed and the cells were washed in 1 mL of PBS 2x. Then a 100 nM stock solution of rhodamine phalloidin was prepared by diluting 3.5 µl of 14 µM rhodamine phalloidin per 500 µl of PBS; this was kept at room temperature in the dark. The PBS was then removed from the cells and 1mL of rhodamine phalloidin solution was added to the cells. Finally the cells were incubated at room temp for 30 min or a 4 ^{o}C overnight. After the actin was stained for the nucleic acid was stained for with Hoechst 33258 at a concentration of 20 µg/mL for 5 min. The cell were then washed in 1 mL of PBS 2x. The images were taken on a Nikon Eclipse Ti with CFI Apo Lambda S 60x objective.

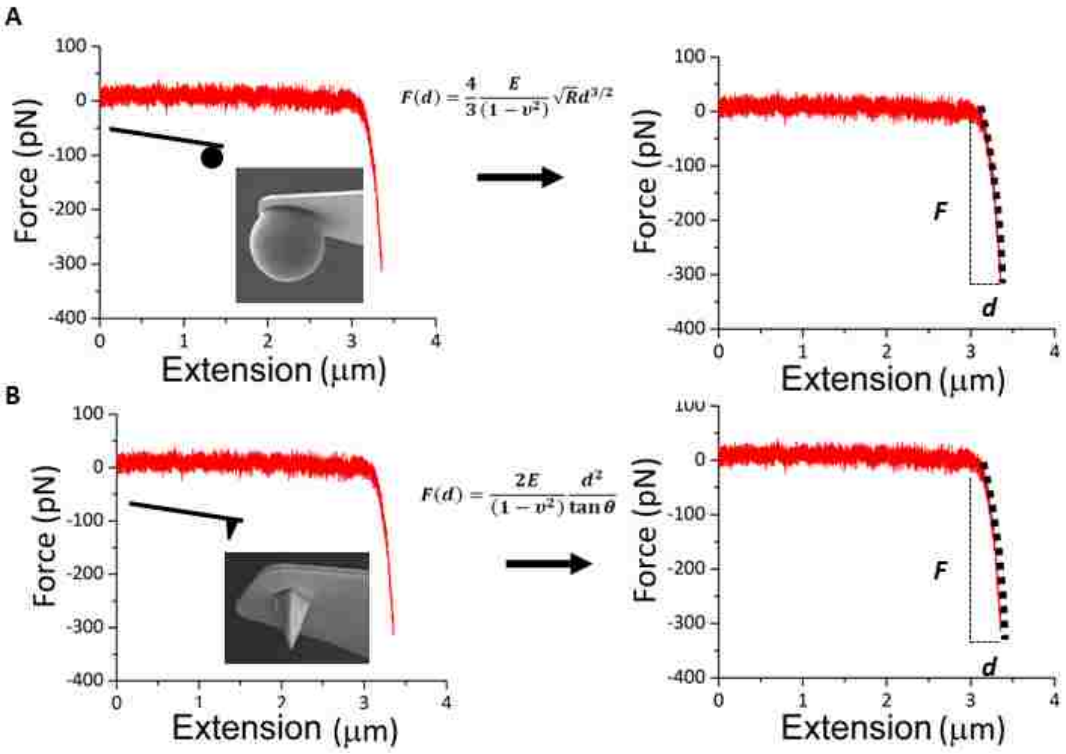

Figure 6.2: The experimental procedure. (A) After the indentation data for force v. tip position was gathered the point of contact between the probe and the cell was defined. This is where the fitting of the Hertz model took place (black dashed line). Force (F) is defined as the change in y position found from the point of contact and depth (d) is defined as the change in x position found from the point of contact. The apparent stiffness, which is Young's modulus or simply E in Eq. 3 and 4, was then determined from the fit of the Hertz model. (B) The exact same protocol was utilized for fitting the Sneddon model.

6.5 Results

After the nano-indentations had been carried out on the cells for every experimental condition the indentation curves produced by the AFM were subsequently fit to either the Hertz (spherical indenter) or Sneddon Model (conical indenter) as shown in Fig. 6.1. After the tip was aligned over either the nuclear region of the cell or the periphery region of the cell the AFM was set to cycle 20 indentations in that particular location. This resulted in a value for the apparent elasticity at that location. The elasticity values

for a single cell, nucleus or periphery, were non-normally distributed with positive skewness. Therefore, we analyzed between group variation via medians rather than means (Fig 6.3).

In the 40 cell groups, the distributions observed were also non-normal and exhibited a positive skewness, thus displaying a higher mean that median. Therefore, all data was log-transformed such to achieve normality. After this was performed parametric statists could be utilized to perform the between groups comparisons, in this case ANOVA with Tukey HSD post-hoc tests.

A box and whisker plot was chosen to display the results obtained via all experiments. Every box and whisker pair symbolizes the distribution for every 40 cell data set taken from each experimental condition. It can be seen in Fig. 6.3 that there are large variations between the predicted elasticity values for the cone and the sphere across all conditions. Moreover, Fig. 6.3 demonstrates the difference between the large amount of experimental conditions that were used in this experiment such as indentation speed and indentation force.

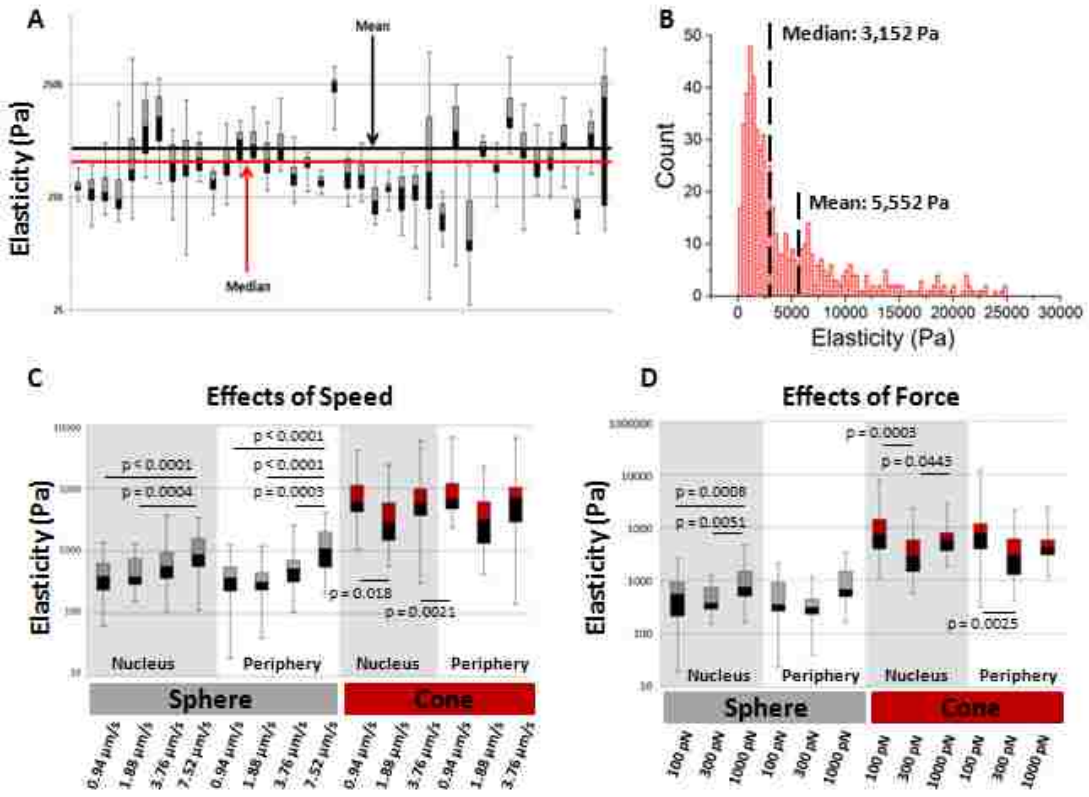

Figure 6.3: AFM results. After the nano-indentations were carried out on 40 cells a box and whiskers was made that demonstrates the between cell elasticity variation (A). Here, each individual box and whisker pair represents the distribution of the elasticity for 1 cell. A histogram comprised of the elasticity derived from each scan for all 40 cells was also created (B). The large variation between the mean and the median suggests that the data is non-normal with a positive skewness. Panels C and D are a box and whiskers plots that expresses the effects of probe speed and indentation force on the apparent elasticity of cells measured via AFM nano-indentation. Each individual box and whisker represents the elasticity distribution of all 40 cells for each experiment. The P values are located within the plots. The data was log-transformed to achieve normality and enable between-groups comparisons using parametric statistics (ANOVA with Tukey HSD post-hoc tests).

6.6 Discussion

After performing one of the largest parameter variations on a single cell type ever to be conducted we came to several conclusions. The first is that the choice of tip shape has a strong influence on the measured cellular elasticity. The use of conical tips

produced a higher value of apparent elasticity across all categories when compared to the spherical probe. This is perhaps due to the inhomogeneity that is seen in cells. When the conical indenter is used the AFM is essentially sampling a smaller region of the cell. Therefore, the between cell variations are likely to be very high as these smaller regions are likely to vary greatly. This can be seen in our data. When a histogram distribution of the apparent elasticity is plotted for the data gathered via a conical tip a greater skewness in the data can be observed when compared to data gathered via a spherical tip. Thus, we recommend that AFM studies be carried out with a spherical tip.

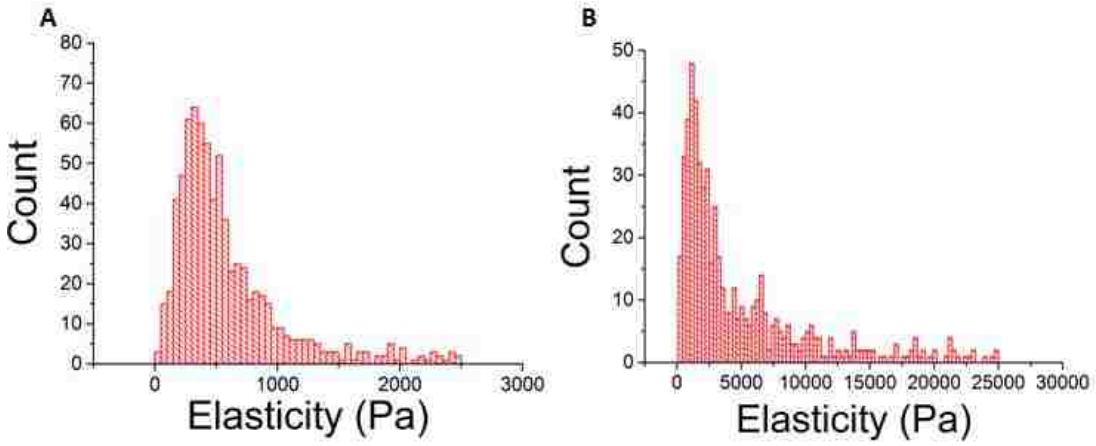

Figure 6.4: Spherical and conical indenter histograms. Comparing the elasticity profiles produced by combining the scans of a 40 cell sample (20 scans per cell) it can be seen that the histogram produced by the spherical indenter (A) has less skewness when compared to the histogram produced by the conical indenter (B).

Our data suggests that the location of the indentation, nucleus or periphery, makes little to no difference on the values of apparent stiffness. However, our AsPC-1 cells were relatively tall in comparison other cell types such as bEnd.3 cells, a rather short endothelial cell. This may have an altered the affects that the nucleus has on

apparent stiffness. In the future, AFM nanoindentation studies (at least on tall cells) may not need to differentiate between the nucleus and periphery.

Perhaps the most important and often unmentioned item in AFM experiments is the validity of the Hertz and Sneddon models Eq. 6.1 and Eq. 6.2. Both of these models assume that the cells are semi-infinite. This is of course not true. Therefore, when cells vary in height the ridged boundary will play an important role in the apparent elasticity of the cell, making shorter cells seem stiffer and taller cells seem softer. This problem should be solved by quantifying this potential for apparent stiffness amplification due to the rigid boundary effect experimentally.

The claim that cancer cells are softer than non-cancer cells is supported by most studies involving this topic (54, 102, 142). This is often attributed to the rearrangement of things such as the actin cytoskeleton that can be seen in cancer cells (102). However, cancer cells also exhibit a very bulky ESG (100). When considering the previous argument discussing the ridged boundary affecting the apparent elasticity of cells, so must a softer surface. Therefore, much of the loss in elasticity may be due to an increasing ESG, not simply interior cell variations. Future experimental studies should quantify the contribution of the glycocalyx to apparent cell stiffness.

Chapter 7: The Future of ESG Research

The ESG; a gel-like membrane bound layer comprised of a variety of proteoglycans and GAGs is located at the surface of all ECs, which line the walls of the entire vasculature. This layer is perhaps one of the most important aspects in the entire network of veins and arteries human body. It provides a protective coating that serves as a mediator of EC permeability, NO production as well as leukocyte adhesion, and inflammation. This thesis served to expand the knowledge on fundamental observations of the nature of the ESG; herein the structural, functional, and mechanical properties of ESG have been further characterized by the means of AFM and other micro- and nano-mechanical methods.

Although the structure and composition of the ESG have been well researched and understood for years, the general mechanical functions of the ESG have not yet been well investigated. This is due in part to a lack of techniques that are currently available to perform biological assays as well as the complexity of the system. The ESG is heterogeneous in its structure. It is filled with complex GAGs that attach to proteoglycans, some of which are transmembrane and share interactions with the actin cytoskeleton. Therefore, the mechanisms that have been outlined in this thesis are expected to be coupled in a non-linear fashion to several other mechanisms that have been previously discovered to perform tasks such as mechano-sensation or controlling cell adhesions. This is up to and including G-protein-coupled receptors, ion channels, tyrosine kinase receptors, cell adhesion molecules, caveolae, actin filaments as well as integrins (39).

The future of examinations of the ESG must include a variety of novel techniques that can analyze the unique complexities that this type of research can present. These techniques include further advancements in AFM technology and technique as well as the use of optical tweezers, magnetic tweezers and micro-fluidic devices. Also, further advancements in imaging techniques can be utilized and improved upon to be used in conjunction with devices such as AFM. These imaging techniques include super resolution devices such as stochastic optical reconstruction microscopy (STORM) and simulated emission depletion (STED) microscopy. Moreover, an understanding of useful yet misunderstood techniques, such as AFM nano-indentations must be achieved.

This Thesis sought to develop AFM technology and technique such to improve the understanding of the ESG's functions a mechanosensor and a mechanical controller of adhesion with further analysis on the methodology of AFM nano-indentation derived elastic measurements. From this effort a clearer picture has been developed of how the ESG allows ECs to produce NO in response to shear flow and how it controls inflammation in response to enzymatic degradation and cytokines has been developed. Furthermore, this thesis has brought a better understanding of AFM nano-indentation techniques to the forefront such to make it a more reliable form of investigation for such topics as ESG research. From the data presented here the power of an engineering approach to biological studies has been demonstrated.

References

1. **Adamson RH, and Clough G**. Plasma-Proteins Modify the Endothelial-Cell Glycocalyx of Frog Mesenteric Microvessels. *J Physiol-London* 445: 473-486, 1992.

2. **Adebiyi A, Narayanan D, and Jaggar JH**. Caveolin-1 Assembles Type 1 Inositol 1,4,5-Trisphosphate Receptors and Canonical Transient Receptor Potential 3 Channels into a Functional Signaling Complex in Arterial Smooth Muscle Cells. *Journal of Biological Chemistry* 286: 4341-4348, 2011.

3. **Algenstaedt P, Schaefer C, Biermann T, Hamann A, Schwarzloh B, Greten H, Ruther W, and Hansen-Algenstaedt N**. Microvascular alterations in diabetic mice correlate with level of hyperglycemia. *Diabetes* 52: 542-549, 2003.

4. **Arkill KP, Knupp C, Michel CC, Neal CR, Qvortrup K, Rostgaard J, and Squire JM**. Similar endothelial glycocalyx structures in microvessels from a range of mammalian tissues: evidence for a common filtering mechanism? *Biophysical journal* 101: 1046-1056, 2011.

5. **Arkill KP, Neal CR, Mantell JM, Michel CC, Qvortrup K, Rostgaard J, Bates DO, Knupp C, and Squire JM**. 3D Reconstruction of the Glycocalyx Structure in Mammalian Capillaries using Electron Tomography. *Microcirculation* 19: 343-351, 2012.

6. **Atkins ED, and Sheehan JK**. The molecular structure of hyaluronic acid. *The Biochemical journal* 125: 92P, 1971.

7. **Bai CX, Giamarchi A, Rodat-Despoix L, Padilla F, Downs T, Tsiokas L, and Delmas P**. Formation of a new receptor-operated channel by heteromeric assembly of TRPP2 and TRPC1 subunits. *EMBO reports* 9: 472-479, 2008.

8. **Bai K, and Wang W**. Spatio-temporal development of the endothelial glycocalyx layer and its mechanical property in vitro. *J R Soc Interface* 9: 2290-2298, 2012.

9. **Balijepalli RC, and Kamp TJ**. Caveolae, ion channels and cardiac arrhythmias. *Prog Biophys Mol Biol* 98: 149-160, 2008.

10. **Bellin RM, Kubicek JD, Frigault MJ, Kamien AJ, Steward RL, Jr., Barnes HM, Digiacomo MB, Duncan LJ, Edgerly CK, Morse EM, Park CY, Fredberg JJ, Cheng CM, and LeDuc PR**. Defining the role of syndecan-4 in mechanotransduction using surface-modification approaches. *Proceedings of the National Academy of Sciences of the United States of America* 106: 22102-22107, 2009.

11. **Berrout J, Jin M, and O'Neil RG**. Critical role of TRPP2 and TRPC1 channels in stretch-induced injury of blood-brain barrier endothelial cells. *Brain Research* 1436: 1-12, 2012.

12. **Bexelius TS, Ljung R, and Garcia Rodriguez LA**. Type 2 diabetes, high blood pressure and acute pancreatitis. *Hepatobiliary & pancreatic diseases international : HBPD INT* 15: 443-445, 2016.

13. **Birdsall HH, Lane C, Ramser MN, and Anderson DC**. Induction of VCAM-1 and ICAM-1 on human neural cells and mechanisms of mononuclear leukocyte adherence. *Journal of immunology* 148: 2717-2723, 1992.

14. **Buscher K, Riese SB, Shakibaei M, Reich C, Dernedde J, Tauber R, and Ley K**. The transmembrane domains of L-selectin and CD44 regulate receptor cell surface positioning and leukocyte adhesion under flow. *The Journal of biological chemistry* 285: 13490-13497, 2010.

15. **Chang YS, Yaccino JA, Lakshminarayanan S, Frangos JA, and Tarbell JM**. Shear-induced increase in hydraulic conductivity in endothelial cells is mediated by a nitric oxide-dependent mechanism. *Arteriosclerosis, thrombosis, and vascular biology* 20: 35-42, 2000.

16. **Chen ZL, Bakhshi FR, Shajahan AN, Sharma T, Mao M, Trane A, Bernatchez P, Amerongen GPV, Bonini MG, Skidgel RA, Malik AB, and Minshall RD**. Nitric oxide-dependent Src activation and resultant caveolin-1 phosphorylation promote eNOS/caveolin-1 binding and eNOS inhibition. *Molecular biology of the cell* 23: 1388-1398, 2012.

17. **Constantinescu AA, Vink H, and Spaan JA**. Endothelial cell glycocalyx modulates immobilization of leukocytes at the endothelial surface. *Arteriosclerosis, thrombosis, and vascular biology* 23: 1541-1547, 2003.

18. **Cooley LS, Handsley MM, Zhou Z, Lafleur MA, Pennington CJ, Thompson EW, Poschl E, and Edwards DR**. Reversible transdifferentiation of blood vascular endothelial cells to a lymphatic-like phenotype in vitro. *J Cell Sci* 123: 3808-3816, 2010.

19. **Couffinhal T, Duplaa C, Labat L, Lamaziere JM, Moreau C, Printseva O, and Bonnet J**. Tumor necrosis factor-alpha stimulates ICAM-1 expression in human vascular smooth muscle cells. *Arteriosclerosis and thrombosis : a journal of vascular biology / American Heart Association* 13: 407-414, 1993.

20. **Cruz-Chu ER, Malafeev A, Pajarskas T, Pivkin IV, and Koumoutsakos P**. Structure and response to flow of the glycocalyx layer. *Biophysical journal* 106: 232-243, 2014.

21. **Dai XQ, Karpinski E, and Chen XZ**. Permeation and inhibition of polycystin-L channel by monovalent organic cations. *Biochimica et biophysica acta* 1758: 197-205, 2006.

22. **Dai XQ, Ramji A, Liu Y, Li Q, Karpinski E, and Chen XZ**. Inhibition of TRPP3 channel by amiloride and analogs. *Molecular pharmacology* 72: 1576-1585, 2007.

23. **Darling EM, Zauscher S, Block JA, and Guilak F**. A thin-layer model for viscoelastic, stress-relaxation testing of cells using atomic force microscopy: Do cell properties reflect metastatic potential? *Biophysical journal* 92: 1784-1791, 2007.

24. **Davies PF**. Flow-Mediated Endothelial Mechanotransduction. *Physiological reviews* 75: 519-560, 1995.

25. **Devika NT, and Jaffar Ali BM**. Analysing calcium dependent and independent regulation of eNOS in endothelium triggered by extracellular signalling events. *Molecular bioSystems* 9: 2653-2664, 2013.

26. **Dietrich A, Chubanov V, Kalwa H, Rost BR, and Gudermann T**. Cation channels of the transient receptor potential superfamily: Their role in physiological and pathophysiological processes of smooth muscle cells. *Pharmacology & therapeutics* 112: 744-760, 2006.

27. **Drab M, Verkade P, Elger M, Kasper M, Lohn M, Lauterbach B, Menne J, Lindschau C, Mende F, Luft FC, Schedl A, Haller H, and Kurzchalia TV**. Loss of caveolae, vascular dysfunction, and pulmonary defects in caveolin-1 gene-disrupted mice. *Science* 293: 2449-2452, 2001.

28. **Draffin JE, McFarlane S, Hill A, Johnston PG, and Waugh DJ**. CD44 potentiates the adherence of metastatic prostate and breast cancer cells to bone marrow endothelial cells. *Cancer research* 64: 5702-5711, 2004.

29. **Drake B, Prater CB, Weisenhorn AL, Gould SAC, Albrecht TR, Quate CF, Cannell DS, Hansma HG, and Hansma PK**. Imaging Crystals, Polymers, and Processes in Water with the Atomic Force Microscope. *Science* 243: 1586-1589, 1989.

30. **Du XL, Edelstein D, Dimmeler S, Ju Q, Sui C, and Brownlee M**. Hyperglycemia inhibits endothelial nitric oxide synthase activity by posttranslational modification at the Akt site. *J Clin Invest* 108: 1341-1348, 2001.

31. **Ebong EE, Lopez-Quintero SV, Rizzo V, Spray DC, and Tarbell JM**. Shear-induced endothelial NOS activation and remodeling via heparan sulfate, glypican-1, and syndecan-1. *Integrative biology : quantitative biosciences from nano to macro* 6: 338-347, 2014.

32. **Ebong EE, Lopez-Quintero SV, Rizzo V, Spray DC, and Tarbell JM**. Shear-induced endothelial NOS activation and remodeling via heparan sulfate, glypican-1, and syndecan-1. *Integr Biol-Uk* 6: 338-347, 2014.

33. **Erlandsen SL, Hasslen SR, and Nelson RD**. Detection and spatial distribution of the beta 2 integrin (Mac-1) and L-selectin (LECAM-1) adherence receptors on human neutrophils by high-resolution field emission SEM. *The journal of histochemistry and cytochemistry : official journal of the Histochemistry Society* 41: 327-333, 1993.

34. **Feron O, Belhassen L, Kobzik L, Smith TW, Kelly RA, and Michel T**. Endothelial nitric oxide synthase targeting to caveolae - Specific interactions with caveolin isoforms

in cardiac myocytes and endothelial cells. *Journal of Biological Chemistry* 271: 22810-22814, 1996.

35. **Florian JA, Kosky JR, Ainslie K, Pang ZY, Dull RO, and Tarbell JM**. Heparan sulfate proteoglycan is a mechanosensor on endothelial cells. *Circulation research* 93: E136-E142, 2003.

36. **Forstermann U, and Munzel T**. Endothelial nitric oxide synthase in vascular disease - From marvel to menace. *Circulation* 113: 1708-1714, 2006.

37. **Fransson LA, Belting M, Cheng F, Jonsson M, Mani K, and Sandgren S**. Novel aspects of glypican glycobiology. *Cellular and molecular life sciences : CMLS* 61: 1016-1024, 2004.

38. **Freichel M, Suh SH, Pfeifer A, Schweig U, Trost C, Weissgerber P, Biel M, Philipp S, Freise D, Droogmans G, Hofmann F, Flockerzi V, and Nilius B**. Lack of an endothelial store-operated Ca2+ current impairs agonist-dependent vasorelaxation in TRP4(-)/(-) mice. *Nat Cell Biol* 3: 121-127, 2001.

39. **Fu BMM, and Tarbell JM**. Mechano-sensing and transduction by endothelial surface glycocalyx: composition, structure, and function. *Wiley Interdisciplinary Reviews-Systems Biology and Medicine* 5: 381-390, 2013.

40. **Fuchs K, Hippe A, Schmaus A, Homey B, Sleeman JP, and Orian-Rousseau V**. Opposing effects of high- and low-molecular weight hyaluronan on CXCL12-induced CXCR4 signaling depend on CD44. *Cell death & disease* 4: e819, 2013.

41. **Fux L, Ilan N, Sanderson RD, and Vlodavsky I**. Heparanase: busy at the cell surface. *Trends in biochemical sciences* 34: 511-519, 2009.

42. **Gaczynska M, Karpowicz P, Stuart CE, Norton MG, Teckman JH, Marszal E, and Osmulski PA**. AFM Imaging Reveals Topographic Diversity of Wild Type and Z Variant Polymers of Human alpha1-Proteinase Inhibitor. *PloS one* 11: e0151902, 2016.

43. **Gal I, Zhang J, Ko W, Glant TT, and Mikecz K**. Interaction of CD44 with RhoGDI through ezrin establishes a functional link between CD44 and the cytoskeleton. *Arthritis Rheum* 48: S271-S271, 2003.

44. **Gao L, and Lipowsky HH**. Composition of the endothelial glycocalyx and its relation to its thickness and diffusion of small solutes. *Microvascular research* 80: 394-401, 2010.

45. **Giuffre L, Cordey AS, Monai N, Tardy Y, Schapira M, and Spertini O**. Monocyte adhesion to activated aortic endothelium: role of L-selectin and heparan sulfate proteoglycans. *The Journal of cell biology* 136: 945-956, 1997.

46. **Gottlieb P, Folgering J, Maroto R, Raso A, Wood TG, Kurosky A, Bowman C, Bichet D, Patel A, Sachs F, Martinac B, Hamill OP, and Honore E**. Revisiting TRPC1 and TRPC6 mechanosensitivity. *Pflugers Archiv : European journal of physiology* 455: 1097-1103, 2008.

47. **Guilak F, Jones WR, Ting-Beall HP, and Lee GM**. The deformation behavior and mechanical properties of chondrocytes in articular cartilage. *Osteoarthr Cartilage* 7: 59-70, 1999.

48. **Han YF, Weinbaum S, Spaan JAE, and Vink H**. Large-deformation analysis of the elastic recoil of fibre layers in a Brinkman medium with application to the endothelial glycocalyx. *J Fluid Mech* 554: 217-235, 2006.

49. **Hanley WD, Napier SL, Burdick MM, Schnaar RL, Sackstein R, and Konstantopoulos K**. Variant isoforms of CD44 are P- and L-selectin ligands on colon carcinoma cells. *FASEB journal : official publication of the Federation of American Societies for Experimental Biology* 20: 337-339, 2006.

50. **Harada H, and Takahashi M**. CD44-dependent intracellular and extracellular catabolism of hyaluronic acid by hyaluronidase-1 and -2. *The Journal of biological chemistry* 282: 5597-5607, 2007.

51. **Henderson E**. Imaging of Living Cells by Atomic-Force Microscopy. *Prog Surf Sci* 46: 39-60, 1994.

52. **Henry CBS, and Duling BR**. TNF-alpha increases entry of macromolecules into luminal endothelial cell glycocalyx. *Am J Physiol-Heart C* 279: H2815-H2823, 2000.

53. **Hinterdorfer P, and Dufrene YF**. Detection and localization of single molecular recognition events using atomic force microscopy. *Nature methods* 3: 347-355, 2006.

54. **Hou HW, Li QS, Lee GY, Kumar AP, Ong CN, and Lim CT**. Deformability study of breast cancer cells using microfluidics. *Biomedical microdevices* 11: 557-564, 2009.

55. **Hsieh HJ, Liu CA, Huang B, Tseng AHH, and Wang DL**. Shear-induced endothelial mechanotransduction: the interplay between reactive oxygen species (ROS) and nitric oxide (NO) and the pathophysiological implications. *J Biomed Sci* 21: 2014.

56. **Hughes ML, and Dougan L**. The physics of pulling polyproteins: a review of single molecule force spectroscopy using the AFM to study protein unfolding. *Reports on progress in physics Physical Society* 79: 076601, 2016.

57. **Hui TH, Zhou ZL, Qian J, Lin Y, Ngan AH, and Gao H**. Volumetric deformation of live cells induced by pressure-activated cross-membrane ion transport. *Physical review letters* 113: 118101, 2014.

58. **Hutter JL, and Bechhoefer J**. Calibration of Atomic-Force Microscope Tips (Vol 64, Pg 1868, 1993). *Review of Scientific Instruments* 64: 3342-3342, 1993.

59. **Ihrcke NS, Wrenshall LE, Lindman BJ, and Platt JL**. Role of heparan sulfate in immune system-blood vessel interactions. *Immunology today* 14: 500-505, 1993.

60. **Jackson RL, Busch SJ, and Cardin AD**. Glycosaminoglycans: molecular properties, protein interactions, and role in physiological processes. *Physiological reviews* 71: 481-539, 1991.

61. **Jung TM, Gallatin WM, Weissman IL, and Dailey MO**. Down-regulation of homing receptors after T cell activation. *Journal of immunology* 141: 4110-4117, 1988.

62. **Kataoka N, Iwaki K, Hashimoto K, Mochizuki S, Ogasawara Y, Sato M, Tsujioka K, and Kajiya F**. Measurements of endothelial cell-to-cell and cell-to-substrate gaps and micromechanical properties of endothelial cells during monocyte adhesion. *Proceedings of the National Academy of Sciences of the United States of America* 99: 15638-15643, 2002.

63. **Kishimoto TK, Jutila MA, and Butcher EC**. Identification of a human peripheral lymph node homing receptor: a rapidly down-regulated adhesion molecule. *Proceedings of the National Academy of Sciences of the United States of America* 87: 2244-2248, 1990.

64. **Koenig A, Norgard-Sumnicht K, Linhardt R, and Varki A**. Differential interactions of heparin and heparan sulfate glycosaminoglycans with the selectins - Implications for the use of unfractionated and low molecular weight heparins as therapeutic agents. *J Clin Invest* 101: 877-889, 1998.

65. **Kohler R, Heyken WT, Heinau P, Schubert R, Si H, Kacik M, Busch C, Grgic I, Maier T, and Hoyer J**. Evidence for a functional role of endothelial transient receptor potential V4 in shear stress-induced vasodilatation. *Arteriosclerosis, thrombosis, and vascular biology* 26: 1495-1502, 2006.

66. **Kuchan MJ, and Frangos JA**. Role of calcium and calmodulin in flow-induced nitric oxide production in endothelial cells. *The American journal of physiology* 266: C628-636, 1994.

67. **Kuchan MJ, Jo H, and Frangos JA**. Role of G proteins in shear stress-mediated nitric oxide production by endothelial cells. *The American journal of physiology* 267: C753-758, 1994.

68. **Kusche-Vihrog K, and Oberleithner H**. An emerging concept of vascular salt sensitivity. *F1000 Biol Rep* 4: 20, 2012.

69. **Kuznetsova TG, Starodubtseva MN, Yegorenkov NI, Chizhik SA, and Zhdanov RI**. Atomic force microscopy probing of cell elasticity. *Micron* 38: 824-833, 2007.

70. **Latkovic S**. Ultrastructural localization of lectin-binding sites on the surface of the guinea pig conjunctival epithelium. *Graefe's archive for clinical and experimental ophthalmology = Albrecht von Graefes Archiv fur klinische und experimentelle Ophthalmologie* 229: 153-156, 1991.

71. **Lever R, Rose MJ, McKenzie EA, and Page CP**. Heparanase induces inflammatory cell recruitment in vivo by promoting adhesion to vascular endothelium. *American journal of physiology Cell physiology* 306: C1184-1190, 2014.

72. **Ley K, Tedder TF, and Kansas GS**. L-Selectin Can Mediate Leukocyte Rolling in Untreated Mesenteric Venules in-Vivo Independent of E-Selection or P-Selectin. *Blood* 82: 1632-1638, 1993.

73. **Liang XB, Shi XT, Ostrovidov S, Wu HK, and Nakajima K**. Probing stem cell differentiation using atomic force microscopy. *Appl Surf Sci* 366: 254-259, 2016.

74. **Libby P**. Inflammation in atherosclerosis. *Nature* 420: 868-874, 2002.

75. **Liu Y, Li Q, Tan M, Zhang YY, Karpinski E, Zhou J, and Chen XZ**. Modulation of the human polycystin-L channel by voltage and divalent cations. *FEBS letters* 525: 71-76, 2002.

76. **Long DS, Smith ML, Pries AR, Ley K, and Damiano ER**. Microviscometry reveals reduced blood viscosity and altered shear rate and shear stress profiles in microvessels after hemodilution. *Proceedings of the National Academy of Sciences of the United States of America* 101: 10060-10065, 2004.

77. **Lozzio BB, Lozzio CB, Bamberger EG, and Feliu AS**. A multipotential leukemia cell line (K-562) of human origin. *Proceedings of the Society for Experimental Biology and Medicine Society for Experimental Biology and Medicine* 166: 546-550, 1981.

78. **Luft JH**. Fine structures of capillary and endocapillary layer as revealed by ruthenium red. *Federation proceedings* 25: 1773-1783, 1966.

79. **Ma XL, Weyrich AS, Lefer DJ, Buerke M, Albertine KH, Kishimoto TK, and Lefer AM**. Monoclonal antibody to L-selectin attenuates neutrophil accumulation and protects ischemic reperfused cat myocardium. *Circulation* 88: 649-658, 1993.

80. **Maroto R, Raso A, Wood TG, Kurosky A, Martinac B, and Hamill OP**. TRPC1 forms the stretch-activated cation channel in vertebrate cells. *Nat Cell Biol* 7: 179-185, 2005.

81. **Megens RTA, Reitsma S, Schiffers PHM, Hilgers RHP, De Mey JGR, Slaaf DW, Egbrink MGAO, and van Zandvoort MAMJ**. Two-photon microscopy of vital murine elastic and muscular arteries - Combined structural and functional imaging with subcellular resolution. *Journal of vascular research* 44: 87-98, 2007.

82. **Michel JB, Feron O, Sacks D, and Michel T**. Reciprocal regulation of endothelial nitric-oxide synthase by Ca2+-calmodulin and caveolin. *The Journal of biological chemistry* 272: 15583-15586, 1997.

83. **Mitchell MJ, and King MR**. Physical Biology in Cancer. 3. The role of cell glycocalyx in vascular transport of circulating tumor cells. *Am J Physiol-Cell Ph* 306: C89-C97, 2014.

84. **Mochizuki S, Vink H, Hiramatsu O, Kajita T, Shigeto F, Spaan JAE, and Kajiya F**. Role of hyaluronic acid glycosaminoglycans in shear-induced endothelium-derived nitric oxide release. *Am J Physiol-Heart C* 285: H722-H726, 2003.

85. **Montell C, and Rubin GM**. Molecular characterization of the Drosophila trp locus: a putative integral membrane protein required for phototransduction. *Neuron* 2: 1313-1323, 1989.

86. **Moore KL, Patel KD, Bruehl RE, Li F, Johnson DA, Lichenstein HS, Cummings RD, Bainton DF, and McEver RP**. P-selectin glycoprotein ligand-1 mediates rolling of human neutrophils on P-selectin. *The Journal of cell biology* 128: 661-671, 1995.

87. **Nandi A, Estess P, and Siegelman MH**. Hyaluronan anchoring and regulation on the surface of vascular endothelial cells is mediated through the functionally active form of CD44. *The Journal of biological chemistry* 275: 14939-14948, 2000.

88. **Nathan DM, Lachin J, Cleary P, Orchard T, Brillon DJ, Backlund JY, O'Leary DH, Genuth S, Diabetes C, Complications T, Epidemiology of Diabetes I, and Complications Research G**. Intensive diabetes therapy and carotid intima-media thickness in type 1 diabetes mellitus. *The New England journal of medicine* 348: 2294-2303, 2003.

89. **Nauli SM, Alenghat FJ, Luo Y, Williams E, Vassilev P, Li X, Elia AE, Lu W, Brown EM, Quinn SJ, Ingber DE, and Zhou J**. Polycystins 1 and 2 mediate mechanosensation in the primary cilium of kidney cells. *Nature genetics* 33: 129-137, 2003.

90. **Nawaz S, Sanchez P, Bodensiek K, Li S, Simons M, and Schaap IAT**. Cell Visco-Elasticity Measured with AFM and Vertical Optical Trapping at Sub-Micrometer Deformations. *Biophysical journal* 104: 478a-478a, 2013.

91. **Nelson RM, Cecconi O, Roberts WG, Aruffo A, Linhardt RJ, and Bevilacqua MP**. Heparin oligosaccharides bind L- and P-selectin and inhibit acute inflammation. *Blood* 82: 3253-3258, 1993.

92. **Nieuwdorp M, Mooij HL, Kroon J, Atasever B, Spaan JAE, Ince C, Holleman F, Diamant M, Heine RJ, Hoekstra JBL, Kastelein JJP, Stroes ESG, and Vink H**. Endothelial

glycocalyx damage coincides with microalbuminuria in type 1 diabetes. *Diabetes* 55: 1127-1132, 2006.

93. **Nijenhuis N, Mizuno D, Spaan JAE, and Schmidt CF**. Viscoelastic response of a model endothelial glycocalyx. *Phys Biol* 6: 2009.

94. **Norgardsumnicht K, and Varki A**. Endothelial Heparan-Sulfate Proteoglycans That Bind to L-Selectin Have Glucosamine Residues with Unsubstituted Amino-Groups. *Journal of Biological Chemistry* 270: 12012-12024, 1995.

95. **O'Callaghan R, Job KM, Dull RO, and Hlady V**. Stiffness and heterogeneity of the pulmonary endothelial glycocalyx measured by atomic force microscopy. *Am J Physiol-Lung C* 301: L353-L360, 2011.

96. **Oberleithner H, Peters W, Kusche-Vihrog K, Korte S, Schillers H, Kliche K, and Oberleithner K**. Salt overload damages the glycocalyx sodium barrier of vascular endothelium. *Pflugers Archiv-European Journal of Physiology* 462: 519-528, 2011.

97. **Ohlson M, Sorensson J, and Haraldsson B**. A gel-membrane model of glomerular charge and size selectivity in series. *American journal of physiology Renal physiology* 280: F396-405, 2001.

98. **Pahakis MY, Kosky JR, Dull RO, and Tarbell JM**. The role of endothelial glycocalyx components in mechanotransduction of fluid shear stress. *Biochemical and biophysical research communications* 355: 228-233, 2007.

99. **Pai R, Bassa B, Kirschenbaum MA, and Kamanna VS**. TNF-alpha stimulates monocyte adhesion to glomerular mesangial cells. The role of intercellular adhesion

molecule-1 gene expression and protein kinases. *Journal of immunology* 156: 2571-2579, 1996.

100. **Paszek MJ, Boettiger D, Weaver VM, and Hammer DA**. Integrin clustering is driven by mechanical resistance from the glycocalyx and the substrate. *PLoS computational biology* 5: e1000604, 2009.

101. **Patel A, Sharif-Naeini R, Folgering JR, Bichet D, Duprat F, and Honore E**. Canonical TRP channels and mechanotransduction: from physiology to disease states. *Pflugers Archiv : European journal of physiology* 460: 571-581, 2010.

102. **Plodinec M, Loparic M, Monnier CA, Obermann EC, Zanetti-Dallenbach R, Oertle P, Hyotyla JT, Aebi U, Bentires-Alj M, Lim RY, and Schoenenberger CA**. The nanomechanical signature of breast cancer. *Nature nanotechnology* 7: 757-765, 2012.

103. **Pries AR, Secomb TW, and Gaehtgens P**. The endothelial surface layer. *Pflugers Archiv : European journal of physiology* 440: 653-666, 2000.

104. **Reitsma S, Slaaf DW, Vink H, van Zandvoort MA, and oude Egbrink MG**. The endothelial glycocalyx: composition, functions, and visualization. *Pflugers Archiv : European journal of physiology* 454: 345-359, 2007.

105. **Renzaho AM, Bilal P, and Marks GC**. Obesity, type 2 diabetes and high blood pressure amongst recently arrived Sudanese refugees in Queensland, Australia. *Journal of immigrant and minority health* 16: 86-94, 2014.

106. **Rops AL, van der Vlag J, Lensen JF, Wijnhoven TJ, van den Heuvel LP, van Kuppevelt TH, and Berden JH**. Heparan sulfate proteoglycans in glomerular inflammation. *Kidney international* 65: 768-785, 2004.

107. **Rotsch C, Jacobson K, and Radmacher M**. Dimensional and mechanical dynamics of active and stable edges in motile fibroblasts investigated by using atomic force microscopy. *Proceedings of the National Academy of Sciences of the United States of America* 96: 921-926, 1999.

108. **Saber R, Sarkar S, Gill P, Nazari B, and Faridani F**. High resolution imaging of IgG and IgM molecules by scanning tunneling microscopy in air condition. *Sci Iran* 18: 1643-1646, 2011.

109. **Sabri S, Soler M, Foa C, Pierres A, Benoliel AM, and Bongrand P**. Glycocalyx modulation is a physiological means of regulating cell adhesion. *J Cell Sci* 113: 1589-1600, 2000.

110. **Sarrazin S, Lamanna WC, and Esko JD**. Heparan sulfate proteoglycans. *Cold Spring Harbor perspectives in biology* 3: 2011.

111. **Sato H, Katano M, Takigawa T, and Masuda T**. Estimation for the elasticity of vascular endothelial cells on the basis of atomic force microscopy and Young's modulus of gelatin gels. *Polym Bull* 47: 375-381, 2001.

112. **Sato H, Kataoka N, Kajiya F, Katano M, Takigawa T, and Masuda T**. Kinetic study on the elastic change of vascular endothelial cells on collagen matrices by atomic force microscopy. *Colloid Surface B* 34: 141-146, 2004.

113. **Secomb TW, Hsu R, and Pries AR**. Effect of the endothelial surface layer on transmission of fluid shear stress to endothelial cells. *Biorheology* 38: 143-150, 2001.

114. **Shriver Z, Capila I, Venkataraman G, and Sasisekharan R**. Heparin and heparan sulfate: analyzing structure and microheterogeneity. *Handbook of experimental pharmacology* 159-176, 2012.

115. **Singer M, Deutschman CS, Seymour CW, Shankar-Hari M, Annane D, Bauer M, Bellomo R, Bernard GR, Chiche JD, Coopersmith CM, Hotchkiss RS, Levy MM, Marshall JC, Martin GS, Opal SM, Rubenfeld GD, van der Poll T, Vincent JL, and Angus DC**. The Third International Consensus Definitions for Sepsis and Septic Shock (Sepsis-3). *Jama-J Am Med Assoc* 315: 801-810, 2016.

116. **Snapp KR, Wagers AJ, Craig R, Stoolman LM, and Kansas GS**. P-selectin glycoprotein ligand-1 is essential for adhesion to P-selectin but not E-selectin in stably transfected hematopoietic cell lines. *Blood* 89: 896-901, 1997.

117. **Sokolov I, Iyer S, Subba-Rao V, Gaikwad RM, and Woodworth CD**. Detection of surface brush on biological cells in vitro with atomic force microscopy. *Appl Phys Lett* 91: 2007.

118. **Soler M, Desplat-Jego S, Vacher B, Ponsonnet L, Fraterno M, Bongrand P, Martin JM, and Foa C**. Adhesion-related glycocalyx study: quantitative approach with imaging-spectrum in the energy filtering transmission electron microscope (EFTEM). *FEBS letters* 429: 89-94, 1998.

119. **Sorensson J, Ohlson M, and Haraldsson B**. A quantitative analysis of the glomerular charge barrier in the rat. *American journal of physiology Renal physiology* 280: F646-656, 2001.

120. **Spooner CE, Markowitz NP, and Saravolatz LD**. The role of tumor necrosis factor in sepsis. *Clinical immunology and immunopathology* 62: S11-17, 1992.

121. **Springer TA**. Adhesion Receptors of the Immune-System. *Nature* 346: 425-434, 1990.

122. **Springer TA**. Traffic signals for lymphocyte recirculation and leukocyte emigration: the multistep paradigm. *Cell* 76: 301-314, 1994.

123. **Squire JM, Chew M, Nneji G, Neal C, Barry J, and Michel C**. Quasi-periodic substructure in the microvessel endothelial glycocalyx: a possible explanation for molecular filtering? *Journal of structural biology* 136: 239-255, 2001.

124. **Stan RV**. Structure of caveolae. *Biochimica et biophysica acta* 1746: 334-348, 2005.

125. **Stein JV, Cheng G, Stockton BM, Fors BP, Butcher EC, and von Andrian UH**. L-selectin-mediated leukocyte adhesion in vivo: microvillous distribution determines tethering efficiency, but not rolling velocity. *The Journal of experimental medicine* 189: 37-50, 1999.

126. **Sundivakkam PC, Kwiatek AM, Sharma TT, Minshall RD, Malik AB, and Tiruppathi C**. Caveolin-1 scaffold domain interacts with TRPC1 and IP3R3 to regulate Ca2+ store release-induced Ca2+ entry in endothelial cells. *American journal of physiology Cell physiology* 296: C403-413, 2009.

127. **Tarbell JM, and Pahakis MY**. Mechanotransduction and the glycocalyx. *Journal of internal medicine* 259: 339-350, 2006.

128. **Thi MM, Tarbell JM, Weinbaum S, and Spray DC**. The role of the glycocalyx in reorganization of the actin cytoskeleton under fluid shear stress: A "bumper-car" model. *Proceedings of the National Academy of Sciences of the United States of America* 101: 16483-16488, 2004.

129. **Tkachenko E, Rhodes JM, and Simons M**. Syndecans - New kids on the signaling block. *Circulation research* 96: 488-500, 2005.

130. **Tsiokas L**. Function and regulation of TRPP2 at the plasma membrane. *Am J Physiol-Renal* 297: F1-F9, 2009.

131. **van den Berg BM, Vink H, and Spaan JAE**. The endothelial glycocalyx protects against myocardial edema. *Circulation research* 92: 592-594, 2003.

132. **Venkatachalam K, and Montell C**. TRP channels. *Annual review of biochemistry* 76: 387-417, 2007.

133. **Vink H, Constantinescu AA, and Spaan JA**. Oxidized lipoproteins degrade the endothelial surface layer : implications for platelet-endothelial cell adhesion. *Circulation* 101: 1500-1502, 2000.

134. **Vink H, Constantinescu AA, and Spaan JAE**. Oxidized lipoproteins degrade the endothelial surface layer - Implications for platelet-endothelial cell adhesion. *Circulation* 101: 1500-1502, 2000.

135. **Vink H, and Duling BR**. Identification of distinct luminal domains for macromolecules, erythrocytes, and leukocytes within mammalian capillaries. *Circulation research* 79: 581-589, 1996.

136. **Vlahu CA, Lemkes BA, Struijk DG, Koopman MG, Krediet RT, and Vink H**. Damage of the Endothelial Glycocalyx in Dialysis Patients. *Journal of the American Society of Nephrology* 23: 1900-1908, 2012.

137. **Waage A, Halstensen A, and Espevik T**. Association between Tumor-Necrosis-Factor in Serum and Fatal Outcome in Patients with Meningococcal Disease. *Lancet* 1: 355-357, 1987.

138. **Walcheck B, Kahn J, Fisher JM, Wang BB, Fisk RS, Payan DG, Feehan C, Betageri R, Darlak K, Spatola AF, and Kishimoto TK**. Neutrophil rolling altered by inhibition of L-selectin shedding in vitro. *Nature* 380: 720-723, 1996.

139. **Wang L, Fuster M, Sriramarao P, and Esko JD**. Endothelial heparan sulfate deficiency impairs L-selectin- and chemokine-mediated neutrophil trafficking during inflammatory responses. *Nature immunology* 6: 902-910, 2005.

140. **Weinbaum S, Tarbell JM, and Damiano ER**. The structure and function of the endothelial glycocalyx layer. *Annual review of biomedical engineering* 9: 121-167, 2007.

141. **Weinbaum S, Zhang XB, Han YF, Vink H, and Cowin SC**. Mechanotransduction and flow across the endothelial glycocalyx. *Proceedings of the National Academy of Sciences of the United States of America* 100: 7988-7995, 2003.

142. **Xu W, Mezencev R, Kim B, Wang L, McDonald J, and Sulchek T**. Cell stiffness is a biomarker of the metastatic potential of ovarian cancer cells. *PloS one* 7: e46609, 2012.

143. **Yang Y, and Schmidt EP**. The endothelial glycocalyx: an important regulator of the pulmonary vascular barrier. *Tissue Barriers* 1: 2013.

144. **Yao Y, Rabodzey A, and Dewey CF**. Glycocalyx modulates the motility and proliferative response of vascular endothelium to fluid shear stress. *Am J Physiol-Heart C* 293: H1023-H1030, 2007.

145. **Ye F, Liu J, Winkler H, and Taylor KA**. Integrin alpha(IIb)beta(3) in a membrane environment remains the same height after Mn2+ activation when observed by cryoelectron tomography. *Journal of molecular biology* 378: 976-986, 2008.

146. **Yuan W, Li G, Gil ES, Lowe TL, and Fu BM**. Effect of surface charge of immortalized mouse cerebral endothelial cell monolayer on transport of charged solutes. *Annals of biomedical engineering* 38: 1463-1472, 2010.

147. **Zakrzewicz A, Grafe M, Terbeek D, Bongrazio M, Auch-Schwelk W, Walzog B, Graf K, Fleck E, Ley K, and Gaehtgens P**. L-selectin-dependent leukocyte adhesion to microvascular but not to macrovascular endothelial cells of the human coronary system. *Blood* 89: 3228-3235, 1997.

148. **Zeng Y, Ebong EE, Fu BM, and Tarbell JM**. The structural stability of the endothelial glycocalyx after enzymatic removal of glycosaminoglycans. *PloS one* 7: e43168, 2012.

149. **Zhang P, Luo Y, Chasan B, Gonzalez-Perrett S, Montalbetti N, Timpanaro GA, Cantero Mdel R, Ramos AJ, Goldmann WH, Zhou J, and Cantiello HF**. The multimeric structure of polycystin-2 (TRPP2): structural-functional correlates of homo- and hetero-multimers with TRPC1. *Human molecular genetics* 18: 1238-1251, 2009.

150. **Zhang X, Chen A, De Leon D, Li H, Noiri E, Moy VT, and Goligorsky MS**. Atomic force microscopy measurement of leukocyte-endothelial interaction. *American journal of physiology Heart and circulatory physiology* 286: H359-367, 2004.

151. **Zhang ZR, Chu WF, Song B, Gooz M, Zhang JN, Yu CJ, Jiang S, Baldys A, Gooz P, Steele S, Owsianik G, Nilius B, Komlosi P, and Bell PD**. TRPP2 and TRPV4 form an EGF-activated calcium permeable channel at the apical membrane of renal collecting duct cells. *PloS one* 8: e73424, 2013.

152. **Zhao JH, Nagao S, and Zhang ZL**. Loading and unloading of a spherical contact: From elastic to elastic-perfectly plastic materials. *Int J Mech Sci* 56: 70-76, 2012.

153. **Zhu X, Chu PB, Peyton M, and Birnbaumer L**. Molecular cloning of a widely expressed human homologue for the Drosophila trp gene. *FEBS letters* 373: 193-198, 1995.

154. **Zimmermann P, and David G**. The syndecans, tuners of transmembrane signaling. *FASEB journal : official publication of the Federation of American Societies for Experimental Biology* 13 Suppl: S91-S100, 1999.

Biography

Matthew Dragovich was born in Harrisburg Pennsylvania in October 1989. He attended Northampton Area Community College where he obtained his associate's degree in engineering in 2011. He then went on to Moravian College where he obtained a bachelor's degree in physics. Upon graduation with his bachelor's degree he attended Lehigh University in pursuit of his Ph.D.

While at Lehigh University Matthew began research on the endothelial surface glycocalyx. He has achieved several publications on this topic including, "Mechanotransduction of the endothelial glycocalyx mediates nitric oxide production through activation of TRP channels" which was published in the American Journal of Physiology in 2016. This project investigated the mechanism behind how endothelial cells produce nitric oxide due to mechanical perturbations. This entailed how proteins in the extra cellular matrix can distribute force across the cell such to active ion soluble channels. His work has been instrumental in clarifying the role of the ESG in nitric oxide production. This work will have potentially therapeutic implications for diseases such as hypertension and diabetes. In 2017 He has accepted a position as a post-doctoral researcher in the field of cancer immunotherapy at New York University.